FERROMAGNETIC AND FERRIMAGNETIC MATERIALS AS JOSEPHSON JUNCTION BARRIERS

By

Alexander Edward Madden

A DISSERTATION

Submitted to
Michigan State University
in partial fulfillment of the requirements
for the degree of

Physics—Doctor of Philosophy

2022

ABSTRACT

FERROMAGNETIC AND FERRIMAGNETIC MATERIALS AS JOSEPHSON JUNCTION BARRIERS

By

Alexander Edward Madden

In this dissertation we will show experimental results on different magnetic materials as Josephson junction barriers. Previous work by our group has shown that a Josephson junction with two magnetic layers can be engineered to allow controllable switching between a '0' state and a 'π' state, with applications in cryogenic computing. First, that work is expanded on to show that a different combination of Ni and NiFe thicknesses can also support that $0 - \pi$ switching, allowing a preliminary phase diagram of Ni and NiFe thicknesses to be outlined. Those measurements are done using a low-inductance symmetric SQUID to simplify the data analysis compared to previous experiments. We also explore other magnetic materials beyond Ni and NiFe. Fe is studied as a hard layer candidate and we show that while while it does have desirable magnetic properties, the critical current of the junction is greatly reduced compared to when using Ni.

We also study the rare-earth transition metal ferrimagnet CoGd. This alloy can be a compensated ferrimagnet with zero net magnetization while still supporting a spin-polarized transport current. We study the relationship between temperature, thickness, and concentration needed to grow compensated films of nanometer-scale thicknesses. We present transport data on Josephson junctions with a CoGd barrier showing the $0 - \pi$ transition characteristic of a ferromagnetic junction despite the near-zero magnetization.

ACKNOWLEDGMENTS

People will be thanked here

TABLE OF CONTENTS

LIST OF TABLES

LIST OF FIGURES

Chapter 1

Introduction

The past decade has seen a sharp and rapid increase in the energy use by computing and data centers in the US and worldwide. 2018 estimates of global energy use attributed 205 TW h to data centers, or approximately 1% of global electrical consumption [1]. While improvements in data center architecture and efficiency have blunted this increase, new and emerging technologies such as machine learning, the overall prevalence of IT devices, and increasing demands of high-performance computing all contribute to a continuing rise in overall global computing power.

1.1 Superconducting Computing

In a classical CMOS computer, a major source of energy consumption comes from passing current through conductors and semiconductors with finite conductance causing Joule heating. Superconductors, materials with zero resistance, therefore offer a natural platform to reduce the energy requirements of computing. Superconductors allow current to flow with zero passive energy use below the material's superconducting transition temperature T_c. For Niobium, one of the most popular materials for use in superconducting circuits, the critical temperature is above 9 K allowing the device to operate in the superconducting state in liquid helium at 4.2 K using commercially available refrigeration.

Attempts to use superconductors for digital logic date back to the 1950s with the development of the cryotron [2]. This device consisted of a superconducting wire about an inch

long with a control wire wound around it. Running a current through the winding created a magnetic field that suppressed superconductivity in the wire, allowing for switching between the superconducting and resistive state. While this allowed for a primitive form of binary logic, the slow switching time due to charging and discharging the inductive coil (then on the order of microseconds), large size of the device, and energy use in the resistive state, in competition with the rapid advancement of semiconductor technologies for computing, led to this approach to computing being largely abandoned by the end of the 1960s.

Another generation of superconducting electronics began after Brian Josephson's 1962 description [3] of the Josephson Junction, a device where supercurrent tunnels across a non-superconducting barrier. These junctions served as the foundation for several different families of superconducting logic. There was enormous effort on this approach under IBM's Josephson Technology Project in the 1970s [4,5], where logic was done by switching Josephson junctions between the zero and voltage states [6]. Although there was outstanding progress in fabrication, materials, and architecture under this effort the program was terminated in 1983 due to competition with rapidly advancing semiconductor technologies.

One category of superconducting electronics devices relies on storing information as quantized magnetic flux in inductive loops. This is broadly referred to as Single Flux Quantum computing. The earliest forms of SFQ computing were referred to as resistive single-flux-quantum logic due to the ohmic interconnects between the Josephson junction elements [7]. The Rapid Single-Flux-Quantum Logic/Memory family (RSFQ) [8] improved on this technology by using additional Josephson junctions as interconnects. The RSFQ family was able to reach picosecond-scale switching. Later SFQ variants improved performance and efficiency largely through improvements to delivery of bias currents such as energy efficient ERSFQ/eSFQ [9] (which replaced bias resistors with inductors), low-voltage LV-RSFQ which

fed bias currents through resistors at below 1 mV [10], and LR-RSFQ which added an inductor in series with a reduced bias resistor [11]. Another family of superconducting electronics systems is the Reciprocal Quantum Logic (RQL) architecture developed by Northrop Grumman [12]. This approach replaces the bias resistor with an AC transmission line, and encodes bits as pairs of opposite-polarity single flux quanta. The experiments in this thesis are largely motivated by a memory architecture using the RQL system.

While there has been enormous overall progress in superconducting computing, a scalable, efficient cryogenic memory has remained elusive. In its 2005 Superconducting Technology Assessment [13] the National Security Agency identified that "Cryogenic RAM has been the most neglected superconductor technology and therefore needs the most development." The lack of a scalable magnetic memory has continued to be a challenge in more recent years limiting the large-scale viability of superconducting computing [14]. Several approaches to cryogenic memory emerged in the following years. In addition to fully superconducting memories there are also systems to use energy-efficient non-superconducting or hybrid superconducting/normal electronics for memory at 4 K [15]. CMOS devices can run at lower power and higher speed at cryogenic temperatures due to increased carrier mobility [16], allowing for the high densities of existing semiconductor technologies such as charge-based dynamic RAM (DRAM) to be used for memory albeit at a higher power cost than a purely superconducting solution.

There has been enormous progress in purely superconducing memories from the late 1980s through the present day. Many of these memories have relied on SQUIDs containing SIS junctions to store SFQ pulses, starting with a 2x2 bit non-destructive readout (NDRO) cell demonstrated in 1989 [17] to more modern designs able to scale as high as 4 kbit [18]. SFQ-based memories are fast and efficient, but the memory density is intrinsically limited

by the geometric size of the superconducting storage loops for flux quanta.

Another approach to superconducting memory is the Josephson Magnetic Random Access Memory (JMRAM) architecture demonstrated [19] by Northrop Grumman. JMRAM stores information in the relative orientation of two magnetic layers within the barrier of a Josephson junction. With appropriately chosen magnetic material thicknesses, the two relative orientations of the magnetic layers change the ground-state phase difference of the Josephson junction between 0 and π. The magnetic Josephson junction itself serves only as passive phase shifter for a SQUID loop additionally containing two SIS Josephson junction. Because of the oscillation of SQUID critical current with phase, a small measurement current will trigger a voltage only in the π state. Much of the work in this thesis has involved study of different magnetic materials that can support a so-called π-junction for integration into this memory cell.

As both applied and basic research into Josephson junctions has progressed, several other types of controllable junctions have been proposed or demonstrated. The very first S/F/S π junctions using very weak ferromagnets were in some sense controllable because they underwent a $0 - \pi$ or $\pi - 0$ transition as a function of temperature [20, 21]. Long S/N/S junctions can be converted to π-junctions by injecting current into the normal part of the junction [22–27]. A Zeeman (magnetic) field applied to an S/N/S junction can produce a controllable π junction [28, 29], as can injection of a nonequilibrium spin population into an S/N/S junction [30]. Phase control has been demonstrated using electrostatic gating in carbon nanotube [31, 32] and quantum dot junctions [33, 34], or by magnetic control in spin-triplet Josephson junctions [35]. There are theoretical proposals to produce controllable π junctions using spin-triplet superconductors and ferromagnets [36], using a quantum-dot Josephson junction containing a molecular spin [37], by electrostatically gating MoS_2 mono-

layers [38], and with pinned Abrikosov vortices [39]. The recent intense interest in topological systems will undoubtedly turn up multiple ways to realize Josephson junctions with controllable phase states [40]. Phase control has immediate application in multiple areas of superconducting electronics [41]. π junctions have applications in both high-speed low-power classical computing [42–45] and in quantum computing [46–49]. A superconducting field-programmable gate array has recently been designed using magnetic Josephson junctions for using in single-flux-quantum (SFQ) computing [50]. The ability to control the phase state of a junction in-situ will surely lead to a wealth of new circuit designs.

1.2 Chapter Overview

Chapter 2 gives a discussion of the physics of superconductivity and magnetism. The proximity effect is discussed in the context of superconductor-normal (SN) interfaces and superconductor-ferromagnet (SF) interfaces. The theory of magnetic Josephson junctions and π junctions is covered, as well as a description of Superconducting Quantum Interference Devices (SQUIDs).

Chapter 3 discusses the sample fabrication techniques used in this work. This chapter is meant to present the techniques and recipes used both to document what was done here and to serve as a reference for future experiments. Microfabrication techniques including photolithography and electron-beam lithography are discussed, as well as material growth techniques such as the sputtering of magnetic materials.

Chapter 4 discusses measurement of ferromagnetic Josephson junctions in a spin-valve configuration with two ferromagnetic layers, one nickel and the other permalloy. Unambiguous switching between a '0' ground-state phase difference configuration and a 'π' state is

demonstrated and the application of this phase control for cryogenic memory is discussed. The current limitations of this approach and need for new materials for the magnetic layers is also addressed, motivating chapters 5 and 6.

Chapter 5 discusses the use of iron as a magnetic layer in a π Josephson junction. Magnetic data is presented showing the effect of a Cu seed layer on the ferromagnet. Transport data showing the critical current of junctions of different thicknesses is presented to identify the crossover between the 0 and π states and the critical current of Fe junctions is discussed in comparison with other materials.

Chapter 6 discusses the rare-earth transition-metal ferrimagnet CoGd as a Josephson junction. Magnetometry data is used to show that CoGd can be grown as a compensated ferrimagnet with vanishingly small magnetic moment at carefully chosen combinations of temperature, composition, and film thickness. Transport in compensated ferrimagnets is discussed, emphasizing the possibility of spin-polarized transport current even with zero net magnetization. Josephson junction data is used to show that the ferrimagnet CoGd undergoes a $0 - \pi$ transition similar to a ferromagnet.

Chapter 7 summarizes the results and discusses future outlooks and possible additional experiments.

Chapter 2

Theoretical Background

Superconductivity was first experimentally discovered in 1911 with Heike Kamerlingh Onnes's observation that at liquid helium temperature, the resistance of mercury suddenly dropped to 'almost zero' below 4.19 K. He subsequently also demonstrated that current circulating in a ring of such a superconducting material persisted for long times without any observable decrease, providing further evidence that superconductors have truly zero resistance. In 1932 Meissner and Ochsenfeld observed that superconductors were perfect diamagnets; not only do they exclude magnetic fields from entering them but when cooled below their transition temperature they expel any magnetic fields already present. This expulsion revealed that the underlying physics must be deeper than simple 'perfect conductivity,' which would trap any flux within a conductor.

2.1 The London Equations

A theory describing the mechanism of superconductivity remained elusive for many decades. One of the first major steps was a description of the electrodynamics of a superconductor by F. and H. London in 1935 [51]. The Londons proposed that in lieu of Ohm's Law $\boldsymbol{J} = \sigma \boldsymbol{E}$ electric currents should be described by an acceleration equation for the current density $\boldsymbol{J}$ simply expressing the Lorenz force acting on freely movable electrons. Starting with the familiar $\boldsymbol{F} = m\frac{d\boldsymbol{v}}{dt}$, with a force $e\boldsymbol{E}$ acting on a charge carrier and a current

density $\boldsymbol{J} = ne\boldsymbol{v}$ we can write

$$\frac{d}{dt}\Lambda\boldsymbol{J} = \boldsymbol{E} \tag{2.1}$$

where $\Lambda = \frac{m}{n_s e^2}$ is a phenomenological parameter depending on the number density of superconducting charge carriers n_s. This equation alone supports stationary currents (constant $\boldsymbol{J}$) in the case that $\boldsymbol{E} = 0$. Taking the curl of this relationship and following Maxwell's equations leads to

$$\frac{d}{dt}\left(\nabla \times \boldsymbol{J} + \frac{\boldsymbol{B}}{\Lambda}\right) = 0 \tag{2.2}$$

Requiring $\boldsymbol{B}$ and $\boldsymbol{J}$ to be zero inside the superconductor consistent with the observations of Meissner and Oschendfeld then leads to the London equation

$$\nabla \times \boldsymbol{J} + \frac{\boldsymbol{B}}{\Lambda} = 0 \tag{2.3}$$

Taking the curl of the Maxwell equation $\nabla \times \boldsymbol{B} = \mu_0 \boldsymbol{J}$ (assuming negligible displacement current) and substituting in the London equation leads to

$$\begin{aligned}
\nabla \times \boldsymbol{B} &= \mu_0 \boldsymbol{J} \\
\nabla \times (\nabla \times \boldsymbol{B}) &= \nabla \times \mu_0 \boldsymbol{J} \\
\nabla(\nabla \cdot \boldsymbol{B}) - \nabla^2 \boldsymbol{B} &= -\mu_0 \boldsymbol{B}/\Lambda \\
\nabla^2 \boldsymbol{B} &= \mu_0 \boldsymbol{B}/\Lambda
\end{aligned} \tag{2.4}$$

and a similar process for $\boldsymbol{J}$ giving the final results

$$\nabla^2 \boldsymbol{B} = \mu_0 \boldsymbol{B}/\Lambda \tag{2.5}$$

$$\nabla^2 \boldsymbol{J} = \mu_0 \boldsymbol{J}/\Lambda \tag{2.6}$$

These equations indicate that fields and currents decay exponentially into a superconductor over a length scale $\lambda_L = \sqrt{\Lambda/\mu_0} = \sqrt{m/\mu_0 e^2 n_s}$. The Londons' argument did not specify the actual value of the number density n_s, simply arguing that some number of electrons were superconducting. A natural upper limit at the time was $n_s = n$ being the density of conduction electrons at $T = 0$, which would then decrease as the temperature was raised towards the superconducting transition temperature. Experimental measurements of the London penetration depth in superconductors often showed values greater than the upper limit $\lambda_L(0) = \sqrt{\Lambda/\mu_0} = \sqrt{m/\mu_0 e^2 n}$. Addressing this issue requires a quantum mechanical treatment of superconductivity beyond what can be done with only electrodynamics. Furthermore, later developments with the emergence of BCS theory showed that pairs of electrons carry supercurrent rather than individual electrons, but the changes in mass charge and number density cancel such that the overall predictions of the London theory are unchanged.

2.2 Ginzburg-Landau Theory

One of the most exciting developments in the theory of superconductivity was the model developed by Vitaly Ginzburg and Lev Landau in 1950 [52]. The Ginzburg-Landau theory introduced a complex pseudowave-function ψ to quantum-mechanically describe the superconducting electrons directly (as compared to the description of excitations in the later BCS theory). The local density of superconducting electrons can then be written as $n_s = |\psi(x)|^2$.

Pragmatically, this approach allows many macroscopic superconducting phenomena to be calculated using familiar techniques from quantum mechanics and provides a common language of wavefunctions to describe the behavior of superconductors.

The Ginzbug-Landau theory was developed by observing that the transition between the resistive and superconducting states could be treated using Landau's general theory of second-order phase transitions [53]. In a second order phase transition, the free energy of a system is minimized as written in powers of some order parameter, which is zero above the transition and nonzero below, and its derivatives. Applying this approach to superconductivity has the wave function $\psi(x)$ play the role of this order parameter, as there are superconducting electrons below T_c but zero above. If ψ is small and varies slowly in space the free energy density f can be written in the series form [54]

$$f = f_{n0} + \alpha|\psi|^2 + \frac{\beta}{2}|\psi|^4 + \frac{1}{2m^*}|\frac{\hbar}{i}\nabla - \frac{e^*}{c}\boldsymbol{A})\psi|^2 + \frac{h^2}{8\pi} \tag{2.7}$$

Minimizing the free energy in this way with expansion coefficients α and β led them to the differential equation for ψ commonly known as the first Ginzbug-Landau equation

$$\frac{1}{2m^*}(\frac{\hbar}{i}\nabla + e^*\boldsymbol{A})^2\psi + \alpha\psi + \beta\psi|\psi|^2 = 0 \tag{2.8}$$

This equation is analogous to the Schrodinger equation for a free particle in a vector potential plus the addition of a nonlinear term. The corresponding equation for the supercurrent density $\boldsymbol{J_s}$ is

$$\boldsymbol{J_s} = \frac{e^*\hbar}{i2m^*}(\psi^*\nabla\psi - \psi\nabla\psi^*) - \frac{{e^*}^2}{m^*}|\psi|^2\boldsymbol{A} \tag{2.9}$$

In 1957, a full microscopic theory of superconductivity was developed by J. Bardeen, L.N.

Cooper, and J.R. Schrieffer [55,56]. While a full treatment of BCS theory is outside the scope of this dissertation, the most salient feature is that dissipationless current is carried by pairs of electrons known as Cooper pairs. At the superconducting transition temperature, electrons at the Fermi level condense into pairs with zero net spin and momentum, which behave as bosons. In 1959 Gor'kov proved that the Ginzburg-Landau equations could be derived from BCS theory [57] applied in the neighborhood of the superconducting transition temperature. The superconducting gap parameter Δ of BCS theory is in fact directly proportional to the GL order paramater ψ. For a physical intuition the order parameter can be interpreted as the wave function of the center-of-mass motion of the microscopic Cooper pairs [54]. As the GL theory provides an easier platform for describing spatial inhomogeneity than BCS as well as using a more familiar quantum-mechanical language of a wavefunction, this approach will be used as much as possible when discussing Josephson junctions.

2.3 Josephson Junctions

Brian Josephson predicted in 1962 [3] that when two superconductors are separated by a thin insulating barrier it would still be possible for supercurrent to flow between them. The supercurrent I_s through the junction is given by

$$I_s = I_c \sin \phi \tag{2.10}$$

where I_c is the *critical current*, the maximum supercurrent the junction can support, and ϕ is the difference in the phase of the superconducting order parameter from one side of the barrier to the other. This constant supercurrent over the junction is refered to as the DC Josephson effect.

If a fixed voltage is applied across a Josephson junction, the phase different ϕ develops a time dependence given by

$$\frac{d\phi}{dt} = \frac{2eV}{\hbar} = \frac{2\pi}{\Phi_0} \tag{2.11}$$

where the quantity $\Phi_0 = 2\pi\hbar/2e$ is referred to as the magnetic flux quantum (for reasons that will be discussed in Section 2.8). Under a constant voltage the supercurrent through a Josephson junction given by equation 2.11 will oscillate at a frequency $f_J = \frac{2e}{2\pi\hbar}V$. For an applied voltage of 10 µV this works out to a microwave frequency of close to 5 GHz. This oscillation under constant voltage is called the AC Josephson effect.

The energy of a Josephson junction [58] can be calculated directly from the Josephson equations by integrating the electrical work done by a current as the phase changes

$$\int I_s V dt = \frac{I_c\hbar}{2e}\int \sin\phi d\phi = const. - E_J\cos(\phi) \tag{2.12}$$

where the Josephson coupling energy has been defined as

$$E_J = \frac{\hbar I_c}{2e} \tag{2.13}$$

The Josephson energy is then conventionally written as

$$U = E_J\left(1 - \cos\phi\right) \tag{2.14}$$

Evidently, the energy is minimized when $\phi = 0$.

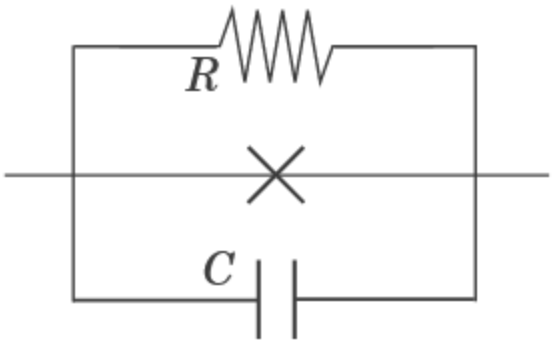

Figure 2.1: Equivalent circuit to a Josephson Junction as described the the resistively and capacitavely shunted junction model.

2.4 RCSJ Model

For a more practical description of the behavior of a Josephson junction the resistively and capacitively shunted junction (RCSJ) model is commonly used. In this model, illustrated in Figure 2.1, the physical junction is described as an ideal Josephson junction described by Equation 2.10 in parallel with a resistor R and capacitor C. The resistance accounts for dissipation in the voltage regime without having an effect in the lossless dc regime. The capacitance reflects the geometric capacitance between the two superconducting electrodes.

The total current across the circuit can the be written as

$$I = I_c \sin\phi + \frac{V}{R} + C\frac{dV}{dt} \tag{2.15}$$

Substituting in the voltage from the second Josephson relation (equation 2.11) this gives a second order differential equation for the phase

$$I = I_c \sin\phi + \frac{\Phi_0}{2\pi R}\frac{d\phi}{dt} + \frac{\Phi_0}{2\pi}C\frac{d^2\phi}{dt^2} \tag{2.16}$$

Dividing out the critical current to give a normalized current $I_n = I/I_c$ and using a

normalized time $\tau = \frac{2eI_cR}{\hbar}t$ this can be cleaned up to read as

$$i_n = sin(\phi) + \frac{d\phi}{d\tau} + \frac{2eI_cR^2C}{\hbar}\frac{d^2\phi}{d\phi^2} \tag{2.17}$$

The coefficient $\frac{2eI_cR^2C}{\hbar}$ is defined as the Stewart-McCumber parameter β_C leaving the differential equation

$$\beta_c\frac{d^2\phi}{d\tau^2} + \frac{d\phi}{d\tau} + \sin\phi - i_n = 0 \tag{2.18}$$

2.4.1 Mechanical Analogues

The dynamics of a Josephson junction described by Equation 2.18 warrant further exploration. Several mechanical systems behaving analogously are now well-known and help to develop an intuition for the behavior of the system. Returning to the equation of motion 2.16, we can slightly regroup terms to write

$$\left(\frac{h}{2e}\right)^2 C\frac{d\phi}{dt^2} + \left(\frac{h}{2e}\right)\frac{1}{R}\frac{d\phi}{dt} = E_J\left(\frac{I}{I_c} - \sin\phi\right) \tag{2.19}$$

Entertain the transformations $\left(\frac{h}{2e}\right)^2 C \mapsto m$, $\frac{h}{2e}\frac{1}{R} \mapsto b$, $\phi \mapsto x$ and we find the equation of motion

$$ma = -bv - \nabla E_J\left(-\frac{I}{I_c}x - \cos x\right) \tag{2.20}$$

Evidently, this equation of motion are the same as a particle with linear drag in a potential $E = -E_J\left(\cos x + \frac{I}{I_c}x\right)$. This situation is commonly described as a *tilted washboard potential*, as illustrated in Figure 2.2. The bias current plays the role of an overall tilt to the energy landscape. The capacitance provides mass and thefore inertia, allowing for the particle to continue to move even when a bound state is available. Similarly, the conductance

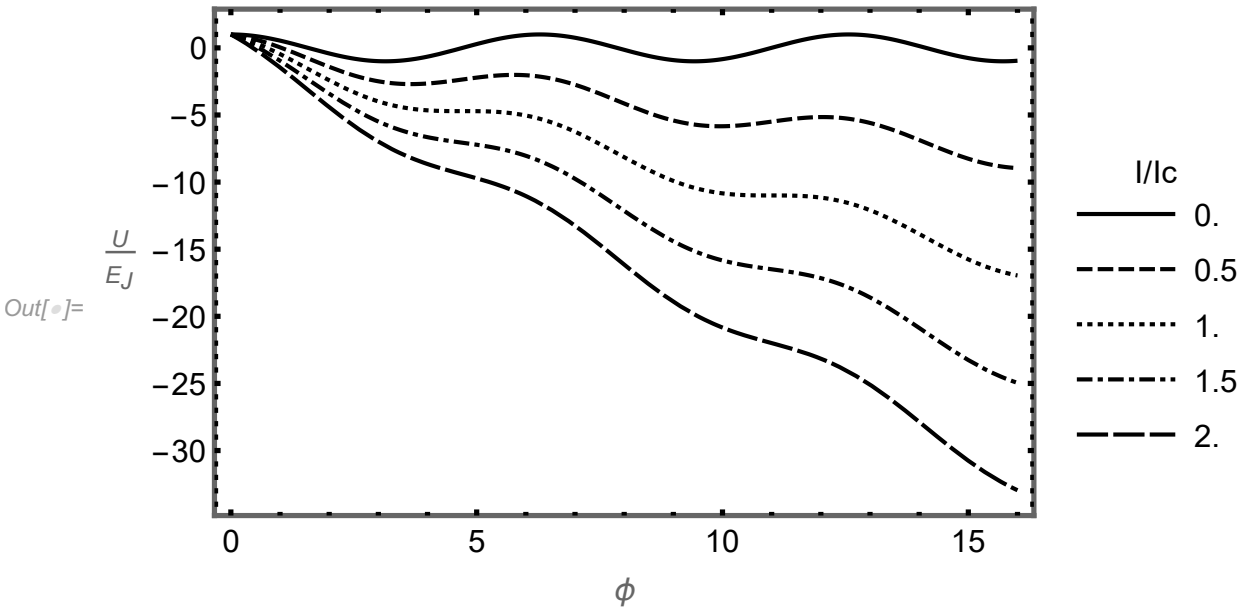

Figure 2.2: Tilted washboard potential of a Resistively and capacitively shunted Josephson junction. When the current through the junction is low relative to the critical current I_c, the tilt of the washboard is shallow. The junction remains trapped in one of the $2E_J$ depth wells, leading to a zero-voltage state. When the bias current exceeds I_c the tilt is steep enough to escape from one of the wells leading to a velocity (i.e. voltage) that is nonzero.

relates to the drag on the system, quickly trapping the particle in a well when available.

In the case when the bias current is small compared to the critical current of the junction, the potential is flat with sinusoidal wells of depth $2E_J$. The particle will remain trapped in one of these minima, only oscillating at the plasma frequency $\omega_J^2 = \frac{2e}{\hbar}\frac{I_c}{C}$. As the velocity of the particle maps back to the voltage via the second Josephson equation, the voltage in this bound state is zero after time-averaging. As the bias current increases the overall slope grows steeper and the wells shallower. At $I > I_c$ the minima of the cosine term are only inflection points overall and bound states no longer exist. At this point the particle escapes and moves down the washboard; equivalently the junction phase begins to monotonically increase and a voltage appears.

2.4.2 Overdamped Junctions

The junctions studied in this work were all of the form that the capacitance and resistance were small such that $\beta_c = \frac{2\pi}{\Phi_0} I_c R^2 C \ll 1$. These junctions are commonly referred to as overdamped, as damping effects dominate 'inertial' effects in this regime. In the language of the tilted-washboard potential described above this corresponds to a a particle with strong drag and low mass. If the current through the junction is decreased below the critical current (tilting the potential towards the horizontal), the particle will quickly get trapped in a local minimum. In this low-capacitance limit the RCSJ model is instead simply referred to as the RSJ model. Dropping the small term linear in β_c (and thus in C) from Equation 2.18 leaves

$$\frac{d\phi}{d\tau} + \sin\phi - i_n = 0 \tag{2.21}$$

Integrating this equation gives an explicit form [59] for the phase

$$\phi(\tau) = 2\arctan\left[\left(\frac{i_n^2 - 1}{i_n^2}\right)^{1/2} \tan\left(\frac{\pi\tau}{T}\right) - i_n\right] \tag{2.22}$$

with the period $T = \frac{2\pi\beta_J}{\left(i_n^2 - 1\right)^{1/2}}$. The voltage can then be calculated as proportional to the time average of $\frac{d\phi}{d\tau}$, giving the current-voltage relation

$$\frac{\langle V\rangle}{I_c R_n} = \sqrt{\left(\frac{I}{I_c}\right)^2 - 1} \tag{2.23}$$

This relationship shows that for currents below I_c the voltage remains zero, then increases following the square root in the voltage state. Equation 2.23 is used to fit the I-V curves measured in the experimental chapters of this work.

2.5 Josephson Junctions in a Magnetic Field

Real Josephson junctions are not zero-dimensional point contacts, and a full investigation must consider spatial variations and material properties within the barrier. The response of the I-V characteristics of the junction to an applied magnetic field is a valuable probe of both the superconducting nature of the junction and the magnetic properties of the barrier material.

The d.c. currents in a Josephson junction with maximum critical current density j_1 tend to be confined to the edges of the superconductor on the scale of the Josephson penetration length (given here in SI units) $\lambda_J = \frac{\hbar}{2e\mu_0 dj_1}$. Josephson junctions can therefore be roughly categorized as small junctions with dimensions much less than λ_J or large junctions exceeding λ_J. In small junctions the current density can be treated as approximately uniform absent any external fields.

Consider a circular Josephson junction of radius R in an in-plane magnetic field such that $H = (0, H_y, 0)$ using a coordinate system where the junction lies in the xy plane with current through the barrier flowing in the z direction as illustrated in Figure 2.3. Across the junction, the phase difference ϕ will develop a spatial variation

$$\nabla_{x,y}\phi = \left(\frac{2\pi}{\Phi_0}d\right)\boldsymbol{H} \times \boldsymbol{n} \tag{2.24}$$

where d is the thickness of the junction and $\boldsymbol{n}$ is the unit vector normal to the junction. As discussed in section 2.1 the magnetic field penetrates the superconductor on the scale of the London penetration depth $\lambda_L = \sqrt{\frac{m}{\mu_0 e^2 n}}$, meaning that to first order $d = \lambda_{L1} + \lambda_{L2} + t$ where t is the physical thickness of the barrier. Integrating this out then gives a linearly

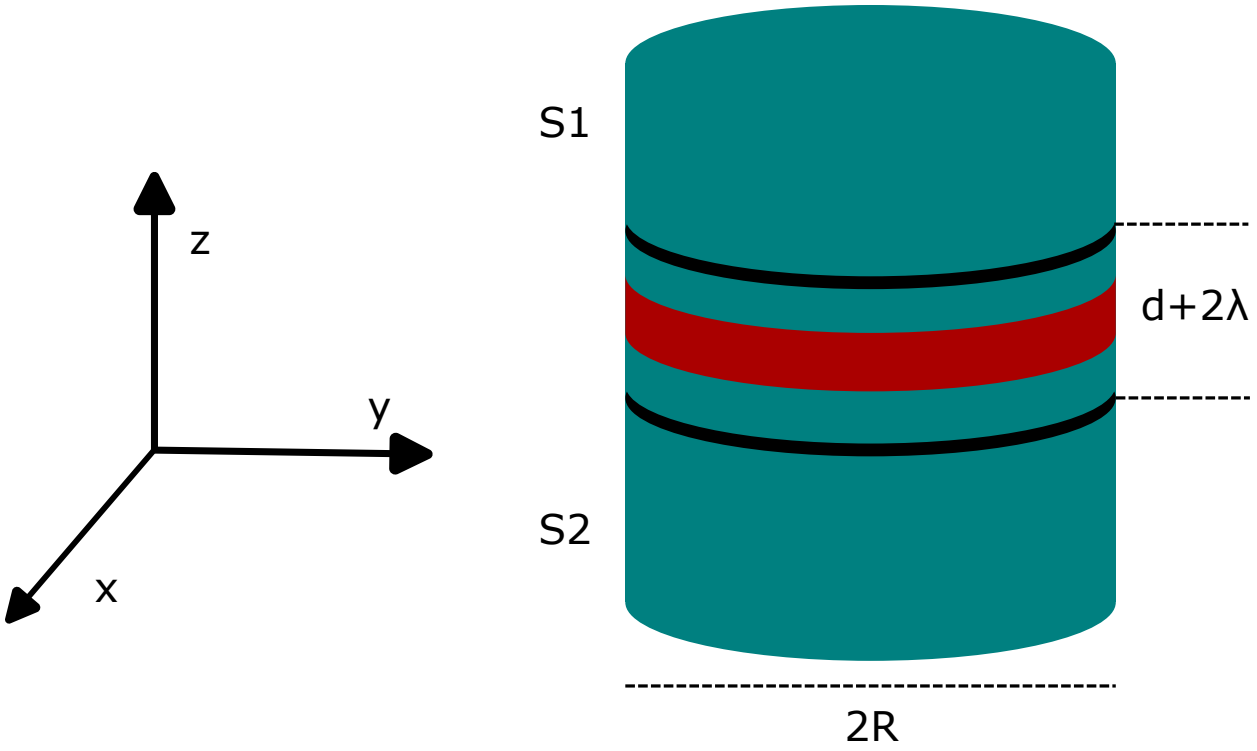

Figure 2.3: Orientation of small Josephson junction in a magnetic field

varying phase difference

$$\phi(z) = \frac{2\pi d}{\Phi_0} H_y x + \phi_0 \tag{2.25}$$

meaning that the current density shows periodic variation in the x direction across the area of the barrier. The current in the junction can then be written as

$$I = \iint dx dy j_1(x,y) \sin\left(\frac{2\pi d}{\Phi_0} H_y x + \phi_0\right) \tag{2.26}$$

In the case that the junction is small enough to treat $j_1(x,y)$ as uniform then calculating the maximum value of this integral [60] gives an Airy pattern

$$I_c = 2I_{c0} \left| \frac{J_1\left(\frac{\pi\Phi}{\Phi_0}\right)}{\frac{\pi\Phi}{\Phi_0}} \right| \tag{2.27}$$

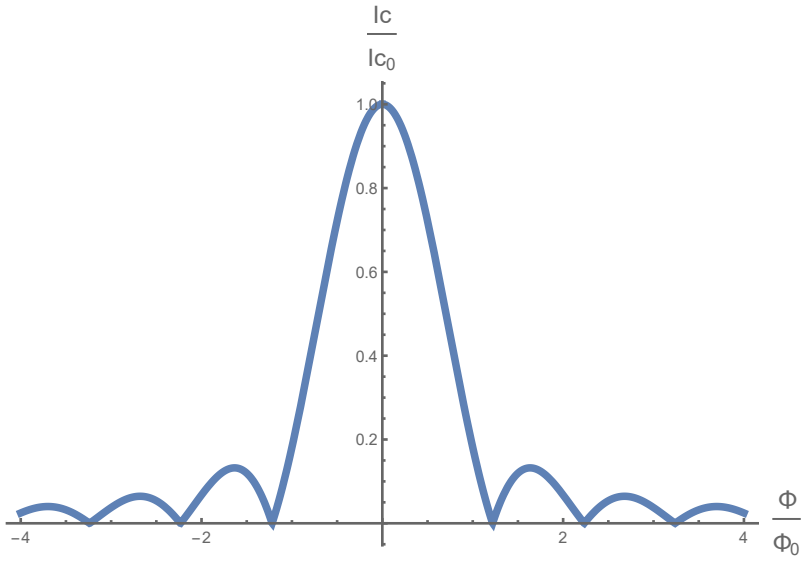

Figure 2.4: Modulation of a circular Josephson Junction's critical current by application of an in-plane magnetic field. This modulation is often referred to as a Fraunhofer pattern due to its similarity to optical diffraction. Knowing the applied field and the London penetration depth λ_L the width of the junction can be extracted from the period of the oscillation. Internal magnetization of the sample will result in a horizontal shift of the pattern with the central peak offset from zero due to the additonal flux.

where J_1 is a Bessel function of the first kind and order 1. Φ is the flux through the junction. In the case where the junction is much thicker than the London penetration depth and the same superconductor is used above and below the junction then $\Phi = B_y 2R(2\lambda_L + t)$. Performing a similar calculation for a rectangular junction gives a result with a sine function in the place of the Bessel function. This result is exactly analogous to Fraunhofer diffraction in optics, and the modulation of the critical current by magnetic field is often colloquially referred to as a Fraunhofer pattern.

The Fraunhofer pattern of a circular junction is shown in Figure 2.4. The same Airy pattern is also observed in elliptical junctions if the field is oriented along one of the principal axes. There are several ways the Fraunhofer pattern can be used to probe the structure of a Josephson. Because the critical current oscillates with the flux through the junction, if the applied field is well-characterized and λ_L is known then this can be used to extract the

junction diameter $2R$. The Fraunhofer pattern will show richer behavior if the barrier is itself ferromagnetic. Because an additional applied field is necessary to cancel the internal magnetic field of the junction, the plot will be translated along the applied field axis with the central peak offset from zero. This shift can itself change with field as the applied field may affect the magnetization of the barrier during the sweep. More complex magnetic structures will cause deviations from a simple Airy function. Relating the internal magnetic structure to the Fraunhofer pattern is generally non-trivial if the magnetization is not uniform [61] and often requires numerical integration in lieu of the maximization done of Equation 2.26.

2.6 S/N and S/F Proximity Effects

To fully understand the behavior of magnetic Josephson junctions, a more careful treatment of superconductor interfaces is necessary. Many of the devices studied here contain interfaces between superconducting Niobium and a normal metal such as Cu. Understanding transport across an S/N interface will provide the language necessary to also discuss S/F interfaces

The mechanism of charge transfer between a superconductor and normal metal is known as Andreev reflection. In a superconductor, electrons condense into Cooper pairs leaving an energy gap Δ at the Fermi energy. In a normal metal, electrons are delocalized and fill states up to the Fermi energy. This would seem to suggest that electrons would be unable to move from the normal metal to the superconductor as there are no single-particle states available in the superconductor at ϵ_F.

Transport across the interface can be understood by looking at the movement of pairs of electrons. There are no single-electron states available in the superconductor due to the

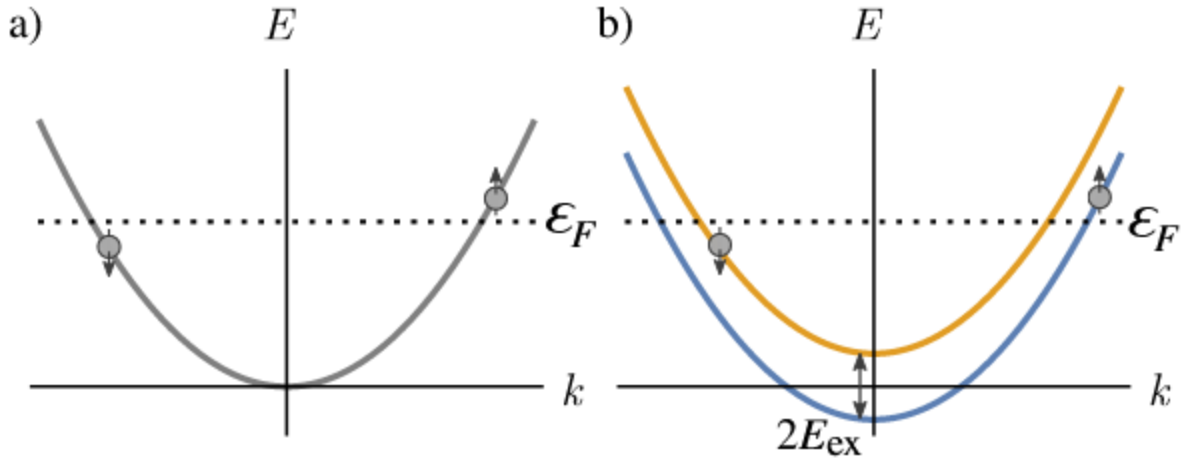

Figure 2.5: Toy model of a normal metal and ferromagnet band structures as seen by a Cooper pair. In the normal metal (a) the two electrons, one spin up and one spin down, both sit at the Fermi energy. In the ferromagnet (b) the bands for the two spins are separated by twice the exchange energy. The two electrons entering different bands will cause the pair to accumulate a net center-of-mass momentum.

presence of the superconducting gap. If an electron with spin up and momentum k crosses the boundary, it requires a second electron from below the Fermi level with spin down and momentum $-k$ in order to form a Cooper pair. Bringing this second electron then leaves a hole in the normal metal with spin down and momentum $-k$. In total then the net charge transfer across the interface is $2e$, with a Cooper pair created inside the superconductor and the incident electron reflected from the interface in the normal metal as a hole. The inverse of this process similarly allows for a Cooper pair in the superconductor to pass into electron states in the metal.

The picture is much richer when the barrier is between a superconductor and a ferromagnet. A qualitative discussion of these effects is given by Demler, Arnold, and Beasley [62]. In a conventional superconductor such as Niobium, and assuming that there is no spin-orbit interaction so that spin is a good quantum number, the Cooper pairs are in a singlet state which can be written as $\Psi = \frac{1}{\sqrt{2}}\left(|\uparrow\downarrow\rangle - |\downarrow\uparrow\rangle\right)$

In the magnetic region, a Cooper pair is no longer an eigenstate, and the pair correlation function decays quickly. For simplicity, consider the band structure of the ferromagnet to be the same as a normal metal with Zeeman splitting of twice the Exchange energy. The two opposite-spin electrons from the pair entering the ferromagnet must enter different spin bands, raising and their potential energies by $\pm E_{ex}$ respectively. This process is illustrated in 2.5. The kinetic energy of the electrons shifts accordingly to conserve total energy, shifting the position of the electrons along the bands. This leads to a nonzero center of mass momentum of the pair $\hbar Q = \hbar(k_F^{\uparrow} - k_F^{\downarrow})$. Treating the bands as parabolic, this shift is

$$\hbar Q = \frac{2E_{ex}}{v_F} \tag{2.28}$$

Combining this shift with that of an antisymmetric pair with the spins reversed to following the singlet state above gives the new wavefunction

$$\Psi = \frac{1}{\sqrt{2}} \left(|\uparrow\downarrow\rangle e^{iQX/\hbar} - |\downarrow\uparrow\rangle e^{-iQX/\hbar} \right) \tag{2.29}$$

where X is the center of mass coordinate of the pair. The inclusion of the center of mass momentum shift manifests as a spatial oscillation. A clearer view comes from rewriting the state in trigonometric terms

$$\Psi = \frac{1}{\sqrt{2}} \left(|\uparrow\downarrow\rangle - |\downarrow\uparrow\rangle \right) \cos QX + i \left(|\uparrow\downarrow\rangle + |\downarrow\uparrow\rangle \right) \sin QX \tag{2.30}$$

The first term is familiar, a singlet state as before with an overall spatial oscillation given by the cosine. The second term modulated by the sine function represents an $m = 0$ triplet state which is zero at the origin. Although the triplet contribution does not wind up

significant in transport through a simple S/F/S junction, triplet effects can play an important role in magnetic junctions with other magnetic structures or inhomogeneities [63].

The calculation above only considered electrons directly crossing the boundary as if in one dimension. For completeness it is important to account for the possibility that the incident electrons enter at an arbitrary angle θ. In this case, in the ballistic limit in a clean system the change in momentum is instead

$$\hbar Q \cos(\theta) = \frac{2E_{ex}}{v_F} \tag{2.31}$$

Integrating this over all all possible angles shows that the pair correlation function oscillates and decays in position on the length scale of the coherence length

$$\xi_F = \frac{\hbar v_f}{2E_e x} \tag{2.32}$$

proportional to

$$\int_0^1 d(cos\theta) \cos QX = \int_0^1 d(\cos\theta) \cos\left(\frac{2E_{ex}X}{\hbar v_f \cos\theta}\right) \approx \frac{\sin X/\xi_F}{X/\xi_F} \tag{2.33}$$

This approximate solution is only valid in the case that $X >> \xi_F$ A similar calculation can be performed for the purely diffusive case [64] giving instead an exponential decay

$$\Psi \propto \exp(-X/\xi_F)\sin(X/\xi_F) \tag{2.34}$$

where the coherence length now depends on the diffusion constant of the ferromagnet

D_F as

$$\xi_F = \sqrt{\frac{\hbar D_F}{E_{Ex}}} \tag{2.35}$$

2.7 Magnetic π Junctions

In a magnetic Josephson junction, the oscillation of correlation function in the magnetic layer can be taken advantage of to form a so-called π junction, as first predicted in 1977 by Bulaevksii et al. [65]

In a conventional Josephson junction, the energy is given by

$$E = \frac{\hbar I_c}{2e}\left(1 - \cos\phi\right) \tag{2.36}$$

This is clearly minimized when the phase difference across the junction is zero. In a magnetic junction, the pair correlation function oscillates with thickness. The thickness of the barrier can be carefully chosen such that the correlation function is negative at the point where the second superconductor is added. The energy is then given by

$$E = \frac{\hbar I_c}{2e}\left(1 - \cos\left(\phi - \pi\right)\right) \tag{2.37}$$

In this case the minimum energy instead lies at $\phi = \pi$. So-called 'π-junctions' using magnetic barriers were first experimentally observed in the early 2000s by Ryazanov et al. [20] and Kontos et al. [66]

2.8 SQUIDs

Perhaps the most famous application of Josephson junctions, as well as a necessity for making measurements informing us about the phase of a junction, is the Superconducting Quantum Interference Device (SQUID). In general, SQUIDs consist of one or more Josephson junctions embedded in a superconducting loop.

2.8.1 Fluxoid Quantization in a Superconducting Loop

Consider a superconductor forming a closed loop. As described previously, below the superconducting transition temperature the state can be characterized using a superconducting order parameter ψ which behaves analogously to a quantum-mechanical wavefunction. In order for this order parameter to be physically meaningful (as it gives the Cooper pair density as a function of spacial coordinate) it must be single valued. Around the loop the phase of the wavefunction can only change by an amount $2\pi n$, where n is some integer. Writing the wavefunction in the form $\psi(r) = \sqrt{\rho}e^{i\phi}$ the current density from the Ginzburg-Landau theory can be recast as

$$J_s = \rho\frac{e}{m}\left(\hbar\nabla\phi - \frac{2e}{c}\boldsymbol{A}\right) \tag{2.38}$$

The phase gradient can then be expressed as

$$\nabla\phi = \frac{2\pi}{\Phi_0}\left(\boldsymbol{A} + \frac{m}{2e^2\rho}\boldsymbol{J_s}\right) \tag{2.39}$$

Integrating around a closed loop and requiring the phase to be single-valued therefore

gives a net phase change of

$$2\pi n = \oint \nabla\phi \cdot dl = \frac{2\pi}{\Phi_0}\left(\oint A \cdot dl + \frac{m}{2e^2\rho}\oint J_s \cdot dl\right) \tag{2.40}$$

$$\iint B \cdot d\sigma + \frac{m}{2e^2\rho}\oint J_s \cdot dl = n\Phi_0 \tag{2.41}$$

The left hand term is often referred to is the "fluxoid" and is clearly quantized in integer multiples of the flux quantum Φ_0. In the case that the integration path can be chosen deep within the superconductor relative to its penetration depth such that the current density can be treated as zero this reduces to the more intuitive

$$\Phi = \iint B \cdot d\sigma = n\Phi_0 \tag{2.42}$$

showing that the magnetic flux through the loop is quantized.

2.8.2 DC SQUID with two junctions

The SQUID experiments done in this dissertation consist of a superconducting loop containing two Josephson junctions. A schematic of this geometry is shown in Figure 2.6. Integrating Equation 2.40 following the dashed path to calculate the phase difference in the case where the $\boldsymbol{J}$ term can be ignored we find

$$2\pi n = \phi_a - \phi_b + \frac{2\pi}{\Phi_0}\oint A \cdot dl \tag{2.43}$$

$$\phi_b - \phi_a = \frac{2\pi\Phi}{\Phi_0} - 2\pi n \tag{2.44}$$

If an external flux is applied to the loop the net flux is $\Phi = \Phi_{ext} + LJ$ where L is

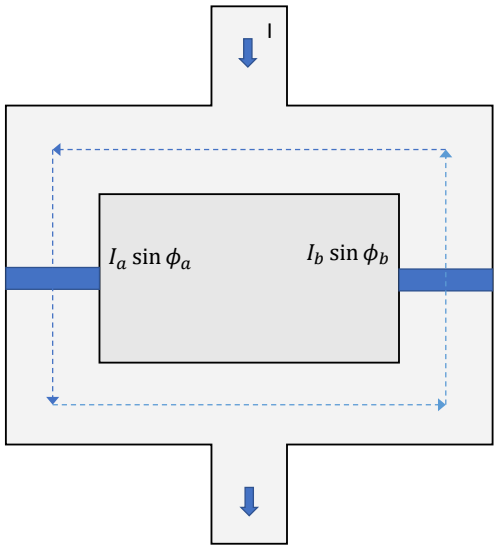

Figure 2.6: Schematic of a DC SQUID consisting of two Josephson junctions (blue rectangles) in a superconducting loop driven by an applied current I (thick arrows). An external bias current can be thought of as splitting along the two branches, passing through the junctions, and recombining (analogous to an interferometer). The loop also supports circulating currents. Dashed arrows indicate an integration path for calculating the phase change around the loop.

the self inductance of the SQUID loop and J is the screening current circulating the loop $2J = I_{c1}\sin\phi_1 - I_{c2}\sin\phi_2$. The total current across the loop is $I = I_{c1}\sin\phi_1 + I_{c2}\sin\phi_2$. If the self-inductance of the loop is small enough to assume $\Phi \approx \Phi_{ext}$ then the current can be written as

$$I(\Phi_{ext}, \phi_a) = I_{c1}\sin\phi_1 + I_{c2}\sin\left(\phi_1 - 2\pi\frac{\Phi_{ext}}{\Phi_0}\right) \tag{2.45}$$

The critical current can be calculated by maximizing this current with respect to ϕ_a. In the simplest case when the junctions are identical with critical current I_{ca} and the SQUID is symmetric this calculation yields [67]

$$I_c(\Phi_e) = 2I_{ca}\left|\cos\pi\frac{\Phi_e}{\Phi_0}\right| \tag{2.46}$$

Thus, the critical current of the whole SQUID oscillates periodically as a function of the flux threading the loop, with a critical current maximum at zero applied flux. This observation will be leveraged heavily in the analysis of Chapter 4.

Chapter 3

Sample Fabrication

Sample fabrication was an involved process that evolved from project to project. In this chapter I will detail the main processes and equipment used for Josephson junction and SQUID fabrication as well as the growth of magnetic films. This chapter is intended to be a fairly exhaustive description of the microfabrication process to serve as a reference for future students attempting to repeat these processes.

3.1 Josephson Junction Fabrication Process

Regardless of the exact materials used, the general process was the same for all of the Josephson junctions and SQUIDs fabricated for this work. Silicon chips used as substrates were coated in a protective layer of photoresist and cut from a wafer in advance. At the start of the fabrication process the photoresist was removed and the chips were cleaned in the cleanroom. After cleaning, the pattern for the bottom electrodes was patterned photolithographically. Both the superconducting niobium and the materials in the junction were then deposited by sputtering. After liftoff, e-beam lithography was used to define the micron-scale Josephson junctions with a negative resist. This left a protective cap over the area that will become the junction. An ion-milling process was then used to remove the barrier material everywhere except the junctions. In the same process, SiO was thermally evaporated to add an insulating layer over the bottom electrodes. After the removal of the negative e-beam resist, a second photolithography step was then used to define the top

superconducting electrodes over the junction. The top niobium and a protective gold layer were then deposited in a second sputtering run.

3.2 Substrate Preparation

A fresh fab run generally started with a wafer of silicon with native oxide covered in a protective layer of photoresist and diced so that the back of the wafer had score lines defining half inch chips. Gently pushing on the back of the wafer breaks off individual chips. Although a full sputtering run holds 16 chips most runs would start with 18 to allow two backups in case any chips break or are contaminated early in the process. The bulk of the photoresist was removed by spraying each chip with acetone over a waste beaker. The chip was then placed in a test tube and fully submerged in acetone. The full set of test tubes were then put into beakers of water and run through the sonicator for 10 minutes. The acetone was then poured out and replaced with isopropanol and given a second run in the sonicator. The IPA was then replaced with DI water and the samples sonicated a third time.

After chemical cleaning the substrates were further cleaned by an O2 plasma etch. Before plasma etching it is important to pump down the plasma etcher and run it empty to ensure the system is clean. After turning it on and selecting manual operation, press the vacuum button and let the chamber pump until the inital sound of pump has audibly quieted, typically about a minute. The pressure gauge can then be turned on; if the display is set to pressure it will start to flash when the base pressure of the chamber is reached. Check that only gas 1 (O2) is turned on and the pressure set point is at 300; although this is the normal configuration for silicon and photoresist processing the pressure is sometimes changed by other KMF users. For pre-cleaning or bulk photoresist removal, set the power setpoint to

300W. Turn on the gas and wait for the pressure to stabilize at the set point. If it does not equilibrate quickly adjust the gas flow rate, but adjustments larger than 1 SCCM are rarely needed. When the gas is stable, turn on the RF power and watch the power meter on top of the unit to make sure it is at the correct value. If the power is unstable or significantly lower than set it may be necessary to check the connection of the plate to the back of the unit. Etch for 300 s, briefly turning the RF power off and immediately back on at 150 s as the system has an alarm that will sometimes sound if run continuously for too long. When the etch is complete, turn off the RF power and then the gas. Wait for the chamber to return to its base pressure, then turn off the pressure gauge followed by the vacuum. To open the chamber, press the bleed button and unlatch the door of the chamber. The control software will automatically stop it from bleeding if it is not at a low enough pressure. The door will remain closed due to the low pressure, but if unlatched it will swing open on its own when the bleed has brought it to ambient pressure. The chips can then be loaded onto the center plate. Close the chamber and latch the door, then repeat the same process to plasma etch the bare silicon, with an RF power of 300 W and 300 units pressure. After removing the chips from the plasma etcher, close the door and turn the vacuum on to pump out the system. After the pump has quieted after a minute or two, use the large red off button to shut down the unit. At this point the chips should be clean enough for photolithography or as a substrate for high-quality magnetic films.

3.3 Photolithography

The superconducting electrodes for Josephson junctions were defined in a two step photolithography process. The bottom-lead photolithography is done on bare silicon and defines

the bottom superconducting electrodes as well as the area where the barrier material will be deposited. In SQUID experiments this step also defines most of the superconducting loops. After deposition and junction processing a top-lead photolithography step is performed to define top electrodes aligned with the micron-scale Josephson junctions.

3.3.1 Bottom-Lead Photolithography

Bottom-Lead Photolithography is performed on silicon chips cleaned as described in Section 3.2. While S1813 G2 photoresist can be used alone for defining junctions it is strongly preferable to use a bilayer of lift-off resist LOR5B and S1813 G2 for cleaner lithography and better edges, and this is strictly necessary for SQUIDs where small-area loops and corners must be defined. The bilayer process has the bottom layer of LOR5B develop faster than the top S1813, leaving an undercut in the resist profile. This prevents material from sticking to the edges of the channel in the resist after sputtering and gives cleaner liftoff when the resist is removed.

3.3.1.1 Spinning and Baking Resist

The spin coater in the cleanroom is used for applying resist to the clean chips. Before starting, cover the spin coater with a sheet of aluminium foil with a hole punched in the middle for the central spindle to catch any drips of resist that fly off while spinning. Select a chuck that is just smaller than the chip. Make sure the chuck is clean before starting, it may be necessary to clean off residual photoresist to get a good seal. Put the chuck on the coater, and cover the tip with a gloved finger. Use the pedal to start the spin coater and make sure it runs while covered, if it won't spin make sure everything is clean and the chuck is snugly connected. Put a chip on the chuck, and again make sure it spins and the vacuum

tightly holds the chip in place. After a quick test spin, the chip should hold firmly enough that it won't slip if gently pushed by the edge with a pair of tweezers.

Resist can be applied using either the pipetter with tips provided by KMF, or using disposable pipettes. Disposable pipettes are recommended to minimize risk of contamination with other users' photoresists. Only open the small jar of photoresist immediately before drawing resist. One disposable pipette should be enough to coat 16 chips. Blow the tip of the pipette off with dry air before drawing to make sure no dust contaminates the resist bottle. Draw from the lower-middle depth of the jar, keeping the tip deep below the surface but not touching the bottom to get the cleanest resist. Place the pippete on a holder angled downward so that any air migrates to the top of the bulb, and to ensure the tip is not touching anything while not in use.

Immediately before dropping resist onto the chip on the spinner, discard the first drop out of the pipette into the foil around the spinner. Then drop enough to cover most of the chip without spilling over the edges. When using S1813 G2 4-5 drops is usually enough, less LOR5B is needed because of its low viscosity. If doing a LOR/S1813 bilayer, spin the LOR for 45 s at 3000 RPM. After spinning, carefully remove the chip and visually inspect both the front and back. The front should be a uniform green (LOR) or red (S1813) color with only slight color variation near the edges and no bubbles or streaks. The back of the chip should be clean; if there is any resist residue it can be carefully removed using a cleanroom swab with a small amount of acetone on it, but avoid getting any solvent on the front of the chip and damaging the resist. It is important to have the back of the chip clean to have it flat and in good contact on the mask aligner, and to do any cleaning before baking to prevent any solvent from softening the resist leaving residue on the photomask. Check the "All Resist Info" document maintained on the Birge group OneDrive and on the cleanroom

microscope computer for the most up-to-date recipes for spinning and baking.

Resist	Description	Spin 1	Bake 1	Spin 2	Bake 2	Exposure	Developer	Remover
S1813-G2	Positive Photoresist	5000 rpm (50s)	95C 45mins			8s	Chlorobenzene (5min) 352 Developer (45s)	Acetone
LOR/S1813 Bilyaer	Positive Photoresist	3000rpm, 45s	180C 45mins	5000rpm 50s	95C 45mins	3.5s	MF 319 (45s)	Remover PG
ma-N 2401	Negative e-beam resist	3000 rpm, 40s	90C, 60s (hotplate)			e-beam	AZ-MIF 300 (10s)	Remover PG

Table 3.1: Common photoresist recipes used. The LOR/S1813 bilayer requires two spin and bake cycles. When baking the ma-N e-beam resist a hotplate can be used for the 60 s bake.

After spinning, put the chips in an oven-safe container such as a covered pyrex dish or aluminum foil boat and transfer to the oven in the class 100 section of the cleanroom. The samples in the Ni/NiFe SQUID project described in Chapter 4 were baked using the programmable hotplate as described by previous students [68, 69], but because of the dirty surface and uneven temperature profile of that plate the slower but more reliable oven bake is now preferred for all samples to prevent underbaking. LOR should be baked for 45 min at 180 °C while S1813G2 should be baked for 45 min at 95 °C. If both resist layers are being done consecutively it is important to turn off the oven and open the door after the LOR bake to cool the oven down to 95 °C while spinning the second layer of resist.

3.3.1.2 UV Exposure

The power supply for the mask aligner should be turned on at least an hour prior to use to ensure the bulb has warmed up. The chuck for the mask aligner is designed for chips larger than half-an-inch, so thin strips of dicing tape can be placed over the outermost row of holes to give the vacuum better adhesion to the back of the chip.

The bottom lead alignment can be performed mostly by eye. Set the height of the chip such that it is not in contact with the mask but the silicon is visible through the uncovered areas on the mask. The corners of the pattern on the mask have wide rectangles used for

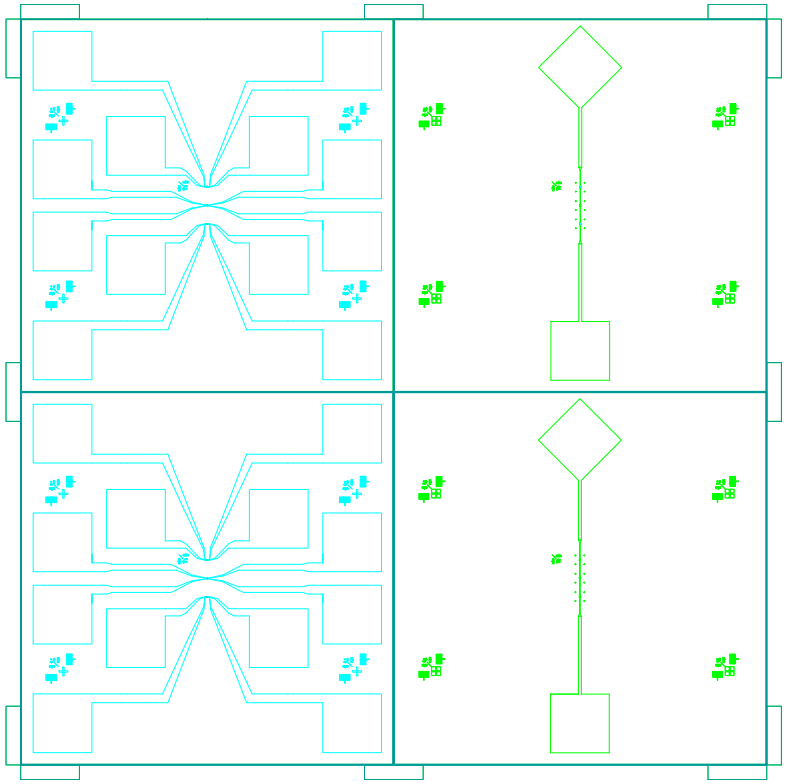

Figure 3.1: Photomask used for Josephson junction fabrication. The right hand patterns contain a long common bottom lead. The patterns on the left provide top leads that overlap the bottom at the points containing Josephson junctions running out electrodes for indium connections. The set of shapes and vernier marks in the corner are used for aligning the two lithography steps.

alignment; if the edges leading to the corner are visible at all four corners than the chip is roughly centered under the mask. Small variations in the position of the pattern can be compensated for during top-lead lithography.

Alignment must be much more precise when doing top-lead lithography, as the leads must pass over the existing junctions. As shown in Figure 3.1, the bottom-lead patterns include a set of alignment marks in all four corners of the pattern, and a smaller set in the central region near the junctions. Adjusting the position and angle of the chip while observing under

the microscope on a low magnification will get the rough alignment and angle correct. For making angle adjustments, it's easiest to use x and y axis corrections to align the markers on one corner of the chip, then make rotation changes to align the marks on the opposite corner.

With the position and angle of the chip roughly set, fine adjustments can be made in the x and y plane. To use the maximum magnification on the microscope the chip must be raised until it is almost in contact with the mask; the depth of focus is much shallower at high magnification. The rectangular alignment marks serve as a vernier scale, so even small differences in alignment will cause the outermost marks to be visibly out of place. X and y adjustments can be iteratively made first aligning the outermost set of marks on two corners of the chip then moving to the smaller marks. When the alignment marks all look set, move to the inner set of verniers close to the junctions. The y axis (horizontal alignment bars) is the most important part of the alignment, as even a small vertical shift will cause the electrodes to not lie over the junctions. Make any necessary final adjustments here, then do not make any further changes as adjusting the chip height or moving the microscope out of position and back in can be enough to shift the positioning slightly.

Before exposing, slowly raise the chip to come into full contact with the mask. If looking at the chip from a low angle, an interference pattern will appear on the chip when it is very close to the surface of the mask. These fringes will stop moving when the chip comes into contact with the mask. Do not raise the chip beyond this point, as additional pressure can move the mask or even cause it to come off the mask aligner.

When the chip is in position, place the UV shield over it and make sure the exposure mode is set to automatic and the desired exposure time is set. For a bilayer a 3.5 s exposure is used, if only using S1813G2 the exposure time is 8 s. Make sure any other chips are covered

so they aren't exposed to UV when the lamp is on.

3.3.1.3 Development

The LOR/S1813 bilayer is developed using MF 319 developer. For best timing start the timer and let it run for a couple seconds, then dip the chip into a beaker of MF 319 and swirl for 45 s. When the development time has elapsed move the chip into a beaker of DI water and swirl for a minute to ensure development has stopped. Dry the chip with nitrogen and photograph it under the optical microscope to verify the correct feature sizes. Be sure the yellow filter is in place on the microscope as the resist is still sensitive to UV.

If only S1813G2 is used, an optional artificial bilayer process can be used to develop a slight undercut for better liftoff. Before liftoff, soak the chip in a beaker of chlorobenzene for five minututes. This will cause the surface of the resist to harden slightly. Developing using 352 Developer for 45 s will then give a slight undercut as the deeper resist not exposed to chlorobenzene will dissolve faster than the surface.

After developing, chips should be de-scummed in the O2 plasma etcher to remove any resist residue. Having any resist residue on the silcon can cause for sputtered material to delaminate during the liftoff process. This plasma etch is done at 100 W for 120 s.

3.4 Sputtering

All of the samples in this work were grown by sputtering. The sputtering system had four 2.25-inch diameter triode guns that were used for deposition of all of the magnetic materials, as well as normal metals and superconductors. The chamber also included three DC magnetron guns used for normal metals. Two of those were reserved for Cu and Au respectively due to their presence in many different projects. The third magnetron gun at

the front could be used for other normal metals such as Ruthenium when needed, otherwise it was kept empty and covered with aluminum foil to keep it clean.

The DC triode guns consist of an assembly with a metal filament serving as a cathode on one end and an anode on the other. The third electode is the target consisting of the material to be sputtered. When high current is passed through the cathode, electrons are emitted which are accelerated to the anode. Two magnets are placed beside the path of this current, causing the emitted electrons to follow a helical path through the parallel electric and magnetic fields. These electrons passing over the target ionize the Ar gas in the chamber creating a plasma directly above the target. The target is held at an independently controlled negative voltage, causing it to be bombarded with Argon ions. These collisions knock metal atoms off the target. An aluminium chimney placed over the target constrains the emitted atoms to escape up towards the substrate 12 cm above the gun assembly.

The DC magnetron guns differ in that the target itself serves as the cathode. A set of magnets is placed directly below the target to create the magnetic field. The anode is placed above the target, in the direction of the substrate. The high voltage between the target and anode ionizes the Ar gas, creating a plasma confined above the target. This plasma then similarly bombards the target and emits metal atoms towards the substrate.

The sputtering system is able to hold 16 chips. In order to load the chamber and set up the guns, the chamber must be opened to the atmosphere. For high quality films the chamber must be pumped back to its base pressure before sputtering. A mechanical roughing pump is first used, and then a cryopump is used to pump down to a base pressure near 2×10^{-8} Torr. Once the cryopump is opened to the chamber, heat tape is used to bake the chamber overnight for 8 hours at 100 °C. This causes water adsorbed on the walls of the chamber to be captured by the cryopump, which has activated charcoal attached to the cold

head to further remove water. The chamber is then pumped down for an additional full day, leading to a typical pumping time of 48 hours. This cryopump must be regularly regenerated to keep the base pressure low, as it is regularly being used to pump the chamber out after exposure to atmosphere. During the summer when the humidity is high regeneration may be necessary after every 2nd or 3rd fab cycle.

At the time of the sputtering run a Meissner trap is used to cool the chamber and further reduce the pressure of any water or other contaminants remaining in the chamber.Liquid nitrogen flows into a cold trap until it reaches $-195\,^{\circ}\mathrm{C}$. Dry nitrogen gas is then flowed through a capillary tube cooling the sample stage to a temperature between $-20\,^{\circ}\mathrm{C}$ and $-30\,^{\circ}\mathrm{C}$. The sample stage temperature can be controlled by turning the nitrogen gas on and off. Due to the high impedance of the capillary the temperature change will lag behind toggling the gas; in a typical configuration where three 2.25 inch guns are running, switching the gas on or off after every chip will keep the temperature within the desired range.

3.4.1 Sputtering Setup

Prior to sputtering, the substrate holders and masks must be cleaned to avoid contaminating the chips. One plastic contained is filled with 3 parts nitric acid added to 1 part DI water and another with water. For samples where contamination is an especially high concern or if the sample holders are unusally dirty a drop of hydrofluoric acid (HF) can be added to the acid bath, but this is usually not necessary and is not recommended for most runs due to the safety concerns working with HF. *Do not use HF working alone and without explicit training and permission.* Carefully set the masks in the acid bath using tongs, and leave them there for at least 20 min. They can then be removed and set in water. The acid bath should remove most of the sputtered material from the masks.

Pre-rinse the sample holders with acetone to remove any sharpie labelling from previous runs, then use a wire brush and DI water to scrub any remaining material from the masks and sample holders. Pay special attention to the spots on the sample holder exposed by the opening on the mask as that region will have a full layer of sputtered material.

After scrubbing, give the sample holders and masks 5 minutes in the ultrasonic in acetone, alcohol, and then DI water. Lay them on a large Kimwipe and dry with a heat gun set to 950 °C until they are visibly dry and the wipe begins to show discoloration. Lay a second kimwipe over the parts and allow to cool.

To protect from cross-contamination between runs, the rotating SPAMA plate is covered with aluminum foil before being installed in the chamber. Lay a sheet of foil larger than the plate down on a smooth, clean surface and then set the plate on top of it. Cut in a circle around the plate with an approximately 1-inch margin, making sure to keep the foil as taught as possible. If the foil is loose it can sag when the target voltage is applied and short to one of the guns. Fold the edge of the foil over the plate, and cut out the four shutter holes. The chimney assemblies placed over the guns are also wrapped in foil, this is best done by cutting thin strips of foil twice the height of the chimney and then folding them over such that the inside surface of the chimney will have a smooth surface where gas is flowing and the ends are folded together on the outside. Lay a square of foil over the top of the chimney and cut a circular hole at the center to expose only the area of the sputtering target. Cut a length of aluminum foil and fold it three times on itself, then staple to form a skirt as tall as the chimney and approximately 1 cm wider in diameter.

3.4.2 Sputtering Technique

The sample plate and shutters are computer controlled, giving precise control of the time that each chip is exposed to a gun. However the gun and target electronics, temperature, and gas handling is done by hand. An hour before the run, the gas purifier connected to the nitrogen gas used for cooling is turned on and both the liquid nitrogen and nitrogen gas are connected to the chamber and turned on. When the cold trap reaches −190 °C throttle the valve on the liquid nitrogen so it is open only 30°; the cold trap should remain stable, adjust the liquid flow rate slightly if it starts to warm up. After an hour, the substrate temperature should reach −30 °C. From that point on the nitrogen gas can be turned on and off as needed to keep the substrates at the desired sputtering temperature.

Ensure that the cooling water supplies for both the large and small sputtering guns are turned on before starting the system. Turn on the argon gas flow controller and enable the gas for all four sputtering guns (even if not all are being used) to ensure there is adequate Ar in the system. Turn the main power on for the sputtering guns, but do not yet start them. To ignite the guns, close the main gate valve to throttle the cryopump until the Ar pressure reaches above 6 mTorr. Turn on the triode guns being used. If they don't stabilize quickly, increase the pressure. Once the plasma is ignited and all the gauges on the power supplies are stable, slowly close the gate valve until the sputtering pressure of 2.4 mTorr is reached.

When the plasma is stable at the sputtering pressure, turn on on the power switches for the sputtering targets. There are two controls for each target, one for the current through the filament and one for the voltage applied to the target. Wait five minutes after turning on the power, then begin to slowly ramp up the voltage. Keep the rate below increases of 50 V every 20 s. Because the CoGd targets are extremely brittle, when sputtering CoGd the

rate should instead be kept below 25 V every 2 min. The current should quickly ramp up to its set point when the voltage is applied, if necessary make fine adjustments to keep it at the desired value as the voltage is increased.

Allow 20 min to pass with the guns running before sputtering a real sample to unsure the chamber is clean and the sputtering guns are stable. Generally this time will elapse while setting up sequence files and measuring the sputtering rates. After setting the working directory with the sputtering sequence files in the software, the motor centering procedure can be run to allow last-minute adjustments to the shutter and SPAMA plate alignments. If the shutter is open to the position of the magnetron gun visible in the front window and the tape markers above the top of the chamber are aligned then the motor positions are correct. Only small adjustments are usually needed here as both of those alignments can be set by hand when installing the samples and SPAMA plate.

Before sputtering, measure the deposition rates of the sputtered material. If in automatic detection mode, the program will record the sputtering rate as long as one FTM is turned on and positioned over a gun. If the ion mill in the chamber is being used, ensure that the last material sputtered on the FTM was gold, then put it over the ion mill and manually enter the mill rate. The smaller magnetron guns are easier to start, so they are generally left off except when in use. Turn them on before measuring their sputter rate then back off again, and include a message in your sequence files to indicate when to do the same during the sputtering run.

The sputtering process is almost fully automated. At the start of the sequence, the shutter will close to the triode guns and the sample will be moved to the side of the chamber. A wobble stick is used to manually open the mask on the sample holder so the chip is exposed. If the mask is properly aligned, the pegs on the mask should be aligned with

the bridge screws. After sending the sample to the front window to visibly confirm the mask is open, the sputtering software will move the substrate from gun to gun and manage the shutters. Continue to toggle the nitrogen gas during the run to maintain the desired sputtering temperature.

3.5 E-Beam Lithography

After the bottom lead lithography and sputtering are complete, e-beam lithography is used to pattern the junctions. All e-beam was done using a Hitachi SU5000 Schottky field emission scanning electron microscope (SEM). Negative e-beam resist ma-N 2401 is spun for 40 s at 3000 rpm following the procedure outlined in Section 3.3.1.1. The negative resist is used to leave resist only in the area exposed to e-beam, leaving a protective cap defining the junction while the magnetic material is removed from the rest of the chip in the later ion milling process.

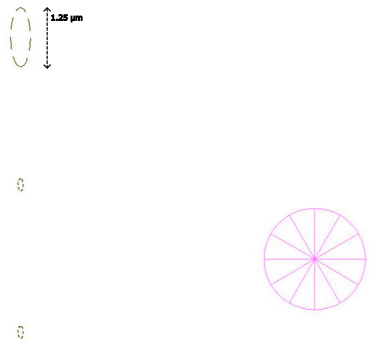

Figure 3.2: E-beam lithography pattern. The small ellipses define the 0.5 µm^2 Josephson junctions. The large ellipse is for visual inspection in an optical microscope before and after liftoff. The wagon-wheel shape should be uniform; variation in line thickness suggests a problem with alignment or stigmation.

Nanometer Pattern Generation System (NPGS) software is used to control the electron

beam while writing the pattern. The software includes control for a beam blanker so that the electron beam will not expose the area of interest except while writing.

The beam current of the SEM is kept at 68 pA using aperture 4 and a spot size of 1. The beam intensity is set to 30. A reference sample is kept in the cleanroom to adjust beam focus, alignment, and stigmation without unnecessarily exposing the e-beam resist to current. This sample has multiple angles, sub-micron features, and nanoparticles of different heights. A coarse focus is done at a low magnification such as 200X. The z-axis is then set such that the working distance as 15 mm; the exact z axis value will depend slightly on the focus. The magnification is then increased to a high enough value (up to 300kx) to clearly show one of the particles on the reference chip. The x and y alignment are adjusted until the particle is stable on the screen, if it oscillates back and forth the alignment is off in that direction. The stigmation control rapidly brings the particle in and out of focus. While defocusing, it should blur isotropically, if it distorts further along one axis adjust the stigmation until it's symmetric.

Whenever viewing a sample with undeveloped e-beam resist in the SEM the magnification must be kept as low as possible (200x or lower) or the field of view restricted to an unimportant region of the chip; the exposure from viewing at even 1000X is enough to start to harden the resist. Center the SEM such that the desired chip is in the field of view - large movements like this are easiest by navigating with the reference photograph of the sample holder taken when loading the chamber. While still at low magnification, set the cursor type to a line. Tracing a line along the edge of the bottom lead electrode will rotate the chip so that that line lies directly on the y axis. There are 'L' and 'Cross' shaped alignment marks from sputtering that indicate where each junction will go. Set the center of the field of view at the center of these alignment marks - turning on the central cross on the viewscreen

can help with this alignment. As the resist has poor conductivity, there is often very poor contrast making it difficult to see the alignment marks, lowering the scan speed, expanding the view display, and adjusting the contrast by hand may make them easier to find.

With the display roughly centered between the alignment marks, the final alignment is done using the NPGS software. Load the GDS file with the alignment patterns, and run the software in align mode. When prompted, set the magnification to 200x and continue to the next step. The program will use the blanker to scan over only the cross marks without exposing the central junction area. Move the cross marks in the program to line up with the image of the crosses on the chip —they can be moved together with the arrow keys or clicked and dragged to unlock and move separately. When the crosses are well-aligned, proceed to the next screen. At this point increase the magnification to 1000x when prompted. Repeat the alignment process with the L shaped marks. The marks sputtered on the chip should have sharp corners, but if there was poor contact during photolithography they may have rounded corners making alignment difficult.

When the alignment step is done, load the GDS file with the Josephson junction pattern. The standard pattern used includes two ellipses to define the $0.5\,\mu m^2$ junctions, a larger ellipse used to visually aid in liftoff, and a wagon-wheel shape to verify proper alignment and focus. The junctions are written with an area dose of $550\,\mu C\,cm^{-2}$ and the finer wagon wheels with a line dose $2.5\,nC\,cm^{-1}$.

3.6 Ion Milling

After e-beam development, the chips have bottom leads containing both the bottom niobium and the magnetic materials to be incorporated the junctions, and pillars of resist

defining the junctions. An argon ion milling process is used to remove the magnetic material everywhere except the area covered by the e-beam resist pillars, and then a SiOx layer is thermally evaporated to provide an insulating layer between the bottom and top electrodes.

3.6.1 Loading

The ion milling process is done in a separate vacuum chamber containing the ion mill, an Au sputtering gun, and a boat of SiOx for thermal evaporation. This chamber can hold up to five chips at a time, and has a load lock at the top allowing samples to be lowered into the system without breaking vaccuum.

Samples are prepared for ion milling in the cleanroom. The ion mill holders consist of a magnetic back plate to hold to the load lock, a copper or brass heat sink, and a mask covering the outer parts of the chip leaving only the center region exposed. Put a mask with a circular hole in the mask holder, with the clean side facing up to contact the chip, then lay a chip on top of it face down. Set a heat sink on the back of the chip. The heat sink should press against the chip, if necessary add a copper shunt behind the chip to make sure there's good thermal contact. Take out the heat sink and add a small amount of silver thermal paste to the back of the chip. A thin stripe scraped off the corner of a q-tip handle is more than enough, as excess paste risks contaminating the front of the chip.

Replace the heat sink and put the backing plate on top, aligning the screw holes with the heat sink and mask holder. Grabbing the whole assembly, flip it over so the chip is facing up. Screw two screws into the countersinks along the axis of the bottom electrode, keeping pressure uniform on both sides of the chip. Make sure the screws are deep enough to reach the threads on the backing plate and the surface is flat.

A similar process is used to prepare samples for the side-milling process. The side-mill

holders are tall enough for a chip to be inserted sideways. The slot for the chip is very slightly off from the vertical, so the sample will be milled from the side to break through the SiOx on the sides of the pillar before liftoff. The side of the slot that is facing down is marked so the chip can be inserted with its face angled down towards the mill.

With up to 5 chips loaded into appropriate ion-mill holders, bring the chips out of the cleanroom to the ion-milling chamber. Before loading, ensure that the black gate valve below the load lock is closed and turn off the ion gauge. Vent the load lock by turning the green nitrogen valve, just enough of a turn that you can hear it is adequate. When the pressure in the load lock reaches atmosphere it can be freely swung open, there is no need to use the front screw to latch or release it. Put the ion mill holder into the sample loading stick and then insert it into the load lock. Attach it to the magnet at the end of the load lock arm, lowering the arm if needed to make contact. Close the front door of the load lock without latching it and turn off the nitrogen. Make sure the roughing pump is on, then slowly open the valve to the roughing pump until it is unscrewed by about two fingers width. The pressure should drop slowly until it bottoms out between 1×10^{-3} and 1×10^{-2} Torr depending on the humidity. When it reaches its minimum value, close the valve to the roughing pump and slightly crack open the nitrogen valve for two seconds, again a quarter turn is enough. Open the valve to the roughing pump again and pump the load lock back down. Repeat this process of purging and pumping 3x.

When the load lock is at an appropriate base pressure (ideally below 1×10^{-2} Torr) close the valve to the roughing pump. It is extremely important that the roughing pump be closed before opening the gate valve while the turbopump is running or oil from the roughing pump will contaminate the chamber. The main valve between the load lock and the chamber can then be opened. Lower the sample arm to set the sample in one of the slots on the plate in

the chamber, then rotate the sample plate to pull the sample off the magnetic arm. Raise the arm back into the load lock and close the valve. Repeat this process until all samples are loaded into the chamber, then allow the chamber to pump down overnight.

3.6.2 Running the Ion Mill

Before milling, turn on the ion gauge and check the pressure, it must be below 1×10^{-7} Torr before beginning. Also turn on the power switch on the ion mill power supply at least 15 minutes before running for it to warm up.

Before ion milling, a DC magnetron gun is used to deposit a layer of gold onto a film thickness monitor (FTM). Rotate the sample plate so that the FTM is over the Au gun. If viewed from the front window, in this position the FTM will be directly behind the central post in the chamber. Open the valve under the chamber to flow argon into the system. Position the shutter plate so that the hole in the shutter is not in the Au position - either the SiOx or Ion Mill positions are safe. Slowly close the gate valve to the main turbopump on the chamber, the Ar pressure should rise, stop when it reaches 7×10^{-4} Torr for Au sputtering. Turn on the Au gun –if it doesn't ignite then slightly increase the pressure by further closing the gate valve then lower it again. Zero the FTM and set it to program 2 for measuring Au thickness. Open the shutter to the Au gun, and sputter at least 400 Å of gold per sample. This gold will be later milled off to measure the ion mill rate. Move the shutter back to the window position and turn off the Au gun when done.

Ion milling is performed at a pressure of 2.4×10^{-4} Torr, which is reached by adjusting the main gate valve to throttle the turbopump. After sputtering, the standard stack contains Cu(2)/FM(x)/Cu(2)/Nb(5)/Au(15) above the bottom superconductor (with all thickness in nanometers). To define the junction, this material is milled away into partially through the

Switch	Left Display	Right Display
None	Beam Current 9 9.0 mA	Accelerator Current 0mA
Discharge	-	Discharge Voltage 39V
Cathode	-	Cathode Current 3.6A-4.2A
Beam Voltage	Beam Voltage 300V	-
Accelerator	-	Accelerator voltage 30V
Neutralizer	-	Neutralizer current 9.0mA

Table 3.2: Ion mill parameters and switches used to adjust them

Material	K Value
Al	2.2
Co	3.5
Cu	1.9
Nb	6.7
Ni	3.9
NiFe	2.7
Ru	3.5
Pd	1.6
CoGd	3.8

Table 3.3: Ion Mill K Values

bottom copper to remove the magnetic material everywhere except the region protected by a resist cap. The target endpoint is halfway through the Cu; ion milling deeper into the bottom Nb can cause backsputtered superconductor to create shorts along the edge of the junction. The FTM is calibrated with the density of Au, so measuring the mill rate gives the rate that Au would sputter. Commonly measured materials in the lab have a 'k-value' coefficient calculated by ion milling films for a known time and comparing the milled depth to the measured Au mill rate. These values are shown in Table 3.3. The thickness measurements were done using both x-ray reflectivity and atomic force microscopy on the films before and after ion milling.

The time needed to ion mill is calculated by determining an effective gold thickness equivalent to the stack. For example, when making junctions with an Fe barrier the effective thickness of the capping layers, top copper, ferromagnet, and half the bottom copper would

be

$$t_{eff} = t_{Au} + k_{Nb} * t_{Nb} + k_{Fe} * t_{Fe} + k_{Cu} * t_{Cu} \tag{3.1}$$

$$= 541.9\,\text{Å} + k_{Fe} * t_{Fe} \tag{3.2}$$

with all calculations done in Angstrom to match the FTM output. The 541.9 Å effective thickness was common for all samples using the standard Cu(2)/FM(x)/Cu(2)/Nb(5)/Au(15) stack, meaning only the contribution from the ferromagnet needed to be changed sample to sample.

When the power supply has warmed up, turn the two source beam switches on one at a time to ignite it. The mill parameters are outlined in Table 3.2. The neutralizer value should be kept 0.5 mA above the beam current to fully neutralize the beam. The neutralizer current is very sensitive so only very fine adjustments to the front panel are needed. The cathode current can vary between 3.6 and 4.2 A, if it drops below this the cathode filament should be replaced. The cathode filament degrades over time due to the high current running through it. A new filament may show a current as high as 5.5 A but it will drop quickly after first use.

Position the FTM over the ion mill, then open the shutter to the IM position. Mill away 400 Å of Au until the mill rate is stable then close the shutter and record the rate. A typical mill rate for the mill parameters specified is 6.3 Å Au per second; if the value is significantly off adjust the beam and neutralizer currents. Move the sample over the ion mill, then open the shutter and start a timer. Ion mill into the bottom Cu, then close the shutter and measure the rate again. Repeat this process for all the samples in the batch. At the end of the run, put the FTM over the ion mill again and mill until the mill rate begins to drop

quickly. Removing any remaining Au this way will prolong the life of the FTM.

After ion milling is complete, turn off the source beam but leave the main power on for 15 min for the power supply to cool. Open the turbo pump all the way and turn off the Argon gas to return the chamber to its base pressure.

3.6.3 Silicon Oxide Evaporation

After Ion Milling, the metal bottom leads are exposed with the resist-covered pillars above them. A 50 nm layer of SiOx is thermally evaporated immediately after milling both to protect the leads and provide an insulating layer between the top and bottom electrodes. The FTM is switched to Program 5 which uses the density of SiOx. Position the FTM over the SiOx source, which lies directly below the sample loading arm, and make sure the shutter is closed to this position. For precise positioning, lower the sample arm until the magnet is just above the FTM. Turn on the power to the SiOx boat, and slowly turn up the voltage. The power should be increased by no more than 0.0020 kV per minute. Raise the voltage to 0.0260 kV to offgas the SiOx then lower to 0.0240 Open the shutter and measure the deposition rate. A typical value is between 6 and 7 Å per second. The SiOx voltage drifts significantly so it requires frequent adjustment to keep a stable rate. Close the shutter and record the rate.

To deposit a more uniform SiOx layer, the samples are rotated during deposition. Use the magnetic arm to raise the sample off of the sample plate, then rotate the sample plate until the hole passing through it is below the arm. Lower the sample until it is at the same height as the plate. Open the shutter, start the timer, and begin slowly turning the sample arm. When enough time has elapsed to deposit 500 Å (about 70 s, depending on the deposition rate). Close the shutter, and return the sample to its holder on the plate. Repeat measuring

the rate and depositing SiOx for the remaining samples. The SiOx should be turned off slowly by ramping down the power at the same 0.0020 kV/min rate.

The samples are removed using the same purging protocol as when loading them to keep the chamber clean and protect the pumps. If SiOx thickness is correct, the central region of the chips should be a brown-gold color such as seen in the background of Figure 3.3. If the SiOx is a blue or green, this indicates that too much material was deposited. Junctions with too thick an insulating layer are still viable, but the junction area may be incorrect and it will be more difficult to liftoff the pillars.

3.6.4 Side Mill

The thermally evaporated SiOx will completely cover the chip and the pillars. To assist with liftoff, a second ion milling process is performed milling from a steep angle instead of straight on. This breaks through the SiOx on the pillars and allows the remover to dissolve the resist. In the cleanroom, the chips are removed from the ion mill holders and the thermal paste is cleaned off with acetone and a q-tip, being careful not to get any paste on the front of the chip. The chips are then inserted into the side mill holders as described in Section 3.6.1. The central bottom electrode should be aligned vertically, with the chip angled to face slightly down. Side milling will be done twice to mill from both directions, so for consistency start with the top end of the chip up.

The side mill holders are loaded into the chamber for a second ion mill run. Only 800 Å of Au is deposited on the FTM as the rate is only measured at the beginning and halfway through the run. This process is less sensitive to the exact thickness milled, and generally a fixed mill time is used as long as the measured mill rate is close to the nominal value. Measure and record the mill rate, then side mill each sample for 2 minutes. After milling

the final sample, record the mill rate again and then mill each sample again for 2 minutes, giving a total 4 minute side mill time for each sample. The samples are then removed from the ion mill and flipped so the top of the chip is at the bottom of the side mill holder (with the face still angled down). This process can be done outside the cleanroom by removing a side mill holder, leaving the argon flowing in the load lock, quickly opening the holder and flipping the chip, and immediately replacing it. The process of two 2:00 side mills is then repeated from the other end of the chip.

3.7 Junction Liftoff

After side milling, a combined chemical and mechanical liftoff process is used to remove the e-beam resist and SiO from the top of the pillars. Before liftoff, photograph each set of junctions using the optical microscope at 50x. Use the manual exposure option, and record the power to the lamp and the exposure time used to get images that clearly show the color of the pillars with good contrast.

Each chip is placed face-up in a beaker of Remover PG. Set the beakers on a hot plate set to 80 °C and cap them with aluminum foil. They can first be checked after an hour, but leaving for at least three hours or even overnight (turning off the hot plate) can lead to easier liftoff. After enough time has elapsed, a cleanroom q-tip is used to gently rub along the bottom lead to break off any material still stuck to the pillar. Enough pressure is used to just begin to bend the q tip when holding it from the end. Swipe along the direction of the bottom electrode to avoid delaminating any of the sputtered metal. The plastic q-tips should be used, as the ones with wood handles can scratch the chip from pressure where the handle meets the tip.

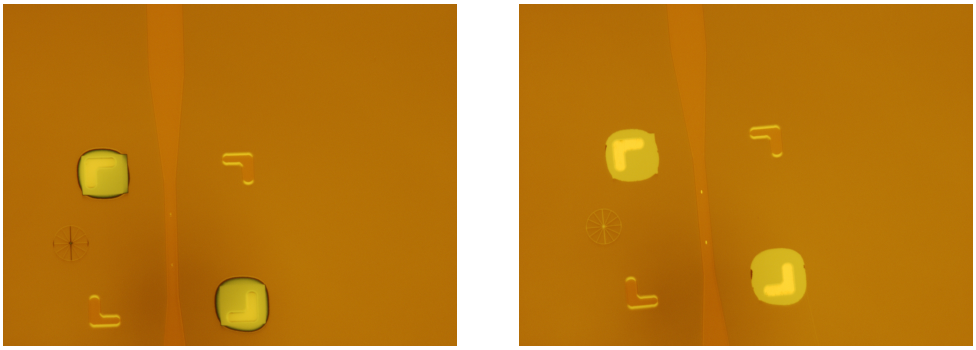

(a) (b)

Figure 3.3: Josephson junctions before (a) and after (b) liftoff. Junctions appear brighter with clearer edges after SiO and resist cap is removed.

Clean the chips in IPA and DI water, then return to the microscope to photograph again. If lifted off, the pillars should appear wider and brighter than before. The comparison of before and after liftoff is shown in Figure 3.3. If more than one pillar has failed to liftoff, return the chip to the remover and repeat the process.

After liftoff is complete, de-scum the chips using the O2 plasma etch. The top leads can then be defined by photolithography as described in Section 3.3.

Chapter 4

Controllable $0 - \pi$ Switching in Spin-Valve SQUIDs

One of the first projects undertaken for this dissertation was a study demonstrating controllable switching of a Josephson junction between the 0 and π state. The first experimental demonstration of such a phase-controllable junction was done by Bethany Niedsielski and Eric Gingrich [68]. The main idea of that work was to fabricate two of those controllable junctions and put them together in a SQUID loop. The SQUID could measure the relative phase of the two junctions, allowing observation of the switch between the 0 and π states. While that work unambiguously showed ground state phase switching, there were several points with room for clarification and expansion. $0 - \pi$ switching requires careful selection of material thicknesses in the junctions, by using different material thicknesses it was possible to expand the 'phase diagram' of viable combinations. The original SQUID data also required a fairly complicated analysis developed by Joseph Glick [69] to extract the phase difference. In this work we used a set of two different SQUID geometries that made the phase shift more apparent even in the raw data. Much of this chapter follows our published paper Alexander E Madden *et al.,* 2019 *Supercond. Sci. Technol.* **32** 015001 [70].

4.1 Junction Structure

The Josephson junctions studied had the structure $[\mathrm{Nb(25)Al(2.4)}]_3$/Nb(20)/Cu(2)/ NiFe(1.25)/ Cu(4)/Ni(2)/Cu(2)/Nb(5)/Au(15) sputtered, with a Nb(150)/Au(10) top electrode sputtered after junction fabrication. All thicknesses are indicated in nanometers with subscripts

indicating repeated layers. The 2 nm Cu layers were included to encourage cleaner switching of the magnetic layers, and the 4 nm Cu layer was to decouple the two ferromagnets.

4.2 SQUID Design

Two different SQUID device geometries were used in this work as shown in Figure 4.1. The first was a square-washer shape referred to as the pitchfork (PF) design due to the shape of its top electrode. In this design the flux current is injected through an independent flux line on the bottom lead metal layer, creating a field that threads the loop defined by the top lead. The sample current is injected through the bottom lead, splits between the two junctions in the SQUID, and returns via the top lead. Unlike in the earlier study, the two arms of the SQUID are symmetric to prevent shifts in the SQUID oscillations that complicate identifying the phase of the SQUID oscillations.

The second SQUID designed studied is the 'Ultra-low inductance' geometry. In this geometry the measurement and flux currents are injected via perpendicular leads on a common bottom electrode. To minimize cross talk the flux current is applied using a Yokogawa 7651 Programmable DC power source with a floating ground independent of the rest of the system. The top electrode is patterned directly above the bottom lead, so the loop of the SQUID contains only the thin insulating layer between the electrodes. The junctions are placed symmetrically with respect to the bottom lead so that the measurement current couples no additional flux into the loop in the case that the junction critical currents are equal. The characteristic 'ratchet' shape of the asymmetric SQUIDs in [71] is caused by a relative shift between I_c^+ and I_c^- that is reduced both by the symmetry of the design and the lower inductance.

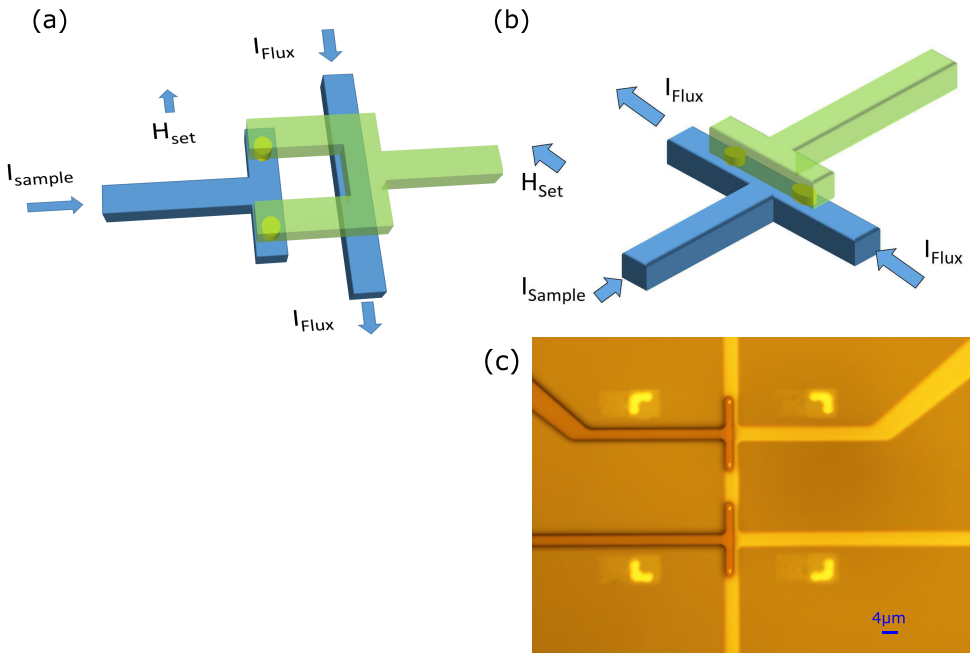

Figure 4.1: SQUID designs. (a) Pitchfork SQUID with loop defined by top lead area and independent line for flux current.(b) Ultra-low inductance (ULI) design with flux current and measurement current on a shared bottom lead directly below the loop.(c) Optical microscope image of ULI SQUID taken after top-lead photolithography. The common bottom electrode and alignment marks show as a light-metallic color. Dark 'T' shaped areas show where top lead will be deposited. Josephson junctions show as light points in overlap areas. In (a) and (b) the arrow label H_set indicates the direction of the in-plane magnetic field used to set and switch the magnetization directions of the magnetic layers in the junctions. Scale bar approximate.

4.3 Measurement Procedure

Before measurement, the samples were initialized by applying an in-plane magnetic field $H_set = -4000\,\mathrm{Oe}$ to ensure both magnetic layers of both junctions were magnetized in the negative direction and fully saturated (see Figure 4.1). The samples were then raised above the surface of the liquid helium in the dewar to release any flux trapped in the SQUIDs or in the measurement electrodes. The resistance of the flux line was monitored during this process to be sure the niobium was raised above its superconducting transition temperature. IV curves were measured using a fully automated SQUID-based potentiometer with a voltage gain of 2×10^{-7} and an RMS voltage noise of 6 pV. The flux current was applied with the programmable Yokogawa voltage source and a $1\,\mathrm{k}\Omega$ resistor. Before any field was applied, IV curves were measured as a function of applied flux current to observe the SQUID oscillations in the initial configuration, which was interpreted as having both junctions in the π state. The flux range was selected to observe multiple lobes of the critical current oscillation. For the pitchfork SQUIDs, a range from $-2.5\,\mathrm{mA}$ to $2.5\,\mathrm{mA}$ was used. In the ULI samples, the critical current began to show suppression at higher flux currents due to the proximity of the junctions to the flux line (the same suppression that causes the Fraunhofer pattern of a single junction) so the current range was restricted to $\pm 1\,\mathrm{mA}$. All transport measurements were taken in zero field to ensure there was no suppression of the critical current by the field used to set the magnets.

Before measuring the full set of SQUID oscillations vs set field, a preliminary measurement was performed to identify the approximate switching fields. An example of these data are shown in Figure 4.2. The flux current was fixed at a maximum of the SQUID oscillation to ensure the largest difference in critical current between the 0 and π states. The set field

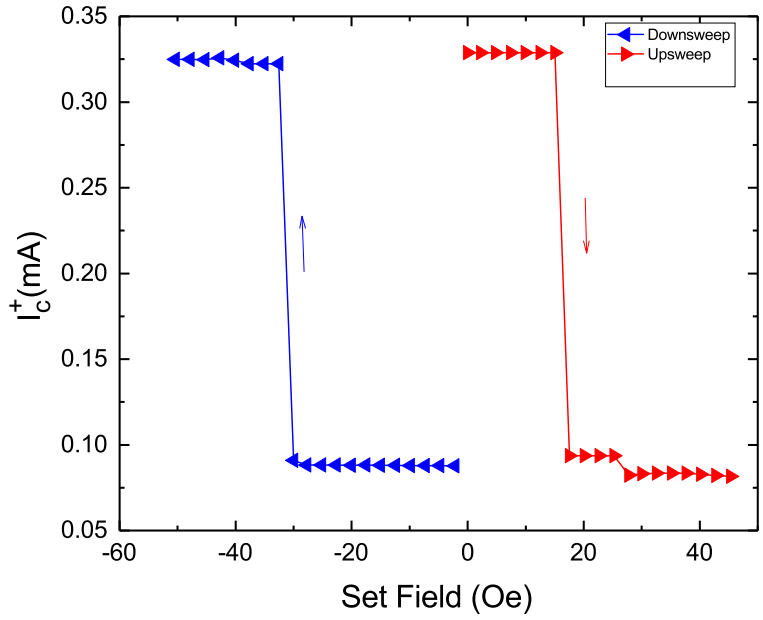

Figure 4.2: Preliminary sweep of set field on spin-valve SQUID. Starting in the parallel state magnetized in the negative direction, an in-plane magnetic field is applied and then the critical current of the SQUID measured at zero field. When the set field is increased (red arrows pointed right) to a high enough positive value to switch the free layer the critical current changes as the junction changes into the antiparallel state. The process is then repeated applying a set field in the negative direction (blue arrows pointed down) until the junction switches back into the original state.

was then incremented in small 2 Oe steps until a large change in critical current was observed. The set field was then incremented in the negative direction until the junction switched back to the original state. A 'training' effect was observed where the switching field varied from run to run at first but stabilized in subsequent measurements, so the set field was swept back and forth until the switching field was consistent run-to-run. This measurement gave a good estimate of when the free layer of the first junction switched, but does not provide any information about the relate phase of the junctions.

The phase-sensitive measurements followed a similar procedure, but full SQUID oscillations were measured instead of only the critical current at a single phase current. Starting

in the initialized $\pi - \pi$ state, IV curves were measured in zero field as a function of the flux current to observe the oscillation of the SQUID critical current. The set field was applied, with the typical increment being 5 Oe. The SQUID oscillation was then again measured in zero set field. When the set field applied is high enough to switch the free layer of the first junction, a half-period switch is observed in the subsequent SQUID oscillation. This shift in the raw data suggests that this switch is associated with a switch of that junction from the π to 0 state, although fitting the data is necessary to confirm this shift.

At point two different procedures can be followed to extract more information about the device. In a 'minor loop' measurement, the set field is then incremented in the negative direction. When the set field is enough to switch the junction back, another half-period shift is observed as the SQUID returns to its original state. In a 'major loop' measurement, the set field continues to be increased beyond the field necessary to switch the first junction. Because the two junctions have slightly different aspect ratios, the second junction has its free layer switch at a higher field than the first. When the set field exceeds the switching field of the second junction, another half-period shift is observed, returning the SQUID to its original phase state albeit with a different critical current. The set field was always kept below 100 Oe to avoid trapping flux in the samples. The set field was also brought only just high enough to observe the $0 - 0$ state as higher fields can begin to switch the Ni fixed layers in the junction. Applying an incremental set field in the other direction then allows the first junction to be switched back, giving access to the $\pi - 0$ state. Continuing to apply the negative set field then switches the second junction and returns the SQUID to its initial state.

These measurements were performed on SQUIDs on two chips. The first chip had three pitchfork samples, and the other had four ULI samples. The large loop inductance of the

pitchforks did give a relative shift between Ic+ and Ic- leading to a ratchet shape which obscured the phase difference between the states in the raw data. The raw data did still show a shift and change in critical current amplitude suggesting that there was some form of phase shift before the exact value was extracted during analysis.

4.4 Results

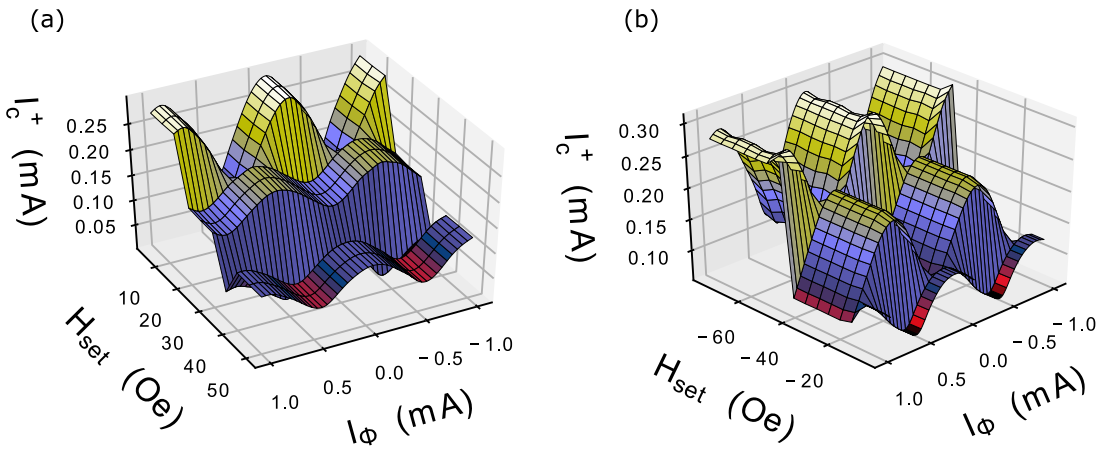

Figure 4.3: 3D Plot of critical current I_c^+ as a function of set field and flux current for ULI SQUID 4. (a) Major loop upsweep for ULI SQUID. Set field is incremented starting at zero until the free layers in the two junctions switch at 20 Oe and 40 Oe respectively. (b) ULI SQUID swept from 0 Oe to −70 Oe until both junctions both switch back to initialized state shown in (a).

Figure 4.3 shows a 3D plot of critical current as a function of flux current and set field for a major loop measurement on an ultra-low inductance sample. Sweeping along the flux current axis shows the standard SQUID oscillation as a function of the flux coupled into the loop. As the set field is swept through the switching fields of the two junctions, the SQUID oscillations show a phase shift and a change in amplitude. Figure 4.3a shows the upsweep data, with the set field being incremented in the positive direction from zero. When the set field reaches 20 Oe in the upsweep, the first junction switches. This is immediately evident

in the raw data as the critical current oscillations shift by half a period. There is also a decrease in the maximum critical current as the critical current of these junctions is less in the antiparallel state than parallel. At 40 Oe, the second junction switches. This is again evident by inspection as there is another decrease in critical current and half-period shift. The downsweep data in Figure 4.3b, taken immediately after the upsweep, show the reverse process. At -20 Oe, there is an increase in critical current and half-period shift as the first junction returns to the parallel state. This is repeated at -60 Oe as the second junction switches to the parallel state. The clear half-period shifts make the changes between 0 and π states evident even without further analysis.

Similar data is shown for a pitchfork SQUID in Figure 4.4. This measurement was a minor loop where the field was kept within a range that would only switch the first junction. The set field is incremented from zero in panel (a) until the first junction switches at 40 Oe. Again, a half-period shift is clearly observed. The set field is then incremented in the negative direction in panel (b) until the junction switches back at -40 Oe. Further changes in the critical current amplitude, but not phase, occur at -60 and -80 Oe, likely due to a domain wall being swept out of the NiFe free layer.

Figure 4.5 shows 2D plots of the critical current vs flux current for the two SQUID designs in the four possible magnetic states, as well as the fits to theory. Panel (a) shows I_c^+ and I_c^- for an ultra-low inductance SQUID. The flux current is restricted to a narrow range on the ULI SQUIDs so that the field due to the flux line doesn't significantly suppress the critical current by the Fraunhofer effect. Panel (b) shows similar data for a pitchfork SQUID. These data show that the I_c^+ and I_c^- maxima when the junctions are in the same state ($\pi - \pi$ and $0 - 0$) align with the minima when the junctions are in opposite states ($0 - \pi$ and $\pi - 0$). As the critical current oscillation is periodic in the flux through the

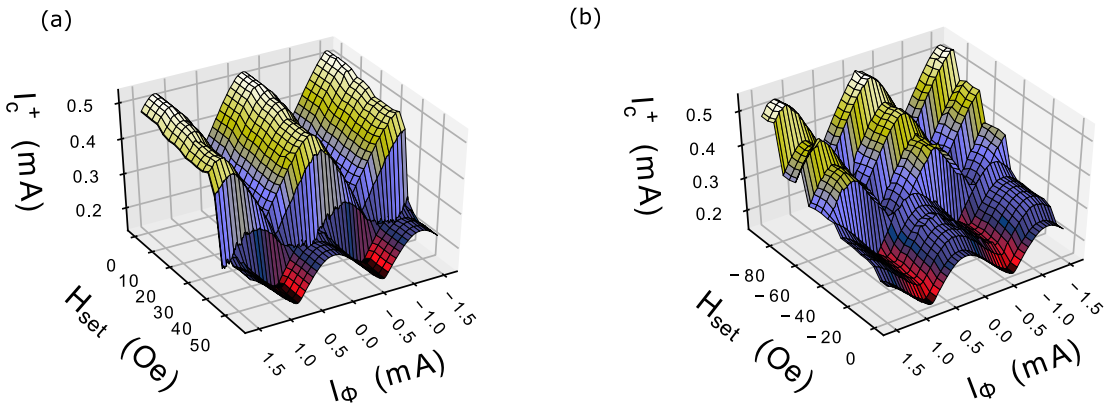

Figure 4.4: Minor loop measurement of critical current vs set field and flux current for pitchfork SQUID 1. (a) Minor loop upsweep for pitchfork sample. One junction switches at 40 Oe, showing a drop in critical current and a half-period phase shift. (b) Downsweep returning pitchfork to initialized state. Amplitude changes in several steps suggest that the free ferromagnetic layer is not switching as a single domain, but the phase shift occurs clearly at -40 Oe.

SQUID, a π phase shift corresponds to a flux shift of $\Phi_0/2$ in the oscillation. The theory fits the data very well and allows the extraction of the flux shift, inductances, and critical currents as described in section 4.5.

Controllable $0-\pi$ switching was observed in all four of the ULI SQUIDS measured in this study. The average phase change for the ULI samples between the $\pi-\pi$ and $0-\pi$ states was $\Delta\Phi_{\text{shift}}/\Phi_0 = 0.510 \pm 0.035$. For the pitchforks the average phase change was $\Delta\Phi_{\text{shift}}/\Phi_0 = 0.529 \pm 0.073$. We attribute the difference in the pitchfork results to a slight flux being coupled into the SQUID by the NiFe nanomagnets as they switch. This issue is avoided in the ULI design due to their high symmetry.

4.5 SQUID Analysis

The standard model of a DC SQUID [72] is characterized by four parameters: the inductances of the two arms L_1 and L_2 and the critical currents of the two junctions I_{c1} and

Sample	State	L_1 (pH)	L_2 (pH)	I_c^1 (mA)	I_c^2 (mA)	$\Delta\Phi_{\text{shift}}/\Phi_0$
1	$\pi-\pi$	2.11 ± 0.01	2.25 ± 0.01	0.204 ± 0.001	0.190 ± 0.001	0.511 ± 0.001
	$0-\pi$	2.17 ± 0.03	2.32 ± 0.03	0.204 ± 0.001	0.114 ± 0.001	
2	$\pi-\pi$	2.22 ± 0.04	2.26 ± 0.04	0.122 ± 0.002	0.173 ± 0.002	0.469 ± 0.003
	$0-\pi$	3.25 ± 0.13	3.05 ± 0.12	0.081 ± 0.002	0.163 ± 0.002	
3	$\pi-\pi$	1.93 ± 0.06	2.09 ± 0.06	0.174 ± 0.002	0.191 ± 0.002	0.507 ± 0.002
	$0-\pi$	1.95 ± 0.05	1.98 ± 0.05	0.173 ± 0.001	0.097 ± 0.001	
4	$\pi-\pi$	2.13 ± 0.08	2.08 ± 0.08	0.174 ± 0.002	0.114 ± 0.002	
	$0-\pi$	2.05 ± 0.52	1.15 ± 0.42	0.173 ± 0.001	0.029 ± 0.001	0.553 ± 0.005
	$0-0$	1.97 ± 0.52	1.30 ± 0.43	0.090 ± 0.001	0.029 ± 0.001	-0.508 ± 0.008
	$\pi-0$	1.97 ± 0.04	2.04 ± 0.04	0.096 ± 0.001	0.128 ± 0.001	0.454 ± 0.005

Table 4.1: Overview of best-fit parameters for ULI SQUIDs. Inductances L_1 and L_2 for the two arms of the SQUID are shown for four samples in the $\pi-\pi$ and $0-\pi$ states, as well as the critical currents through the two junctions. The SQUID oscillations are periodic in flux, so the shift of the oscillation pattern between states is shown as $\Delta\Phi_{\text{shift}}/\Phi_0$ such that a phase change of π would be represented by a $\Phi_0/2$ shift. The critical current of only one junction changes between successive states, consistent with one of the two junctions switching states. There were anomalous changes in the extracted inductances (which should be constant) between states in samples 2 and 4. Data from a major loop was fit for sample 4, showing that each switching event corresponds to a change in one of the two junctions.

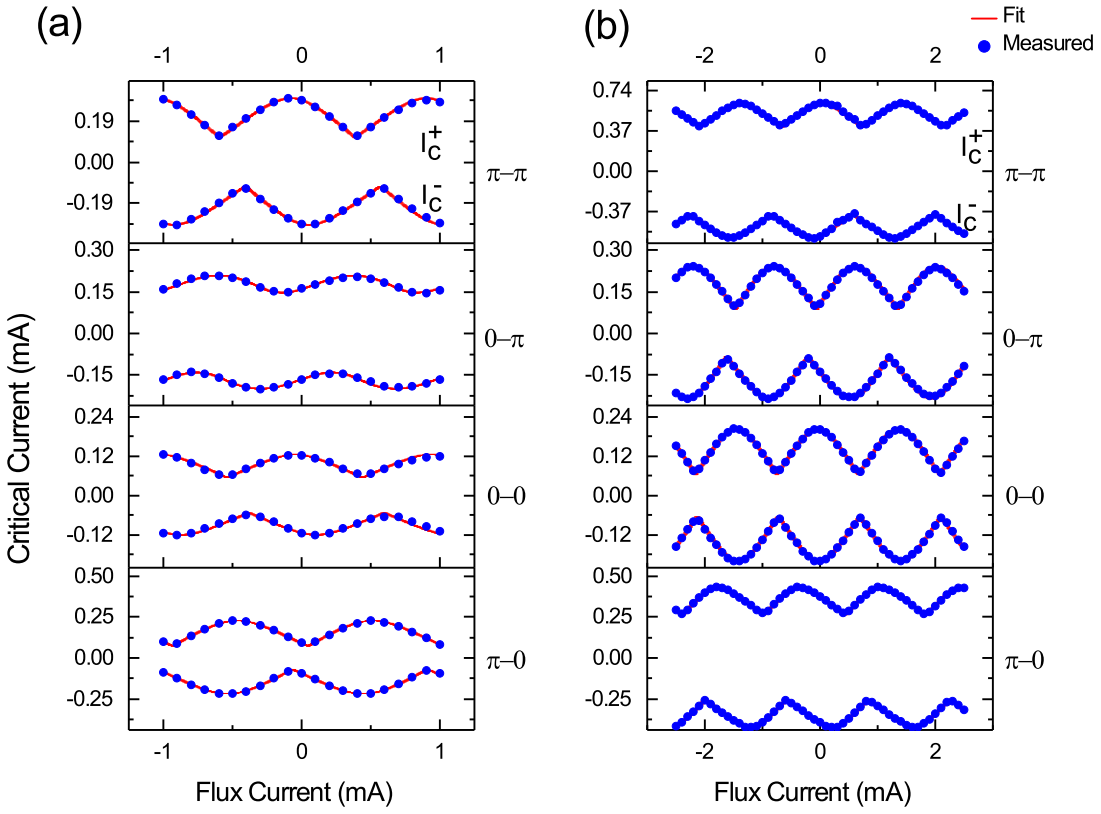

Figure 4.5: (a) Fits (lines) to measured I_c^+ and I_c^- data (symbols) in all four states for ULI SQUID 4. A half-period phase change is observed as each junction switches. The first three measurements are cross sections from a major loop in the increasing direction, and the final measurement is from the following downsweep after the first junction switches back to its initial state. The flux current was restricted to $\pm 1\,\mathrm{mA}$ to avoid suppression of the critical current by the Fraunhofer effect. (b) Data and fits to I_c^+ and I_c^- in all four states of pitchfork SQUID 2. Differences in critical currents of the two junctions manifest as slight relative shifts between I_c^+ and I_c^- in both samples.

Sample	State	L_1 (pH)	L_2 (pH)	I_c^1 (mA)	I_c^2 (mA)	$\Delta\Phi_{\text{shift}}/\Phi_0$
1	$\pi-\pi$	2.66 ± 0.03	2.78 ± 0.03	0.209 ± 0.002	0.302 ± 0.002	0.584 ± 0.001
	$0-\pi$	2.65 ± 0.03	2.61 ± 0.03	0.177 ± 0.001	0.093 ± 0.001	
2	$\pi-\pi$	2.57 ± 0.03	2.67 ± 0.03	0.293 ± 0.002	0.328 ± 0.002	
	$0-\pi$	2.51 ± 0.03	2.39 ± 0.03	0.102 ± 0.001	0.133 ± 0.001	0.439 ± 0.001
	$0-0$	2.47 ± 0.03	2.32 ± 0.03	0.102 ± 0.001	0.099 ± 0.001	-0.424 ± 0.001
	$\pi-0$	2.51 ± 0.03	2.66 ± 0.03	0.104 ± 0.001	0.324 ± 0.001	0.468 ± 0.001
3	$\pi-\pi$	2.91 ± 0.03	2.90 ± 0.03	0.248 ± 0.001	0.249 ± 0.001	0.564 ± 0.001
	$0-\pi$	2.79 ± 0.07	3.28 ± 0.07	0.182 ± 0.001	0.093 ± 0.001	

Table 4.2: Fit results for pitchfork SQUIDs. The deviation from the expected flux shift of $0.5\Phi_0$ is attributed to a change in the flux coupled into the SQUID by the NiFe nanomagnets when the free layers switch. Samples 1 and 3 both showed a significant change in critical current for only one junction. Fits are shown for sample 2 at field values along a major loop, where we expected one junction to switch at a time and then one to switch back when the set field was applied in the opposite direction. There is some anomalous behavior observed in the critical current changes for that sample where it appears both junctions are partially switching in the $0-\pi$ state, but flux shifts are still close to $\Phi_0/2$ between states.

I_{c2}. The inductance of the entire SQUID is characterized by the dimensionless parameter $\beta_L \equiv LI_c/\Phi_0$ where $L = L_1 + L_2$ is the loop inductance of the SQUID and $I_c = I_{c1} + I_{c2}$ is the sum of the critical currents of the two junctions. Fits to standard SQUID theory were performed using the critical current vs applied flux analysis described by Tsang and Van Duzer [73]. This analysis was implemented in a Mathematica script developed by Joseph Glick. The fits are described by the dimensionless parameters $\alpha_I \equiv (I_{c2} - I_{c1})/(I_{c2} + I_{c1})$ and $\alpha_L \equiv (L_2 - L_1)/(L_2 + L_1)$ which respectively characterize the asymmetries in the inductances and critical currents between arms. The fit also returns a value of Φ_{shift} for each SQUID oscillation. As the period of the oscillation corresponds to one flux quantum, a π phase shift in one Josephson junctions induces a horizontal shift in the SQUID oscillation

data by $\Phi_0/2$. The phase change was then calculated by taking the difference in Φ_{shift} between adjacent states. Because of the symmetric design, a preliminary fit was performed with the inductance asymmetry α_L fixed at zero. The results of this fit were then used as initial guesses for a fit where all four parameters were allowed to vary. For all of the SQUIDs analyzed, the best fit supported half flux quantum shifts between adjacent states, as expected. In the four ULI SQUIDs studied, the fitting program always converged to the expected value of Φ_{shift}. For the pitchfork SQUIDs, it was possible to force the fit to converge to a value of Φ_{shift} differing from the expected value by half a flux quantum by allowing large inductance asymmetries and carefully choosing the initial guess, but the fit consistent with $0 - \pi$ switching always had a lower χ^2. As noted in previous work [71], taking the wrong value for the phase shift also led to unphysical values for the inductances which changed from state to state. We are confident that the fits showing the $\Phi_0/2$ shift incorporate the correct set of parameters for the pitchfork samples, and this issue was not observed in the ultra-low inductance samples.

4.6 Inductance Extraction

The inductances calculated from the fits were compared with values found by performing a superconducting circuit simulation of the SQUID devices. The simulations were performed using the InductEx package developed by Sun-Magnetics. InductEx takes a GDSII file as input as well as a netlist listing all the couplings between elements to be calculated. The layout file can be easily prepared using LayoutEditor. A layer definition file is used to map layers in the GDS image onto 3D structures with materials, which the program then maps onto a circuit model defined by the SPICE netlist and outputs the self inductance of and

mutual inductances between the various segments of the circuit.

The initial results of the simulations dramatically underestimated both the self and mutual inductances of the ULI SQUIDs. When setting up the layer definition file, the conventional value of $\lambda_L = 0.085\,\mu m$ was used. The bottom electrodes in the SQUIDs were a Nb/Al trilayer rather than pure Niobium, so this was seen as a possible source of error in the simulation. The simulation was repeated varying the London penetration depth and the best agreement with the SQUID data was found using $\lambda_L = 0.185\,\mu m$ for the bottom lead. The average experimental inductance for the ULI SQUID was $L = 4.10\,pH$ and $M = 2.14\,pH$ while the simulations gave $L = 3.88\,pH$ and $M = 2.39\,pH$. For the pitchforks, the experimenal data gave $L = 5.33\,pH$ and $M = 1.48\,pH$ while the simulation gave $L = 5.00\,pH$ and $M = 1.69\,pH$.

As a consistency check on the new London penetration depth, an InductEx simulation was also done to compare with the asymmetric devices in the previous SQUID experiment from the group [71]. The geometry of the SQUIDs in that experiment differed in that the flux line was offset from the SQUID loop instead of running underneath it. Because there was less bottom-lead material close to the loop, varying λ_L had a negligible effect on the simulated inductances of those samples and the new value of $0.185\,\mu m$ was still compatible with those results.

After this work, Quarterman *et al.* performed Polarized Neutron Reflectivity (PNR) measurements on Nb/Al and Nb/Au superlattices [74] and measured penetration depths of $\lambda_L = 0.145\,\mu m$ and $\lambda_L = 0.190\,\mu m$ respectively, providing more support for the conclusion that these multilayers have much longer penetration depths than pure Nb.

4.7 $0 - \pi$ Phase Diagram

In choosing the Ni/NiFe thickness used for this study, the observations shown in Figure 3a of prior single-junction results by our group in [75] were used to identify thicknesses where the critical current would be the same in the P and AP states. Those data suggested that for Ni(2.0), a NiFe(1.25) free layer should produce a junction with nearly equal critical currents in the P and AP states. Our data show that we in fact had a decrease in critical current as each junction switched into an AP state, and that in our full stack the thicknesses chosen were not exactly at the crossing point shown in the single-junction data. This characteristic decrease in critical current from the P to AP state is observed for both switches in every sample measured. Given the findings of our single-junction study and the fact that the critical currents we observe are higher in the P state than AP we expect increasing the NiFe thickness slightly would bring the critical currents in the two states closer together.

Controllable $0 - \pi$ switching only works in the case where the phase difference across the junction is different in the parallel and antiparallel states. Exactly calculating the sets of thicknesses where this is possible remains a challenging problem. A single Ni barrier can be well described by a theory treating the transport as ballistic [76]. Similarly, a single NiFe barrier can be successfully described by a calculation in the diffusive limit [77]. In more complicated structures, the exact positions of the $0 - \pi$ transitions are less well understood. Adding a strongly spin-scattering layer to a Ni junction pushes the first transition to a higher thickness [76]. This shift may be interpreted as a change from mostly ballistic transport to diffusive. Normal and insulating layers can introduce additional phase shifts making it harder to predict the transition thicknesses [78, 79].

Some progress on predicting the transition thicknesses can be made following calculations

done by Crouzy, Tollis, and Ivanov [80]. That work calculated the critical currents in both the P and AP states of a magnetic junction with two ferromagnetic layers in the diffusive limit. The zeros of the formulas for critical current (where I_c crosses from positive to negative) then indicate the transitions between the 0 and π states. Those phase boundaries are shown in the left panel of Figure 4.6. The yellow lines with negative slope indicate the boundaries between phases in the P state, and the blue lines with positive slope indicate the phase boundaries in the AP state.

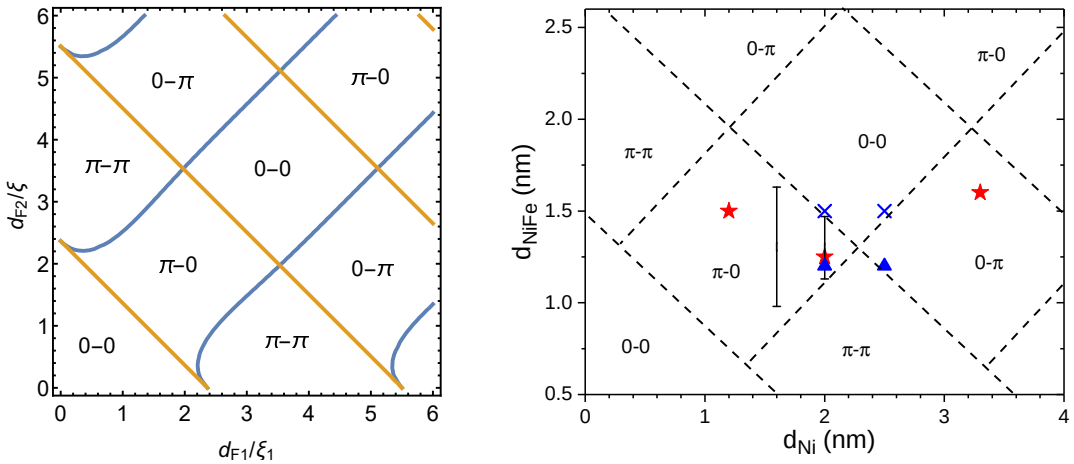

(a) (b)

Figure 4.6: Phase diagram of a Josephson Junction with a Ni fixed layer and a NiFe free layer. (a) Theoretical calculations based on Ref. [80]. Yellow lines indicate the boundaries between phase states in the parallel (P) state and blue lines indicate phase boundaries in the antiparallel (AP) state. In order for a junction to toggle between 0 and π, layer thicknesses must be selected such that the phase is different in the P and AP states, the regions labelled $0-\pi$ or $\pi-0$. In the other boxes ($0-\pi$ or $\pi-0$) toggling between P and AP would not change the phase state of the junction. (b) Experimental data on different combinations of Ni and NiFe thicknesses. Red stars indicate published points where $0-\pi$ switching has been successfully demonstrated. Blue triangles represent unpublished data from devices that showed switching, and crosses show thicknesses where phase switching did not work. Vertical bars show ranges that have been studied in single junctions but not confirmed with phase-sensitive measurements. The dashed lines indicate a preliminary attempt to map out the linear portions of the phase boundaries based on experimental data. In order to fit the boundaries to the experimental points it was necessary to start the NiFe thickness axis at 0.5 nm, this may indicate the presence of a magnetically dead layer that does not contribute to the phase accumulation. Figure reproduced from Ref. [81]

.

In the P state, the junction can be interpreted as behaving as if it had a single combined F layer with an effective thickness $\frac{d_{F1}}{\xi_{f1}} + \frac{d_{F2}}{\xi_{f2}}$. In the diffusive limit the first $0-\pi$ transition is expected to occur at $d_F/\xi_F = 3\pi/4$. The P state phase boundaries (yellow lines) as expected fall along the lines

$$\frac{d_{F1}}{\xi_{f1}} + \frac{d_{F2}}{\xi_{f2}} = (n + 3/4)\pi \tag{4.1}$$

In the AP state, the phase accumulation over the junction partially cancels leading to a reduced effective thickness. The $\pi/4$ phase shifts accumulated over each later also cancel, moving the first phase boundary to $\pi/2$ giving boundaries that can be approximate by the lines

$$\frac{d_{F1}}{\xi_{f1}} - \frac{d_{F2}}{\xi_{f2}} = (n + 1/2)\pi \tag{4.2}$$

. These lines match the blue boundaries in Figure 4.6 well except in the limit where one layer is thin, where they approach matching the single-layer boundaries.

The right hand panel of Figure 4.6 attempts to reconcile existing data on $0-\pi$ switching with the boundaries suggested by theory. The red stars indicate published points where $0-\pi$ switching has been demonstrated by phase-sensitve measurements [19, 70, 71]. These points must lie in a $0-\pi$ or $\pi-0$ region for switching to be possible. The vertical lines indicate regions that were shown to lie between critical current amplitude minima suggesting a phase boundary in single junctions [75] without phase-sensitive confirmation. The blue triangles and crosses indicate thicknesses where NGC succeeded or failed to observe phase switching respectively in unpublished data.

Using the known successful and unsuccessful thickness combinations, the dashed lines were drawn in as tentative phase boundaries. It was possible to place the lines such that the

known working thicknesses were in regions where the P and AP states had opposite phases and the non-viable thicknesses were not. The lines drawn do not reduce to the single-layer phase boundaries at the axis, but the curvature of the boundaries cannot be inferred from such sparse data. In order to match the experimental data it was necessary to begin the NiFe axis at 0.5 nm. We do not fully understand this but a possible explanation may be a magnetically dead layer at the interface that does not contribute to the phase accumulation.

4.8 Future Outlook

While this work showed that the Ni(2)/NiFe(1.25) system shows controllable $0-\pi$ switching, the broader effort to develop a scalable fully superconducting memory is still in its early stages. There is still a strong need for optimization and innovation in the choice of magnetic materials used to develop a viable memory device. The prototype memory cell demonstrated [19] by our collaborators at Northrop Grumman Corporation several intermediate states when switching between the parallel and antiparallel alignments, similarly to the partial switching seen in the pitchfork data in Figure 4.4. In order to repeatably and controllably write the bit, it will be important to find a magnetic structure that can cleanly and reproducibly switch without sacrificing the superconducting properties of the junction.

There has been a steadily increasing number of materials studied as a barrier for magnetic Josephson junctions in recent years [81]. There are several considerations when selecting the materials to go into a spin-valve structure. The fixed layer must have a high enough switching field to remain stable when the set field is applied. Ideally this layer should also be single-domain on the scale of the junction; stray fields from domain wall boundaries can interfere with the clean switching of the free layer. The free layer should similarly be single-domain

but with a low enough coercive field to switch easily without effecting the fixed layer. On top of the magnetic demands, the entire structure must also maintain a high critical current. In order for the magnetic Josephson junction to remain passive in the JMRAM architecture, its critical current must be above the approximately 100 µA I_c of the SIS junctions in the SQUID.

There remains room for improvement in every element of this system. Ni has become popular as a fixed layer due to its very high critical current [76]. In the π state a Ni junction can have an I_cR_n product as high as 100 µV, a factor of 10 higher than that seen in permalloy. Unfortunately, Ni is not single domain at the size scale of the junction and has significant stray fields, hence the broad switching field range. The work on Fe and CoGd in later chapters is directly motivated by the search for other viable fixed layer materials.

Another avenue for increasing the critical current density of the junctions comes from engineering not the barrier materials themselves but the interfaces between them. Recent work by Swapna Sindhu Mishra has shown that inserting a thin Ni spacer between the NiFe/Cu can increase the supercurrent transmission by almost a factor of 4 by decreasing the boundary resistance and spin-scattering asymmetry [82]. Similar interface-engineering efforts may unlock new ways to maintain viable superconducting properties of junctions with other materials in the future.

Improvements may also be found by optimizing the structure of the superconductor itself. Niobium is overwhelmingly the most popular material for superconducting electronics due to its critical temperature of 9.1 K (high enough to operate in liquid helium without additional cooling), the maturity of Nb-Al-Al_2O_3-Nb SIS junction fabrication, and robustness under thermal cycling. Unfortunately, Nb films develop a characteristic "rice-grain" texture giving high surface roughness. The Nb/Al multilayer used in this work was intended to help mitigate

this issue and give a smoother Nb surface. Research on new smoothing recipes such as inserting an Al/Cu seed [83] below the ferromagnets or oxidizing and then ion milling the Nb [84] can give a smoother interface and better magnetic switching.

Chapter 5

Iron Ferromagnetic Josephson Junctions

Despite the allure of Ni as a hard layer for magnetic spin-valve Josephson junctions due to the large supercurrents it can support, its poor magnetic properties have been an outstanding issue for many years. In particular, Ni is believed to be multidomain on the scale of micron-sized Josephson junctions. This multidomain structure can create out-of-plane stray fields that pin the free layer leading to inconsistent magnetic switching.

As another elemental ferromagnet, Fe was a natural candidate for an alternative fixed layer. This chapter will outline a study of Fe Josephson junctions to characterize the magnetic properties of the material in thin films at cryogenic temperatures as well as examine the $0-\pi$ transition and critical current of such junctions.

5.1 Magnetic Films

Before studying Josephson junctions directly, sheet films were grown to study the magnetic properties of Fe films at the nanometer thickness scale at low temperature. In most of the work done by this lab, a Cu buffer has been placed between Nb and the ferromagnets used; this has been shown to reduce the magnetic dead layer and improve switching. To see if this is necessary for Fe, two sets of films were sputtered. The first ranged from 0.5 nm to 1.9 nm Fe with 5 nm Nb above and below, and the second contained the same range of thicknesses with 2 nm Cu layers between the Fe and Nb. This sputtering run was done by Ben Byrd and Josh Willard.

The magnetic films were measured using a Quantum Design MPMS3 SQUID Magnetometer. Four-quadrant hysteresis loops sweeping from high positive field to negative and back up were measured at 10 K to determine the magnetic properties just above the Nb superconducting transition temperature. Fitting the hysteresis loops to an error function allowed the extraction of the saturation magnetization M_s, the coercive field H_c and the squareness of the loop which describes how cleanly the ferromagnet switches.

In summary, the magnetic properties were consistently better for the films grown with the Cu buffer. Extrapolating the saturation moment per area vs thickness line gave a lower x-intercept with Cu, suggesting that the spacer layer decreases the magnetic dead layer. The squareness was also higher with the Cu spacer, especially in the thinner films, indicating that the magnetic switching was cleaner. The films grown with Cu had lower coercivity. Although a high switching field is desirable for a fixed layer, the coercive field was high enough in both sets to warrant consideration given the low switching fields of a permalloy free layer, and the fact that the switching field is expected to be higher in an elliptical junction than in a large-area magnetic sheet film.

5.2 Fe Josephson Junctions

In order to characterize the supercurrent transmission and $0 - \pi$ transition thickness a range of Josephson junctions was fabricated covering the same thickness range. Based on the results of the film study a Cu spacer was included, with a final structure of the Nb/Al multilayer described previously as a bottom lead, the Cu(2)/Fe(x)/Cu(2) magnetic layer, and a Nb top electrode. A more thorough discussion of the measurement procedure for single junctions will be given in Chapter 6, here only an outline of the method will be given

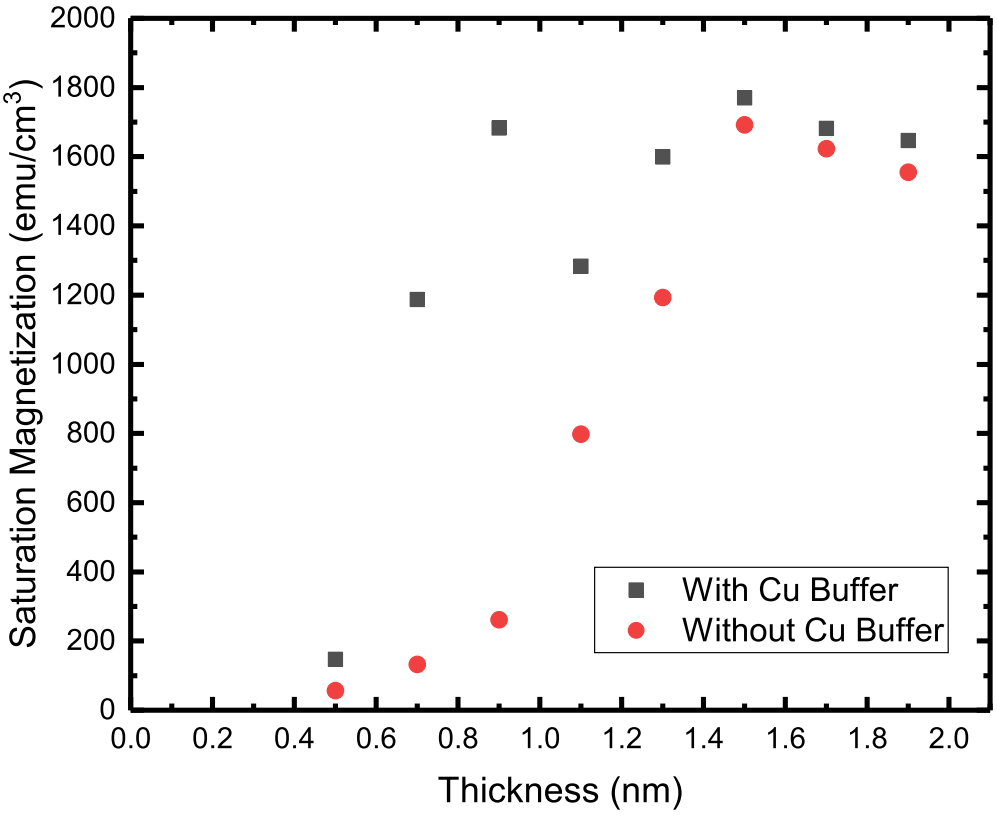

Figure 5.1: Saturation Magnetization of Fe films measured with (squares) and without (circles) a 2 nm Cu buffer layer. Including the Cu layer allows the films to maintain high magnetization at lower thicknesses. Data taken at 10 K.

in order to highlight the key results.

Fraunhofer patterns were measured from -600 Oe to 600 Oe. Before measurement of the upsweep a -1000 Oe field was applied in-plane to saturate the magnetization in a known state. Similarly a 1000 Oe field was applied before the downsweep.

The Fraunhofer patterns measured such as the one illustrated in Figure 5.2 were typical for a strong Ferromagnet in a Josephson junction. One of the key features was an offset between the upsweep and downsweep with the central lobe no longer centered at zero. Due to the internal magnetization, an external field is required to reach zero flux through the junction. At some point during each sweep, the applied field exceeded the coercive field of magnetic layer. At this point a switch is observed where the Fraunhofer pattern jumps from following the upsweep magnetization curve to the downsweep. In these junctions the switch occurred after the central peak was measured, so the maximum critical current could be read off directly from the data.

Josephson junction critical current was plotted vs thickness in order to characterize the $0-\pi$ transition. The critical current was multiplied by the normal-state resistance to give a voltage insensitive to small variations in sample area. The critical current of an S/F/S junction in the diffusive limit takes the form

$$I_c R_n = V_0 \exp(-d_f/\xi_{f1})|\cos(d_F/\xi_f 2 - \phi)| \tag{5.1}$$

where the minima correspond to transitions between a 0 and π ground state. Accordingly, the experimental signature for a $0-\pi$ transition is a sharp dip in the $I_c R_n$ vs thickness curve. Many of the junctions measured had extremely low critical currents, restricting the portion

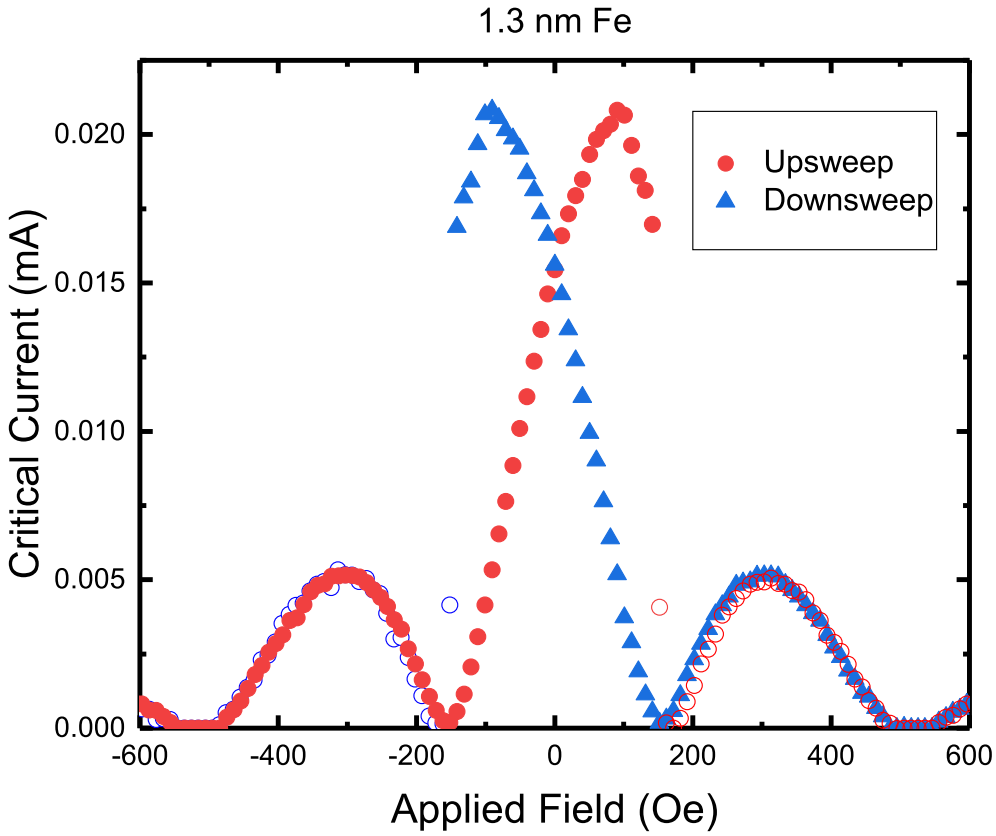

Figure 5.2: Fraunhofer pattern of Josephson junction with 1.3 nm barrier. The junction was initialized in the negative direction, the upsweep (red circles) measured, then initialized in the positive direction and the downsweep (blue triangles) measured. The central peaks are offset from each other because of the internal magnetization of the junction. When the switching field of the Fe layer is reached the critical current shifts to match the curve initialized in the other direction. Open symbols indicate the points that were acquired after the magnetic switching event.

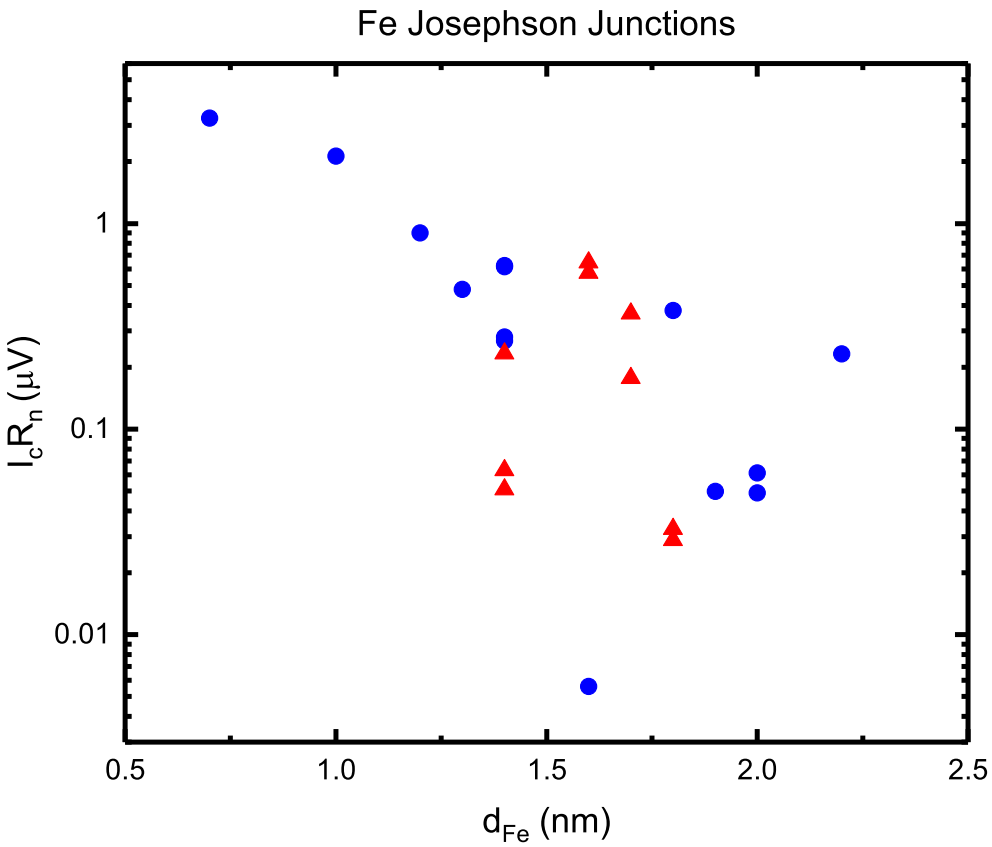

Figure 5.3: Variation of critical current with thickness for two series of Fe Josephson junctions. The expected signature of a $0-\pi$ transition would be a sharp local minimum in the critical current at the transition thickness. Although one point in the first series (blue circles) had a lower critical current this did not reproduce in the second run (red triangles). The overall magnitude of the I_cR_n product was very low, limiting the viability of Fe as a material for JMRAM.

of the curve that could be resolved to the thinner end of the curve*. The fab yield on the initial run was low, so a second set of junctions was made to supplement the data. Although the initial data showed a minimum at 1.5 nm this did not reproduce in the second series of junctions.

Ultimately, a $0-\pi$ transition was not conclusively identified in this project. While other groups have seen oscillations in the critical current through Fe [85, 86] those studies were

*Since these data were taken, improvements have been made to the measurement probe fixing a faulty ground connection. This has significantly reduced the effective noise temperature of the measurements, allowing smaller critical currents to be resolved. A future follow-up study could likely meaningfully improve these data, although the broader conclusions are unlikely to change

done at a much lower thickness resolution, looking only at one or two points per lobe. More importantly, the critical currents seen were much lower than those in Ni. As Fe was being investigated as a candidate to replace Ni as a fixed layer in a JMRAM spin-valve structure, this low critical current rules it out for application in the present form of memory under consideration. The clean magnetic switching seen in the Fraunhofer patterns was promising. Clearly, the search for materials combining the high supercurrent transmission of Ni with the beneficial magnetic properties of alloys such as permalloy remains an outstanding challenge in the field.

Chapter 6

CoGd Ferrimagnetic Josephson Junctions

6.1 Rare-Earth Transition-Metal Ferrimagnets

The rare-earth transition-metal alloys have seen a surge of research in recent years largely driven by their potential for application in spintronics [87, 88]. These alloys first began to attract interest in the 1970s as their domain structure showed promise for magnetic bubble memory [89]. Many of these alloys are ferrimagnetic, with the rare-earth and transition-metal atoms contributing antialigned magnetic moments. These alloys can be described well using a model treating them as two independent sublattices sharing a common Curie temperature [90]. These alloys are referred to as "compensated ferrimagnets" in the case that the net moments of the two sublattices cancel leaving zero magnetization [91,92]. In the case of the ferrimagnet CoFeGd this compensation has been shown to occur even in ultra thin films below 10 nm [93].

Much of the more recent investigation on the RE-TM alloys has focused on their ultrafast magnetization dynamics [94]. In addition to magnetic compensation, at a certain temperature T_A angular momentum compensation can be observed. Small changes in composition can have a significant effect on this compensation temperature [95]. The magnetic and angular momentum compensation do not occur at the same point because of the different g-factors of the two sublattices. At T_A both the Gilbert damping constant and the effective g-factor of the alloy diverge, potentially allowing very rapid magnetic switching.

An important insight into the transport properties of these alloys was work done by

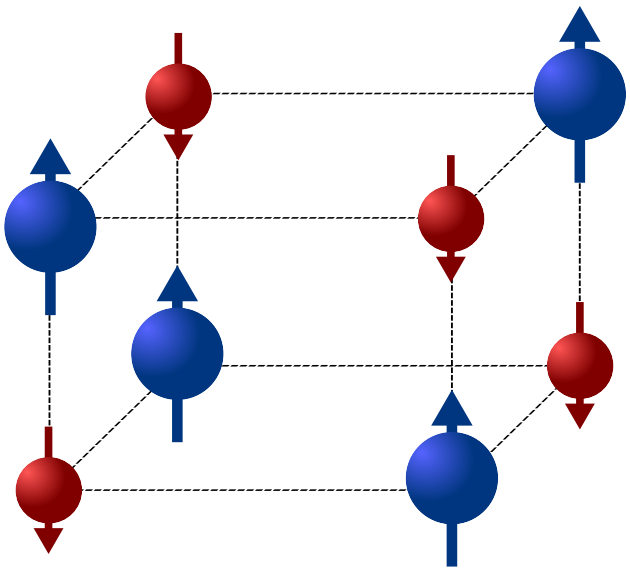

Figure 6.1: Structure of a ferrimagnet such as CoGd. The two species form sublattices with antiparallel magnetizations. A compensated ferrimagnet is the particular case where the total contribution from the two species cancel leaving zero net magnetization. Many RE-TM ferrimagnets are amorphous; the strucutre shown is for illustrative purposes.

Naylor, Burnell, and Hickey on the alloy $Co_{1-x}Gd_x$ [96]. That work used point-contact Andreev reflection (PCAR) measurement to probe the spin polarization of the conduction electrons. Their key observation was that even in the case that the alloy was compensated with near-zero net magnetization, the transport current was still spin-polarized.

The polarized transport current of a compensated ferrimagnet can be understood by considering the origins of magnetism and electron transport in the constituent elements. The rare earth (Gd here) gains its magnetic moment from $4f$ electrons. The half-filled $4f$ band lies deep below the Fermi level, and these electrons are highly spatially localized, so there is very low participation of Gd electrons in transport. In the transition metal (Co) the magnetic moment arises from d electrons near the Fermi level which are much more mobile.

The possibility of a strongly spin-polarized alloy with zero net magnetization raises interesting questions about potential applications in a superconducting context. Magnetic fields are intrinsically destructive to superconductivity, which is a natural downside to any appli-

cation of magnetic materials in a superconducting circuit. Projects such as the Ni/NiFe spin valves in Chapter 4 have shown inconsistent magnetic behavior, which we attributed to the stray magnetic field from the Ni domains. If a π junction could be made using a compensated ferrimagnet, it could allow the phase shift of a magnetic Josephson junction to be used in a device without the downsides caused by the stray magnetic field.

6.2 Target and Film Characterization

6.2.1 Preliminary cosputtering

Preliminary characterization of thin CoGd was done on films cosputtered and measured by Josh Willard as shown in Figure 6.2. In the bulk, $Co_{1-x}Gd_x$ is compensated near $x = 20\%$ at 4.2 K [92] but that value may change in very thin films [96]. Films were grown by cosputtering from Co and Gd targets in DC magnetron guns oriented at an angle onto a rotating substrate at room temperature. The Co sputtering power was fixed at 100W with the Gd power varied from 0 to 25 W. For every power used, one 3 nm film was grown for magnetic measurement and a 200 nm film was grown for EDX analysis to determine the composition. The films for magnetic measurement were encapsulated in the structure Nb(5)/Cu(2)/CoGd(3)/Cu(2)/Nb(5) to prevent oxidization of the Gd and give a surface similar to that used in Josephson junctions; early measurements showed a significant increase in magnetization when this cap was omitted.

MPMS3 SQUID Magnetometer measurements were used to measure the saturation magnetization of the CoGd films at 10 K. As compared to the bulk 20% Gd compensation point measured in thicker films [97], the 3 nm films showed the lowest magnetization (below 100 emu/cm^3) at $x = 24\%$. The main sputtering system with triode guns and 16 chip hold-

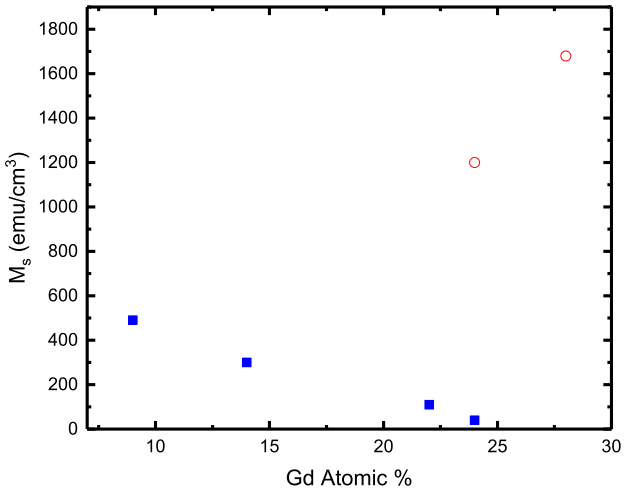

Figure 6.2: Saturation magnetization of cosputtered 3 nm CoGd films measured at 10 K. The 24% Gd film had a magnetization of only 40 emu/cm^3, suggesting that that concentration is very close to compensation for low temperature thing films. Open red circles indicate films that did not include a capping layer; their magnetization is much higher due to oxidization of the Gd.

ers does not have cosputtering capabilities, so for larger studies and for Josephson junction fabrication an alloy target made by ACI alloys was purchased. $Co_{76}Gd_{24}$ did not mix well when arc melted so the target was made from a sintered powder.

6.2.2 $Co_{76}Gd_{24}$ Sputtered films

Magnetic films were sputtered from the 76:24 target over a wide range of thickness from 1 nm to 9 nm. The films were sputtered using a triode gun with a target voltage of 250 V and an anode current of 0.33 A based on sputtering parameters used for Co. Oxidization can cause for the Gd to be magnetically deactivated [98] so the films for the magnetometer were again encapsulated in Nb and Cu. As shown in Figure 6.3 none of the films in that series showed a saturation magnetization below 350 emu/cm^3. The magnetization was nearly constant above 3 nm but increased sharply for the thinnest films.

The difference in moment measured in the cosputtered films vs the alloy target films sug-

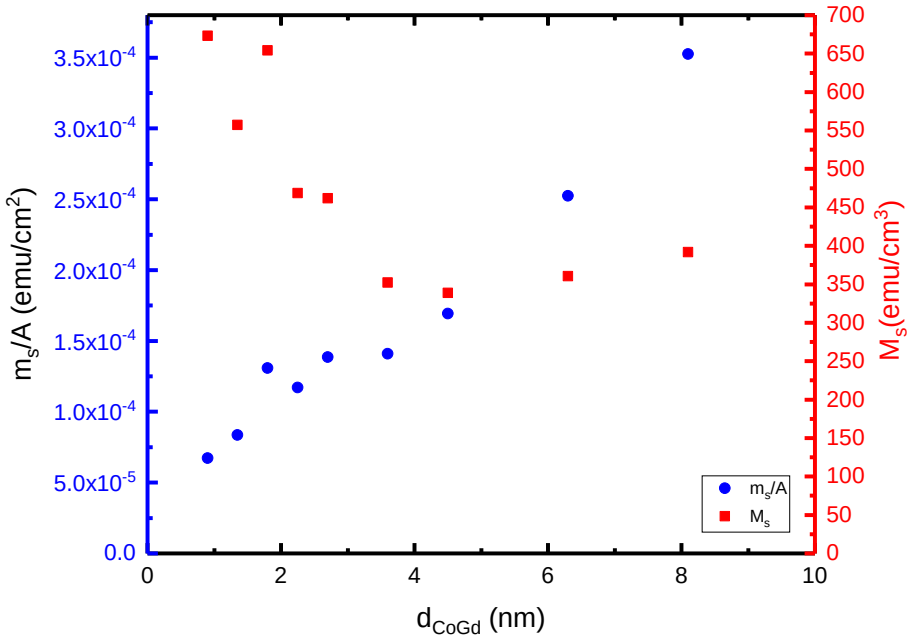

Figure 6.3: Saturation magnetization of films sputtered from $Co_{76}Gd_{24}$ target measured at 10 K. Red squares indicate moment per volume and blue circles moment per film area. The lowest magnetization observed, 350 emu/cm^3, was higher than the minimum observed in cosputtered films suggesting that these films were not compensated and that the composition may not have been the same as the nominal target value.

gested that the films sputtered from the alloy target did not have the intended composition. Elemental analysis was performed by energy dispersive x-ray (EDX) on two films sputtered from the alloy target and found that the films were $19.19 \pm 0.27\%$ Gd. A possible interpretation of this discrepancy is that the relative sputtering rates of Gd and Co from the target may not be the same, causing the films to have a different composition from the target.

To increase the amount of Gd in the films, a second series was measured with a higher sputtering power to attempt to raise the relative sputtering rate of Gd. The target voltage was raised to 500 V and the anode current to 0.5 A. The saturation magnetization of the films sputtered in that run is shown in Figure 6.4.

The CoGd films sputtered at a higher power showed much low saturation magnetizations

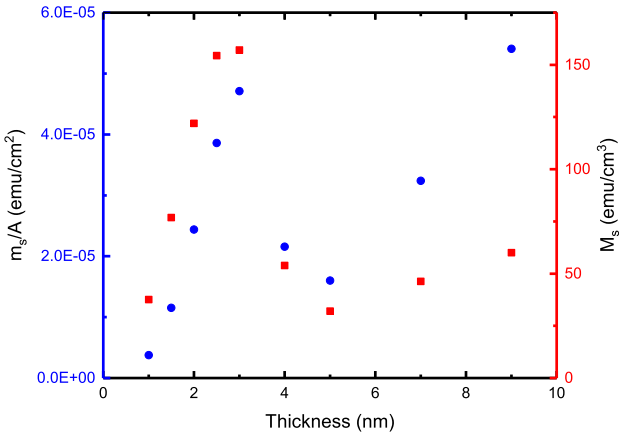

Figure 6.4: Saturation magnetization of films sputtered from $Co_{76}Gd_{24}$ target at 500 V. The lower magnetizations than in Figure 6.3 are because the concentration of the sputtered film is closer to the alloy's compensation point. The moment was measured with an in-plane field at a temperature of 10 K. The heat produced sputtering at higher voltage caused the target to crack during the sputtering run. Blue circles indicate moment per area, red squares moment per volume.

than the previous set at 10 K, getting as low as 32 emu/cm^3 at 5 nm thickness. Thicker CoGd films tend to show an out-of-plane magnetic anisotropy; we attribute the change in the trend above 4 nm to this change in direction. Unfortunately, due to the increased heat generated by sputtering at higher power, the sintered target significantly cracked during this sputtering run. EDX analysis of films at this higher power showed a Gd concentration of $27.1 \pm 1.1\%$. Further attempts to use this target caused the solder holding it to the target base in the sputtering system to wick through the crack, causing contamination and variations in composition.

In order to grow films closer to the compensation point without needing to sputter at high voltage, a second target was ordered. The new target was chosen to have a nominal Gd concentration of 30%. As the nominal 24% target gave films with only 19% Gd at 250 V we aimed higher that the desired film concentration, intending for the 30% target to give films closer to 24%. This film was epoxy bound to a Cu backing plate by the manufacturer to protect it from strain due to thermal expansion.

6.2.3 Sputtering Voltage and Temperature Dependence

To characterize the new nominally $Co_{70}Gd_{30}$ target, films were sputtered at 250 V, 300 V, and 350 V with the anode current fixed at 0.3 A. 200 nm CoGd films were sputtered for EDX analysis and Nb(5)/Cu(2)/CoGd(3)/Cu(2)/Nb(5) films for measurement in the magnetometer.

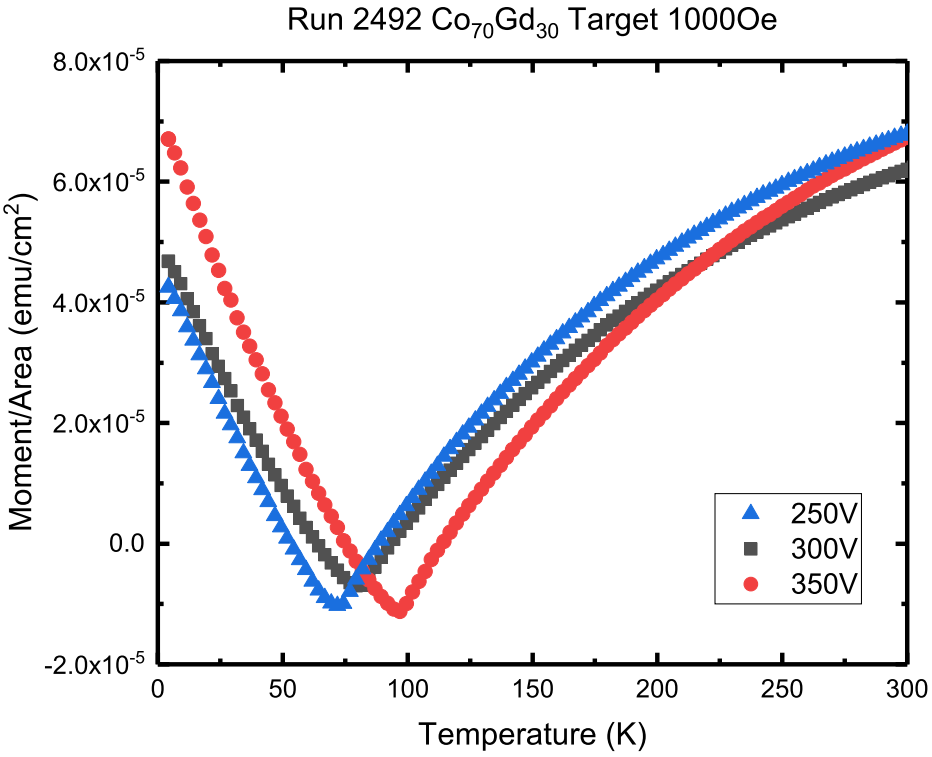

Figure 6.5: Magnetic moment vs temperature for different CoGd sputtering voltages. Increasing the sputtering voltage causes a large change in compensation temperature even if the changes in composition seen by EDX analysis are small. The moment goes below zero because of the diamagnetic contribution from the Si substrate.

For the magnetometer measurements, the applied field was fixed at 1000 Oe and the temperature swept from 4 K to 305 K. The high applied field was used to set the direction of the magnetization and ensure that the films were saturated. Each of these curves shown in Figure 6.5 started with a positive moment, steeply decreased with temperature to a minimum at the compensation temperature T_{comp}. The form of the M vs T curves can be understood

following the arguments of Ref. [90], in which the individual sublattice magnetizations of an RE-TM ferrimagnet were measured using an element-specific x-ray magnetic circular dichroism technique. The results of that study are reproduced in Figure 6.6. The magnetization as a function of temperature for for either constituent element follows a power-law form

$$M(T) = M(0)(1 - \frac{T}{T_c})^{\rho} \tag{6.1}$$

where T_c is the Curie temperature of the alloy and ρ is a critical exponent particular to that sublattice. The transition metal with a lower ρ rises quickly in moment as temperature is decreased below T_c. The rare-earth has a higher critical exponent so the antiparallel Gd moment increases in magnitude more linearly as temperature decreases, eventually crossing the Co magnetization at the compensation point. The resulting net magnetization has two zeros, one at the compensation point where the sublattices cancel and one at the Curie temperature where both go to zero.

As seen in Figure 6.5 increasing the sputtering voltage caused a corresponding increase in the compensation temperature where the minimum was observed. 200 nm films were grown in the same run for elemental analysis. EDX analysis was done by measuring four points on each chip and averaging. As shown in Table 6.1 all of the films appeared to have a higher Gd concentration than the nominal value of the target, unlike in the 250 V films from the original target. Increasing the sputtering voltage caused a small increase in the Gd concentration going from 250 to 300, but the change from 300 to 350 could not be resolved by the EDX measurements. Apparently even very small changes the composition can have a noticeable effect on the compensation temperature. The compensation temperatures seen here were in the range of 70 to 100 K, much higher than the 4.2 K liquid helium temperatures where a

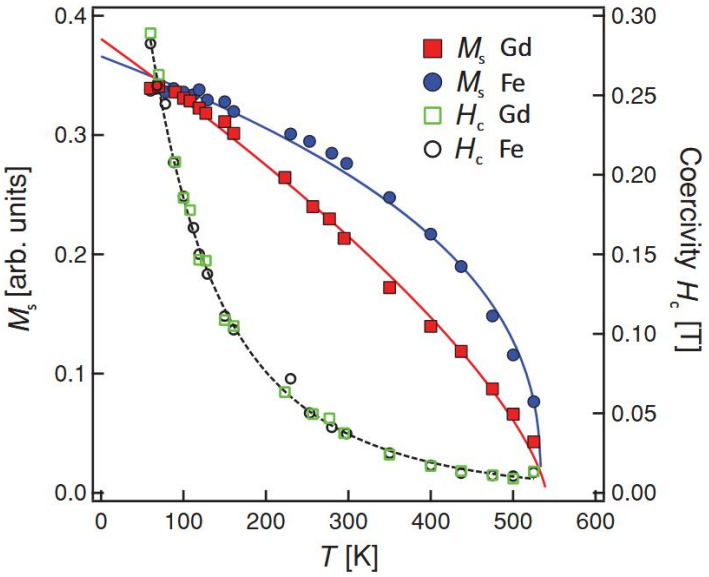

Figure 6.6: Sublattice magnetizations of a rare-earth transition metal ferrimagnet. The sublattices share a common Curie temperature, but their magnetizations increase with different critical exponents as temperature decreases. The point where the antiparallel magnetizations of the rare earth (red squares) and transition metal (blue circles) are equal and cancel is the compensation temperature. Reproduced with permission from Ostler et al. [90]

superconducting device would be operated. However up until this point only 3.0 nm films were measured and the effect of film thickness both on compensation and on the Josephson junction $0-\pi$ transition must be considered to find the ideal point in thickness-temperature-composition parameter space for the compensation point.

Voltage	250	300	350
Gd %	31.1 ± 0.7	32.5 ± 1.0	32.3 ± 0.6

Table 6.1: Effect of sputtering voltage on CoGd composition on films grown from a nominally 30% atomic target. Increasing the Gd concentration raises the compensation temperature, as also illustrated in Figure 6.5. Values were calculated by averaging measurements at four points on each film. Films for EDX analysis were 200 nm thick. Although the difference between the 300 V and 300 V could not be resolved within the uncertainty of these EDX measurements the change in compensation temperature suggests there was still an increase in Gd concentration at higher sputtering voltage.

The magnetic and EDX results from the two different targets are somewhat difficult

to reconcile. At low sputtering power, the films sputtered from the 76:24 target did not show compensation at all in the range studied, with the sputtered films appearing Gd-poor compared to the nominal target values. Increasing the Gd concentration of the target increased the compensation temperature from too low to see to over 50 K. It is possible that the difference between the target compositions was larger than expected, either due to the 76:24 target actually having less than 26% Gd (closer to the 19% seen in the first films) or the 70:30 having more Gd than intended. Elemental analysis of the targets by a more accurate method such as inductively coupled plasma could give a clearer picture of the exact stoichiometry but was prohibitively expensive for use on Gd and requires an amount of material that would be destructive to the sputtering target.

6.3 Magnetic Measurement

To characterize the compensation temperature of nominal Co_70Gd_30 a series of films were sputtered using the $Co_{70}Gd_{30}$ target in thicknesses ranging from 0.7 nm to 2.0 nm. The chips were sputtered in a random order to decouple any drift in sputtering parameters from film thickness during the run. The moment was measured in a 1000 Oe in-plane applied field. MPMS3 measurements were taken with a 6 s integration time in VSM mode with a peak amplitude of 5 mm while the temperature was swept continuously at $5\,\mathrm{K\,min^{-1}}$ from 2 K to 305 K. Due to the very small magnetic moment near compensation the sample transport and chamber were cleaned with alcohol at the beginning of each run to avoid contamination from any magnetic powders or other contaminants in the magnetometer left by users from other research groups on the shared instrument.

The Quantum Design MPMS3 SQUID magnetometer has an auto-tracking feature to

account for the thermal expansion of a sample holder when measurements are taken while changing temperature. Because the straws used to hold the chips were not provided by Quantum Design and did not necessarily have the same material properties, this auto-tracking was disabled for the temperature sweeps. To ensure that the moment was most accurate in the area of interest (near helium temperatures) the samples were centered after cooling to 10 K. A 200 Oe centering field was used; this was high enough to induce a ferromagnetic signal from the film without being drowned out by the diamagnetic background of the substrate.

When measuring moment vs temperature on a CoGd film, the measured moment goes below zero at the minimum near T_{comp} due to the diamagnetic background from the Si substrate. At a single temperature this diamagnetic background can easily be removed by subtracting out the linear portion of an M vs H curve; doing so for the whole moment vs temperature series would require measuring the field dependence at every temperature for every thickness. For a faster background subtraction, a blank Si chip from the same wafer as the sample substrates underwent the same measurement procedure as the CoGd films.

As shown in Figure 6.7 the diamagnetic signal of the Si substrate had a steep negative slope at temperatures below 30 K and a more gradual positive slope at higher temperature. The substrate measurement was used to parameterize an interpolating function in Mathematica using a spline method. After scaling for the difference in chip and reference substrate areas this interpolation was subtracted out of the measured moments to give only the contribution from the CoGd films.

Figure 6.8 shows the dependence of magnetization on temperature for various CoGd films. Reading from low temperature to high, all of the curves show a decreasing moment below T_{comp}, then a minimum followed by an increasing moment as the temperature is raised.

In the thinnest films, it is immediately apparent that even at the local minimum in

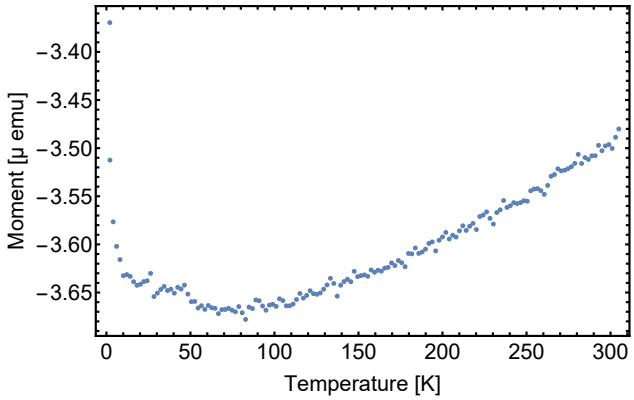

Figure 6.7: Measured background of Si substrate in a 1000 Oe in-plane applied magnetic field. The chip used for this measurement was cut from the same wafer the magnetic films were grown on. The small diamagnetic signal increases gradually with temperature except for a region with a steep negative slope below 30 K. This background causes the measured magnetization of the CoGd films to go below zero at the compensation point, and was subtracted out (normalized by film area) from the final magnetization vs temperature curves in Figure 6.8.

moment the magnetization remains positive. In these films the signal did not go below zero even in the raw data before subtracting out the diamagnetic background. The fact that there is still a minimum in the M vs T curve suggests that the ferrimagnetic coupling between the sublattices is still present in these films as some partial cancellation is observed. We speculate that in these very thin films below 1 nm, which are likely rougher and less uniform the, Co and Gd sublattice moments are not perfectly colinear, leaving a residual magnetization even at the compensation temperature.

As the thickness of the films increases, the compensation temperature rises quickly as shown in Figure 6.9. For the films below 1.5 nm the films are at least near compensation, but as the films approach 2 nm the compensation temperature reaches 70 K and above. Clearly referring to CoGd as a compensated ferrimagnet is strongly dependant on the temperature and exact thickness in ultra thin films.

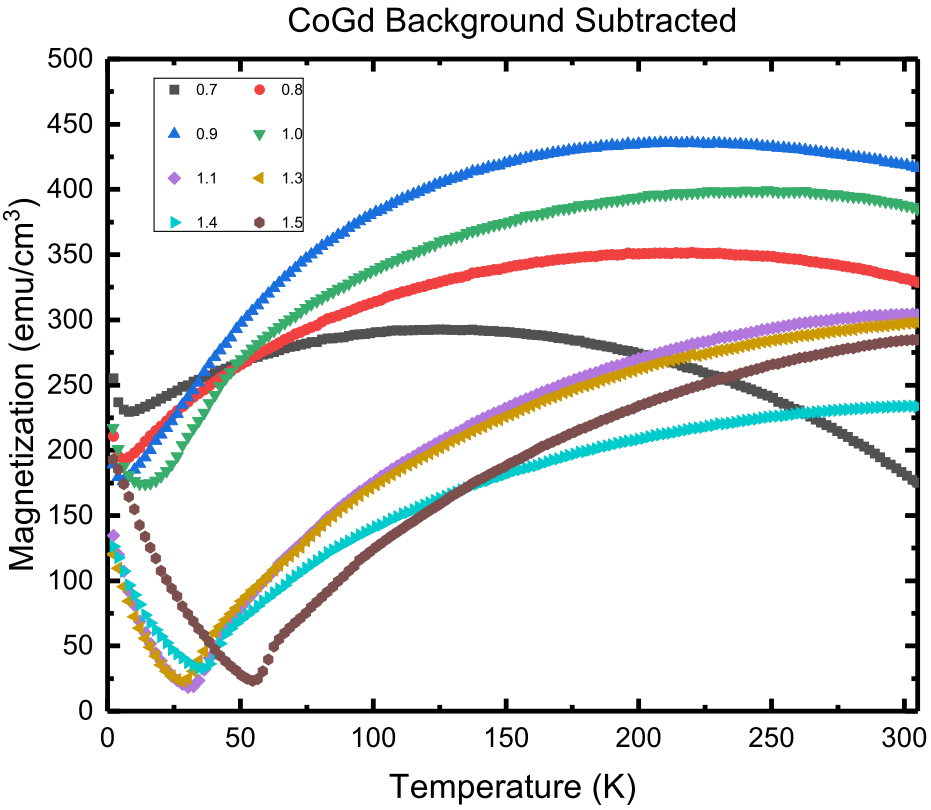

Figure 6.8: Magnetization vs temperature curves for CoGd films of various thicknesses. At low temperature, the magnetic moment is dominated by the contribution from Gd. As temperature increases, the relative contribution of the antiparallel Co increases until they cancel at the compensation temperature, leaving minimal magnetizaiton. Above that temperature the Co contribution dominates and the magnetization increases until the temperature begins to approach the Curie temperature of the alloy above room temperature. The compensation temperature depends strongly on thickness, with the films having their compensation temperature in the 10 K range used for superconducting devices only at sub-nanometer thicknesses. In the thinnest films, the magnetization does not go to zero at the minimum, suggesting that there is nonuniformity in such thin films or the sublattices are no longer truly colinear, but a minimum magnetization defining a compensation temperature is still observed.

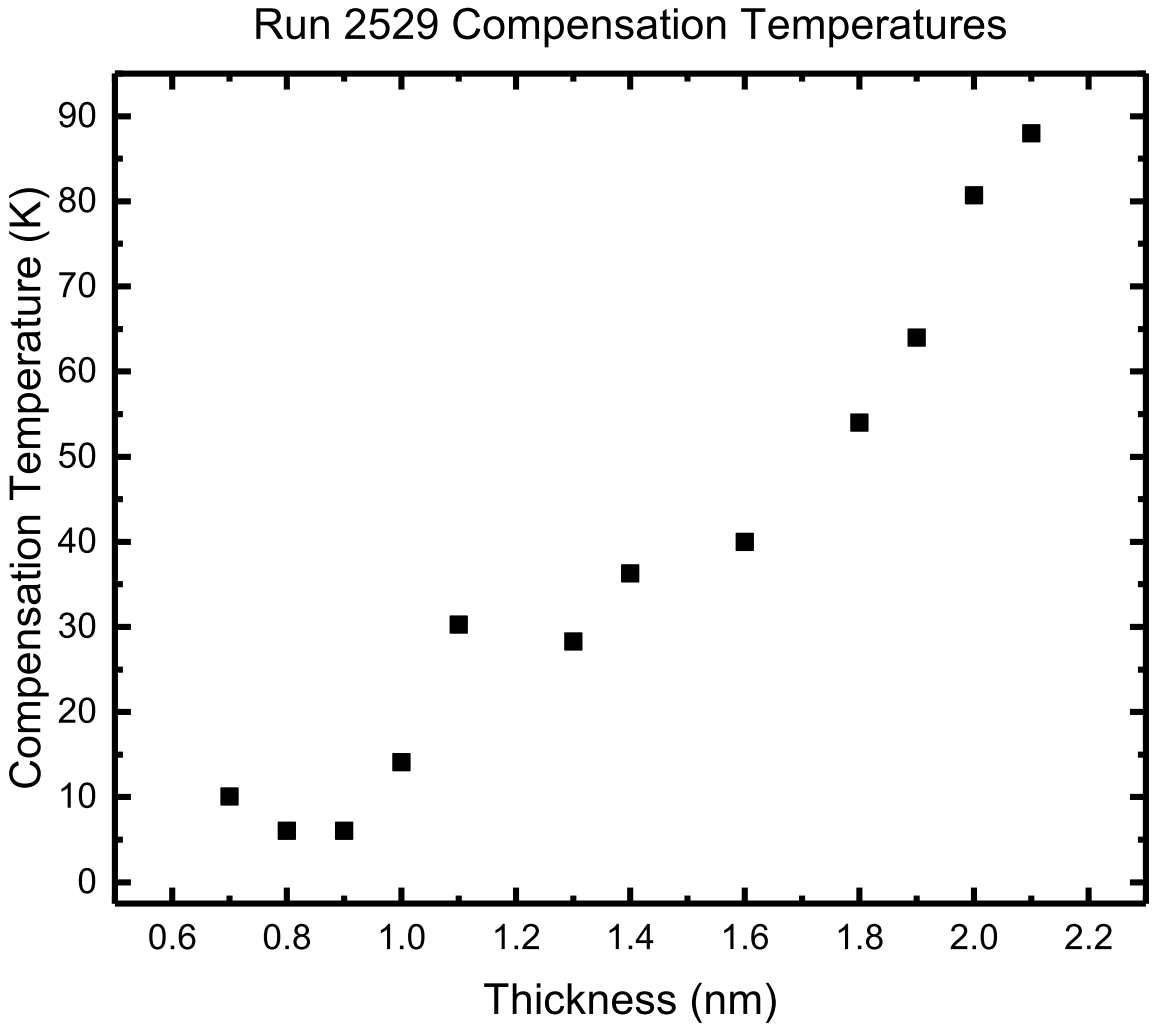

Figure 6.9: Compensation temperature of CoGd films of different thicknesses. The compensation temperature is taken as the local minimum in the magnetization vs temperature curve at $-1000\,\mathrm{Oe}$.

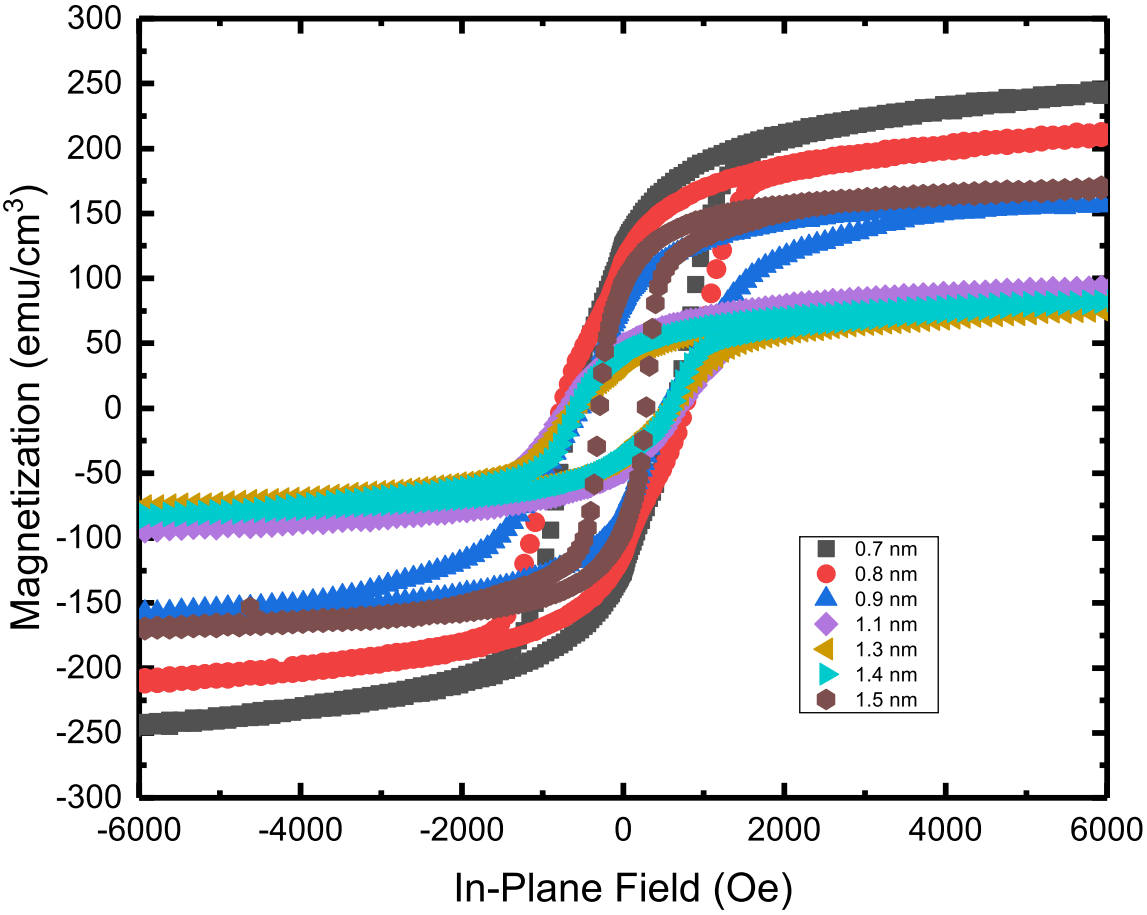

Figure 6.10: CoGd Magnetic Film Hysteresis loops at 4 K. The linear slope due to the diamagnetic background has been subtracted out.

6.3.1 Hysteresis Loops

After cooling the films for the measurement of the temperature dependence, hysteresis loops were measured at 10 K. The temperature was chosen to avoid the Meissner effect response from the Nb base layer superconducting. The field was swept from −10 kOe to 10 kOe and back in a four-quadrant measurement. A subset of these curves are shown in Figure 6.10. The intermediate thicknesses around 1.2 nm showed the lowest saturation magnetization as their compensation temperature was closest to 10 K. The samples at both the thinner and thicker end of the range had higher magnetization due to being further away from compensation at 10 K or due to the impartial compensation noted in Figure 6.8.

Clearly, the compensation point depends strongly on the exact thickness of the sputtered film. For transport measurements on Josephson junctions, a single composition sputtering target would not be able to provide films that are exactly at their compensation temperature at 4.2 K for the whole thickness range. Since using a different composition sputtering target for every thickness would be impractical, we elected to use the nominally 30% Gd sputtering target for the entire Josephson junction study, accepting that in the approximately 1 – 2 nm range the junctions would at least be low moment if not fully compensated.

6.4 CoGd Josephson Junctions

Josephson junctions with a CoGd barrier were grown over the same range of thicknesses as the magnetic sheet films. Two sets of junctions were made in independent fabrication runs. The junctions themselves were 0.5 μm^2 ellipses. The sputtered stack was $[Nb(25)Al(2.4)]_3$/Nb(20)/Cu(2)/CoGd(x)/Cu(2)/Nb(5)/Au(15), using the same smooth Nb/Al trilayer for the bottom electrode as described in Chapter 4.

6.4.1 CoGd Fraunhofer Pattern

Transport measurements were done at 4.2 K in liquid helium using the QD-1 SQUID-based measurement probe. As the junctions typically had critical currents on the order of 10 µA the current supply was run on the lowest range (100 µA). The nominal current step size used was 1 µA but this was lowered to 0.5 or 0.1 µA as necessary for samples with smaller critical currents to ensure that the zero voltage state could clearly be observed. The IV curves were swept as high as possible without exceeding the voltage limit of the measurement SQUID electronics as getting more data above I_c where the curve becomes linear allows a more accurate extraction of the normal-state resistance when fitting. The typical voltage

limit used was 3 V after a voltage gain of about 2×10^7 The voltmeter reading the amplified signal from the SQUID electronics was on a 10 V scale with a resolution of 0.000 03 V to give an integration time of one power line cycle. The junctions were initialized in a −1000 Oe applied in-plane field to saturate the CoGd layer and begin in a known magnetic state. For these single-junction measurements, IV curves were taken as a function of applied field to measure the Fraunhofer pattern of the junction (as compared to the technique in Chapter 4 where the field was returned to zero before each measurement). The field was swept from −800 Oe to 800 Oe in steps of 10 Oe to observe at least the second side lobe of the Franhofer pattern. A downsweep was then measured, initializing at 1000 Oe then sweeping from 800 Oe −800 Oe. Each IV curve was fit with the square-root form of the RSJ model to extract the critical current, such as shown in Figure 6.11. For I-V curves with small critical currents on the order of 1 µA there was some thermal rounding at low current, but not to the extent that the critical current could not be resolved. A full treatment of the I-V characteristics of Josephson junctions in the presence of thermal rounding is given in Ref. [99], but fitting that model is computationally intensive and only necessary if the rounding is severe enough that the zero voltage state is not observed directly in the measurement.

The Fraunhofer pattern of each junction was plotted as critical current I_c vs applied field as illustrated in Figure 6.12. In a ferromagnetic junction, the internal magnetization of the junction causes an offset of the Fraunhofer pattern's central lobe due to the additional field needed to reach zero flux through the junction. The CoGd junctions showed little to no offset between the upsweep and downsweep, indicating that the magnetization of the junction was very low. Even though at these thicknesses CoGd is not exactly at its compensation point at 4.2 K it still behaves as a low-magnetization material in a Josephson junction.

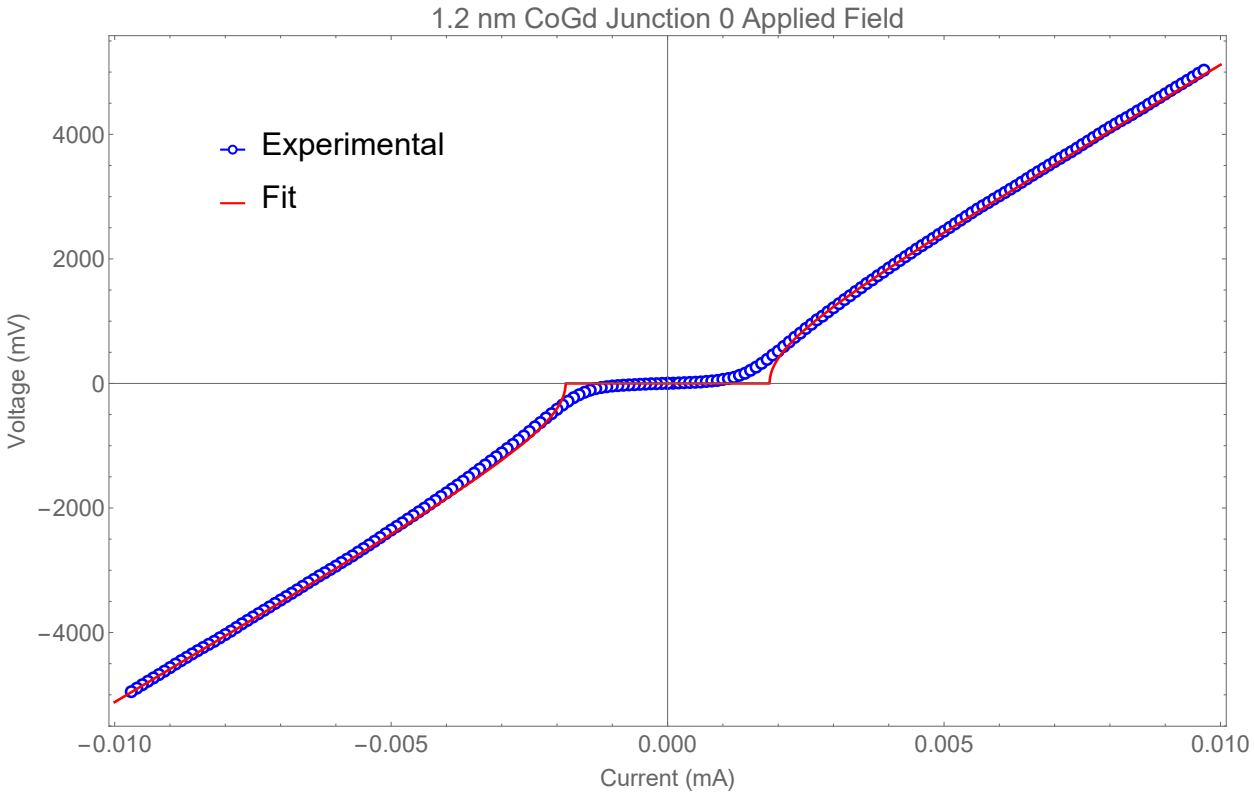

Figure 6.11: I-V curve of CoGd Josephson Junction. Blue circles are experimental data; the red line is a fit to the RSCJ model. Noise and thermal affects manifest as rounding at low current causing deviations from the curve near the critical current I_c. The critical current where the voltage becomes nonzero is still apparent despite the thermal rounding so a full treatment is not necessary. If the critical current is smaller or the effective noise temperature higher a fit such as the technique described by Ivanchenko and Zil'berman [99] can be used to fit the thermal rounding.

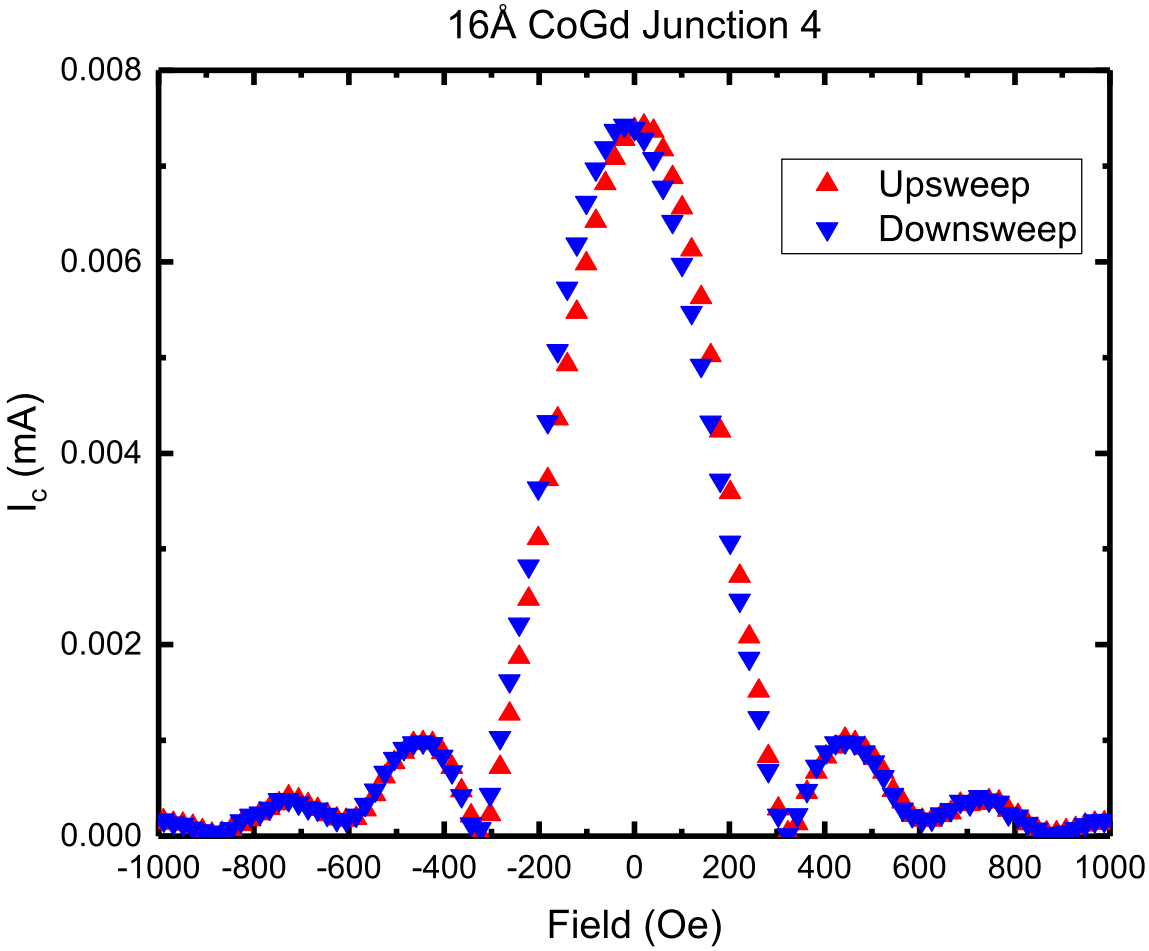

Figure 6.12: Fraunhofer pattern of a Josephson Junction with a 1.6 nm CoGd barrier. Both the upsweep and downsweep lie almost directly on top of each other, indicating that the junction has very low internal magnetization. The critical current is large enough to resolve the third side lobe on both sides.

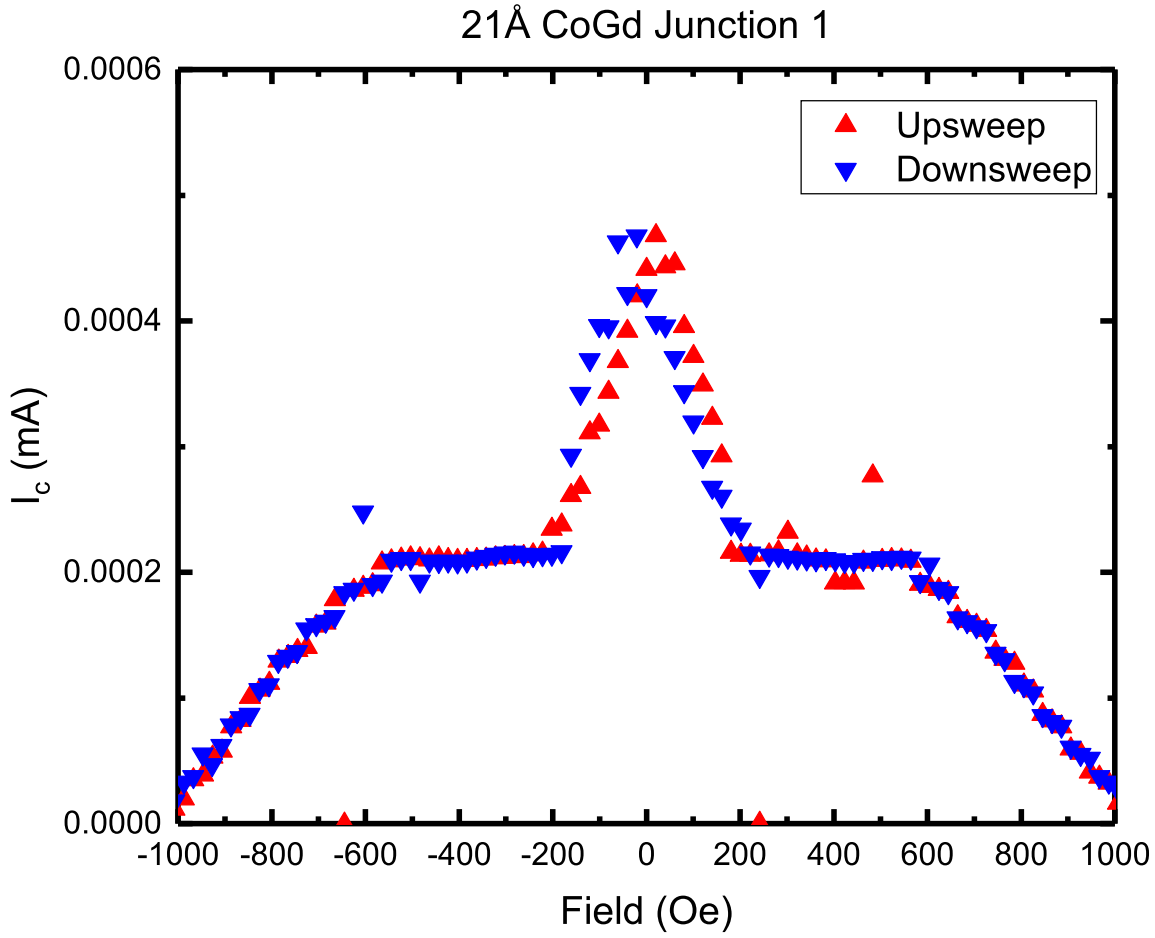

Figure 6.13: Fraunhofer pattern of a Josephson Junction with a 2.1 nm CoGd barrier. At this thickness the critical current is significantly reduced. A central peak can still be resolved, but the data are much noisier and no side lobes are visible. The effect of the internal magnetization is more pronounced here, appearing as an offset between the upsweep and downsweep.

6.4.2 CoGd IcRn Thickness Dependence

In all of the Fraunhofer patterns measured, the maximum critical current at the central peak was observed directly in the data set, there was no shift or magnetic switch obscuring the peak requiring extrapolation. The maximum critical current was tabulated for the full thickness range, taking data from at least two junctions per thickness on chips from both fabrication runs. The critical current was multiplied by the normal-state resistance to give a characteristic voltage I_cR_n independent of minor variations in sample area during fabrication. The dependence of I_cR_n on barrier thickness is shown in 6.14

Several features immediately jump out in the thickness dependence. The data visibly show a sharp decrease at 1.2 nm. This was originally seen in the measurements on the chips from the first fabrication run (blue stars), which motivated the fabrication of the second run (red squares) where the same feature was observed. This minimum is suggestive of the transition between a 0 ground state and a π ground state (or vice versa). At very low thicknesses, the decay with thickness is very steep, leading to small voltages at even modest thickness. The 1.7 nm junctions on the one chip from the first run at that thickness showed unusually high critical current, but this did not reproduce in the second run. This was likely the result of an error in the sputtering process, but it is shown for completeness. The bottom panel of Figure 6.14 shows the normal state resistances of the junctions. R_n was calculated by going to the point on the Fraunhofer pattern where the critical current was smallest and using the slope of that linear IV curve.

In a S/F/S magnetic Josephson junction in the diffusive limit, the dependence of critical current on thickness takes the general form

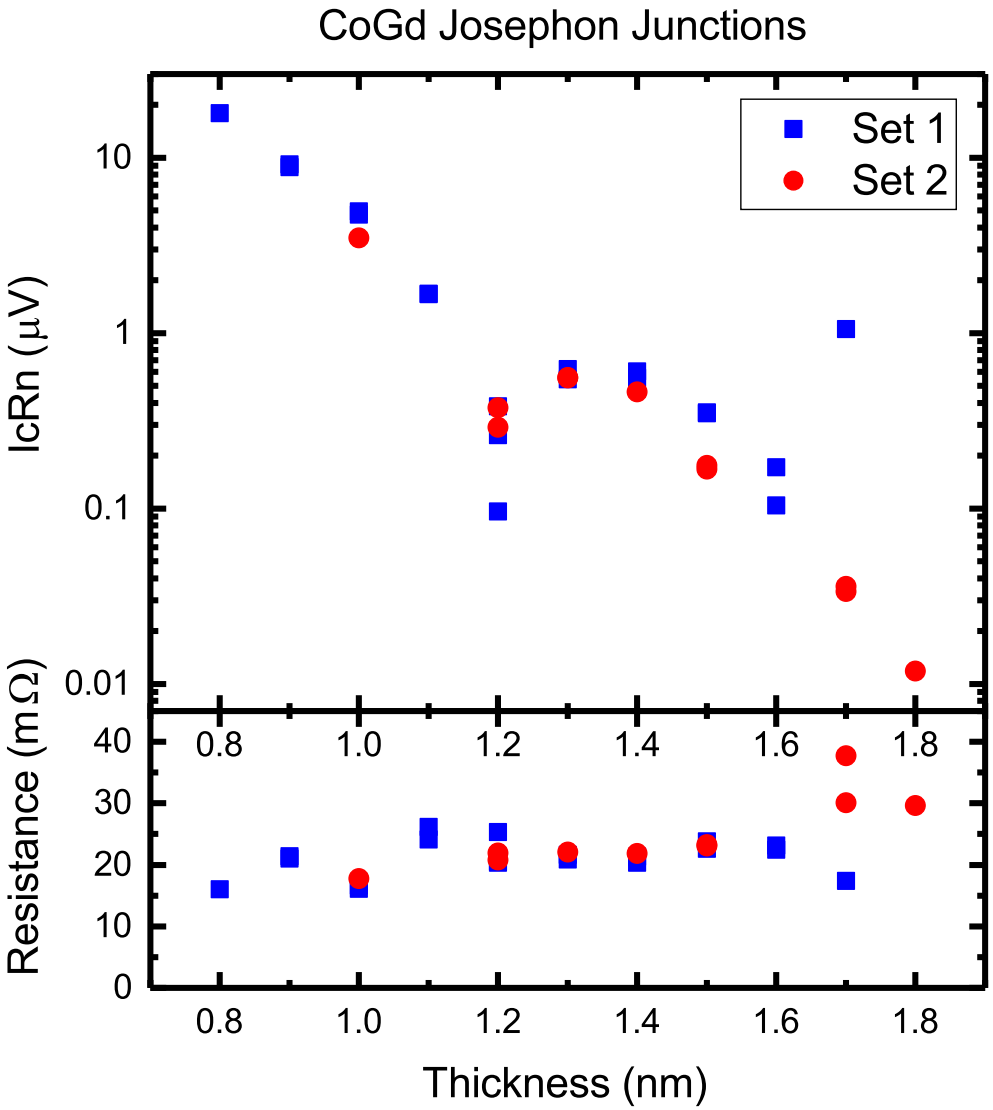

Figure 6.14: Dependence of characteristic voltage I_cR_n on CoGd Josephson Junction barrier thickness. The minimum at 1.2 nm is indicative of a transition between phase states. Blue squares and red circles represent junctions from chips in two different fab runs. The abnormally high critical current at 1.7 nm did not reproduce in the second set and is believed to be the result of a sputtering failure. The bottom panel shows the normal state resistances of the junctions. The resistance was taken from a minimum on the Fraunhofer pattern where the IV curves were closest to linear. The low scatter around 20 mΩ shows that the junctions areas were all very similar; the resistance of junctions this small largely arises at the interface and depends only weakly on thickness.

$$I_c R_n = V_0 \exp\left(\frac{-d_f}{\xi_{f1}}\right)\left|\cos\left(\frac{d_f}{\xi_{f2}} - \phi\right)\right| \tag{6.2}$$

where d_f is the F layer thickness and ξ_{f1} and ξ_{f2} are the length scales governing the decay and oscillation respectively. In the diffusive limit, the overall phase shift is expected to be $\phi = \frac{3\pi}{4}$ but this value is also very sensitive to the nature of the interfaces and any nonmagnetic spacer layers [79]. As there are two free parameters inside the cosine, both ξ_{f2} and ϕ cannot be uniquely specified unless at least two $0 - \pi$ transitions are observed.

The I_cR_n data were fit to Equation 6.2 as shown in Figure 6.15. The line of best fit is shown as a solid black line. This fit implied that the minimum at 1.2 nm is actually the second minimum of the oscillation, meaning that it is a $\pi - 0$ transition rather than the expected $0 - \pi$. Constraining the first minimum of the fit to fall at 1.2 nm gives the fit shown as a dashed red line. While it does not capture the exponential decay well at short thicknesses, this fit is comparable and without more data resolving additional thicknesses a concrete claim cannot be made about which model is better. The fit parameters are summarized in Table 6.2. The success of this model at all is strong evidence that a transition between the π and 0 states occurs so a π junction can be made with this material.

The overall magnitude of the critical currents in Figure 6.15 are very low; in the second lobe (presumed π state) I_c was below 30 µA at the peak. This is consistent with the very short decay length ξ_{f1}. In commonly used ferromagnetic materials such as permalloy the decay length can be as long as 0.76 nm [82], allowing a large critical current even in the π state. As sputtered CoGd in this thickness range is amorphous there is likely significant scattering decreasing supercurrent.

Comparing the Josephson junction data to the magnetic film results shows there is some

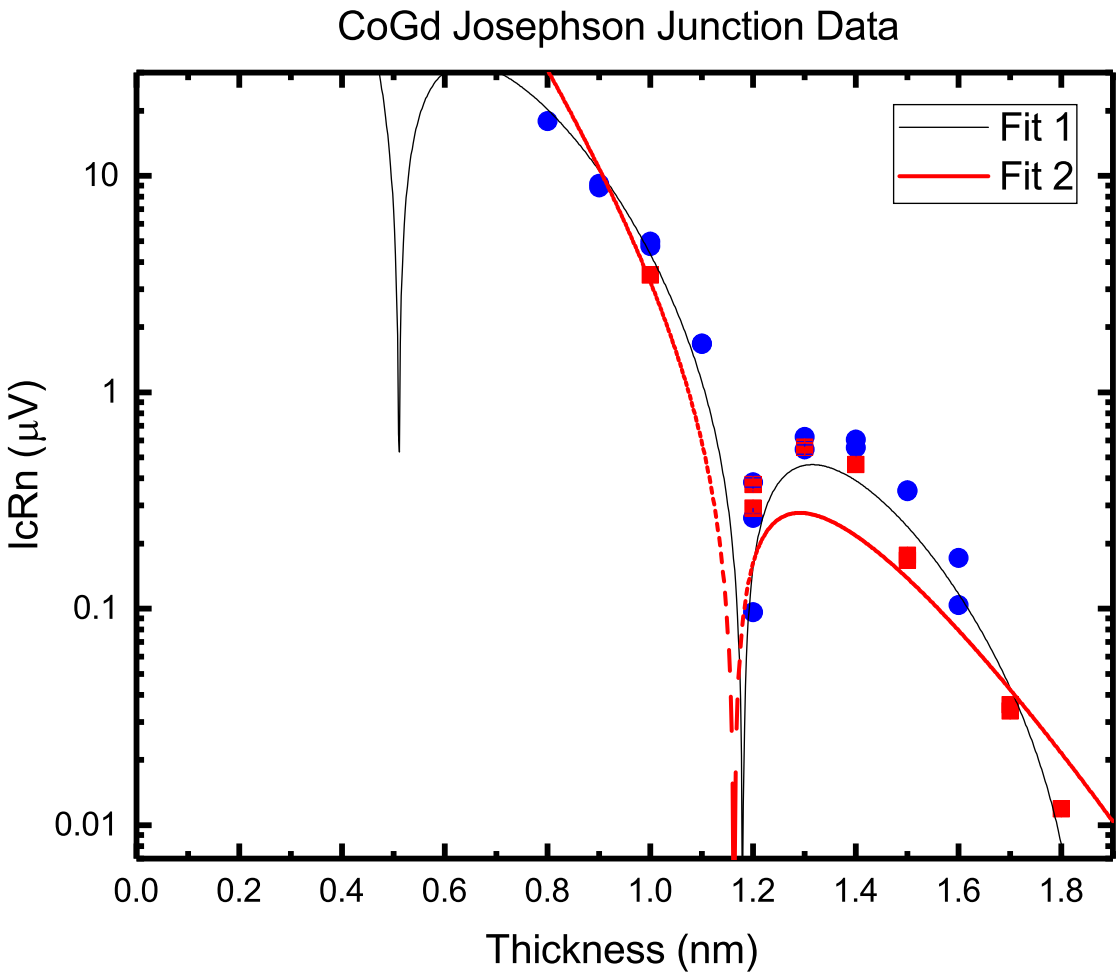

Figure 6.15: Fits to CoGd $0-\pi$ transition data. The best-fit line (black, solid) suggests that the minimum at 1.2 nm is actually the second minimum at a $\pi-0$ boundary. An alternative fit (red, dashed) was done constraining that minimum to be the first transition thickness.

Parameter	Free Fit	Fixed Fit
V_0	3380 ± 1250	20800 ± 8500
ξ_{f1}	0.157 ± 0.006	0.130 ± 0.005
ξ_{f2}	0.213 ± 0.009	0.5
ϕ	0.828 ± 0.240	0.754 ± 0.020

Table 6.2: Best-Fit Paramaters for CoGd $0-\pi$ transition. The best fit with all paramaters free shows that 1.2 nm minimum illustrated in Figure 6.15 is the second transition thickness. The second fit was done with ξ_{F2} fixed to force that minimum to be the first for comparison.

subtlety to the relationship between magnetization and thickness. Evidently, the compensation temperature varies dramatically with even small changes in thickness. As the films grow thicker T_{comp} becomes much higher than the 4.2 K temperature used for the transport measurements. In fact, below 1.0 nm compensation isn't observed at all, instead there is still a positive moment at the local minimum. Evidently the magnetization of the material must vary significantly across this range of thicknesses. All the same, the Josephson junction data fit a theoretical model that does not include any variation of fit parameters with thickness remarkably well. An intriguing possibility for a follow-up experiment would be a study of a Josephson junction series with slightly varying compositions to keep each thickness at its own compensation point. Realistically this would be extremely difficult until the characterization of the compensation temperature in ultra-low films becomes much more mature.

Seeing a $0 - \pi$ transition in a rare-earth transition metal ferrimagnet provides evidence that the alloy is behaving similarly to a ferromagnet in terms of the electron pair phase shift across the junction despite the near-zero magnetization. To make a RE-TM π junction viable in electronics, materials and interface optimization to allow higher critical currents would be a crucial next step.

Chapter 7

Conclusions

Throughout this dissertation, magnetic materials were studied for applications using Josephson junctions with a π ground-state phase difference. It is already both theoretically understood and experimentally demonstrated that a magnetic Josephson junction with two ferromagnetic layers can be engineered to have a different phase state in the parallell and antiparallel orientation. Previous study of Ni/NiFe spin valves by our group demonstrated $0 - \pi$ switching but those data were difficult to interpret without a fairly involved fitting process to extract the phase difference. To address the SQUID fitting ambiguity issues, in this study new SQUID designs were used. These SQUIDs had much lower inductances and greater symmetry, greatly reducing the distortions in the critical current oscillations with applied flux. This simplified analysis to the point that the half-period phase shift could be observed directly in the raw data. A different combination of Ni and NiFe thicknesses were used. While not at exactly the point where the critical current was the same in the P and AP states, this additional set of thicknesses combined with other studies from our group and our collaborators at NGC allowed for a tentative phase diagram to be mapped out showing for what Ni and NiFe thicknesses the P and AP magnetic states corresponded to 0 and π phase states.

Ni has caused persistent issues in spin-valve style Josephson junctions because it has a magnetic structure that is not single-domain on the size scale of the junction. This is suspected to cause stray fields from the domain walls which pin the NiFe free layer and

prevent it from switching cleanly and consistently. As a possible solution, Fe was studied as an alternative fixed layer. The effect of the seed layer was studied and Fe was shown to have a reduced dead layer and cleaner switching when grown on Cu than when grown directly on Nb. Unfortunately, the junctions made from Fe showed much lower critical currents than Ni, and the $0 - \pi$ transition could not be seen clearly. Fe was not pursued further as the degraded superconductivity was too serious an issue to offset any improvement in magnetics. Fe may still show promise for other Josephson junctions such as spin triplet experiments with a Cr interface [100], but not for the simple case of a singlet π junction.

Investigating CoGd as a magnetic material in Josephson junctions showed exciting results in terms of the underlying physics, although many of the same challenges for application remained. The alloy was grown close to its compensation point where the net magnetizaiton is zero, but a Josephson junction thickness series showed a $0 - \pi$ transition similar to that seen in a strong ferromagnet. The spin-polarized transport currents through this and similar alloys may offer a new avenue for taking advantage of the phase shifts present in magnetic Josephson junctions without the disadvantage of stray magnetic fields produced by including ferromagnetic materials in superconducting circuits.

7.1 Future Work

While extensively studied as a magnetic material, CoGd and the broader category of Rare-Earth Transition-Metal ferrimagnets as a Josephson junction barrier is new and has lots of room for further explanation. Investigating how to control the compensation point in ultra-thin films (below 10 nm) is important; here it was shown that the compensation temperature varies significantly with even angstrom-scale changes in thickness. Improvements

in deposition techniques would also be invaluable. Triode sputtering from an alloy target showed differences in the target and film compositions that varied with sputtering power, making it difficult to grow films exactly at their compensation point. Further characterizing this sputtering process or making Josephson junctions using a cosputtering process could allow observation of the $0-\pi$ transition where the films are better compensated rather than in a wide "low-moment" regime.

Further magnetic film measurements could further clarify the behavior of the CoGd alloy. The moment vs temperature curves studied here began to turn downwards near room temperature. As CoGd is often modeled as two sublattices with a shared Curie temperature, extending these measurements to high enough temperature to observe T_C directly might give insight into the contributions of the two sublattices at different thicknesses. Direct comparison to films of the constituent elements would also help this effort; currently our group is measuring the Curie temperature of Co films over the same thickness range.

In all of the projects here, a major limiting factor was the maximum critical current of the Josephson junction. For integration in the JMRAM memory cell, the entire stack must support a critical current of at least 100 µA. While large critical currents were possible using Ni as a free layer, its magnetic domain structure on the scale of the junction caused poor reproducibility and inconsistent switching of the free layer. Attempting to replace Ni with Fe significantly reduced the critical current, immediately ruling it out as a fixed layer candidate in this architecture. CoGd, while intriguing for the possibility of a low-moment π junction, also showed very low critical current. Finding either new materials or techniques such as interface engineering [82] to allow higher supercurrent through a magnetic Josephson junction remains a high priority.

There are several possibilities to explore through improving the critical current of CoGd

Josephson junctions. The material used here was an amorphous film sputtered from an alloy target at $-30\,^{\circ}\mathrm{C}$. The magnetic and structural properties of CoGd are very sensitive to growth conditions and processing [101] so further exploring growth conditions or introducing an annealing process may help to decrease the scattering due to the amorphous structure. Alternatively, a heterostructure Co and Gd layers could be explored instead of an alloy. Alternating Co and Gd layers grown on Si can maintain a polycrystaline microstructure [102], and the longer mean free path of this structure could allow for larger supercurrent than in the amorphous alloy.

REFERENCES

REFERENCES

[1] Eric Masanet, Arman Shehabi, Nuoa Lei, Sarah Smith, and Jonathan Koomey. Recalibrating global data center energy-use estimates. *Science*, 367(6481):984–986, 2020.

[2] D. A. Buck. The cryotron-a superconductive computer component. *Proceedings of the IRE*, 44(4):482–493, 1956.

[3] B.D. Josephson. Possible new effects in superconductive tunnelling. *Physics Letters*, 1(7):251–253, 1962.

[4] W. Anacker. Josephson computer technology: An IBM research project. *IBM Journal of Research and Development*, 24(2):107–112, 1980.

[5] Cyrus C. M. Mody. Between research and development: IBM and Josephson computing. *Physics Today*, 69(10):32–38, 2016.

[6] J. Matisoo. Subnanosecond pair-tunneling to single-particle tunneling transitions in josephson junctions. *Applied Physics Letters*, 9(4):167–168, 1966.

[7] Hans-D. Hahlbohm and Heinz Lübbig, editors. *SQUID '85 Superconducting Quantum Interference Devices and their Applications: Proceedings of the Third International Conference on Superconducting Quantum Devices, Berlin (West), June 25-28, 1985.* De Gruyter, 2012.

[8] K.K. Likharev and V.K. Semenov. Rsfq logic/memory family: a new Josephson-junction technology for sub-terahertz-clock-frequency digital systems. *IEEE Transactions on Applied Superconductivity*, 1(1):3–28, 1991.

[9] Oleg A. Mukhanov. Energy-efficient single flux quantum technology. *IEEE Transactions on Applied Superconductivity*, 21(3):760–769, 2011.

[10] Masamitsu Tanaka, Atsushi Kitayama, Tomohito Koketsu, Masato Ito, and Akira Fujimaki. Low-energy consumption rsfq circuits driven by low voltages. *IEEE Transactions on Applied Superconductivity*, 23(3):1701104–1701104, 2013.

[11] Yuki Yamanashi, Takanobu Nishigai, and Nobuyuki Yoshikawa. Study of lr-loading technique for low-power single flux quantum circuits. *IEEE Transactions on Applied Superconductivity*, 17(2):150–153, 2007.

[12] Quentin P. Herr, Anna Y. Herr, Oliver T. Oberg, and Alexander G. Ioannidis. Ultra-low-power superconductor logic. *Journal of Applied Physics*, 109(10):103903, 2011.

[13] Superconducting technology assessment. Technical report, National Security Agency Office of Corporate Assessments, 2005.

[14] Sergey K. Tolpygo. Superconductor digital electronics: Scalability and energy efficiency issues (review article). *Low Temperature Physics*, 42(5):361–379, 2016.

[15] Shamiul Alam, Md Shafayat Hossain, Srivatsa Rangachar Srinivasa, and Ahmedullah Aziz. Cryogenic Memory Technologies. *arXiv e-prints*, page arXiv:2111.09436, November 2021.

[16] N. Yoshikawa, T. Tomida, M. Tokuda, Q. Liu, X. Meng, S.R. Whiteley, and T. VanDuzer. Characterization of 4 K CMOS Devices and Circuits for Hybrid Josephson-CMOS Systems. *IEEE Transactions on Appiled Superconductivity*, 15(2):267–271, June 2005.

[17] Shuichi Tahara, Ichiro Ishida, Yumi Ajisawa, and Yoshifusa Wada. Experimental vortex transitional nondestructive read-out Josephson memory cell. *Journal of Applied Physics*, 65(2):851–856, January 1989.

[18] S. Nagasawa, Y. Hashimoto, H. Numata, and S. Tahara. A 380 ps, 9.5 mW Josephson 4-Kbit RAM operated at a high bit yield. *IEEE Transactions on Applied Superconductivity*, 5(2):2447–2452, 1995.

[19] Ian M. Dayton, Tessandra Sage, Eric C. Gingrich, Melissa G. Loving, Thomas F. Ambrose, Nathan P. Siwak, Shawn Keebaugh, Christopher Kirby, Donald L. Miller, Anna Y. Herr, Quentin P. Herr, and Ofer Naaman. Experimental demonstration of a Josephson magnetic memory cell with a programmable π-junction. *IEEE Magnetics Letters*, 9:1–5, 2018.

[20] V. V. Ryazanov, V. A. Oboznov, A. Yu. Rusanov, A. V. Veretennikov, A. A. Golubov, and J. Aarts. Coupling of two superconductors through a ferromagnet: Evidence for a π junction. *Phys. Rev. Lett.*, 86:2427–2430, Mar 2001.

[21] S. M. Frolov, D. J. Van Harlingen, V. A. Oboznov, V. V. Bolginov, and V. V. Ryazanov. Measurement of the current-phase relation of superconductor/ferromagnet/superconductor π Josephson junctions. *Phys. Rev. B*, 70:144505, Oct 2004.

[22] A. F. Volkov. New phenomena in Josephson SINIS junctions. *Phys. Rev. Lett.*, 74:4730–4733, Jun 1995.

[23] J. J. A. Baselmans, A. F. Morpurgo, B. J. van Wees, and T. M. Klapwijk. Reversing the direction of the supercurrent in a controllable Josephson junction. *Nature*, 397:43, Jan 1999.

[24] J. J. A. Baselmans, B. J. van Wees, and T. M. Klapwijk. Nonequilibrium supercurrent transport in controllable superconductor–normal-metal–superconductor junctions. *Phys. Rev. B*, 63:094504, Jan 2001.

[25] Jian Huang, F. Pierre, Tero T. Heikkilä, Frank K. Wilhelm, and Norman O. Birge. Observation of a controllable π junction in a 3-terminal Josephson device. *Phys. Rev. B*, 66:020507, Jul 2002.

[26] Frank K. Wilhelm, Gerd Schön, and Andrei D. Zaikin. Mesoscopic superconducting–normal metal–superconducting transistor. *Phys. Rev. Lett.*, 81:1682–1685, Aug 1998.

[27] S.-K. Yip. Energy-resolved supercurrent between two superconductors. *Phys. Rev. B*, 58:5803–5807, Sep 1998.

[28] S.-K. Yip. Magnetic-field effect on the supercurrent of an SNS junction. *Phys. Rev. B*, 62:R6127–R6130, Sep 2000.

[29] T. T. Heikkilä, F. K. Wilhelm, and G. Schön. Non-equilibrium supercurrent through mesoscopic ferromagnetic weak links. *EPL (Europhysics Letters)*, 51(4):434, 2000.

[30] T. Yamashita, S. Takahashi, and S. Maekawa. Controllable π junction with magnetic nanostructures. *Phys. Rev. B*, 73:144517, Apr 2006.

[31] J-P Cleuziou, Wolfgang Wernsdorfer, V Bouchiat, Th Ondarçuhu, and M Monthioux. Carbon nanotube superconducting quantum interference device. *Nat. Nanotech.*, 1(1):53–59, 2006.

[32] R. Delagrange, R. Weil, A. Kasumov, M. Ferrier, H. Bouchiat, and R. Deblock. 0-π quantum transition in a carbon nanotube Josephson junction: Universal phase dependence and orbital degeneracy. *Physica B: Condensed Matter*, 536:211 – 222, 2018.

[33] Jorden A Van Dam, Yuli V Nazarov, Erik PAM Bakkers, Silvano De Franceschi, and Leo P Kouwenhoven. Supercurrent reversal in quantum dots. *Nature*, 442(7103):667, 2006.

[34] D. B. Szombati, S. Nadj-Perge, D. Car, S. R. Plissard, E. P. A. M. Bakkers, and L. P. Kouwenhoven. Josephson ϕ_0-junction in nanowire quantum dots. *Nature Physics*, 12:568 – 572, May 2016.

[35] Joseph A. Glick, Victor Aguilar, Adel B. Gougam, Bethany M. Niedzielski, Eric C. Gingrich, Reza Loloee, William P. Pratt, and Norman O. Birge. Phase control in a spin-triplet SQUID. *Science Advances*, 4(7):eeat9457, 2018.

[36] Boris Kastening, Dirk K. Morr, Dirk Manske, and Karl Bennemann. Novel Josephson effect in triplet-superconductor–ferromagnet–triplet-superconductor junctions. *Phys. Rev. Lett.*, 96:047009, Feb 2006.

[37] Benjamin, C., Jonckheere, T., Zazunov, A., and Martin, T. Controllable π junction in a Josephson quantum-dot device with molecular spin. *Eur. Phys. J. B*, 57(3):279–289, 2007.

[38] Babak Zare Rameshti, Ali G. Moghaddam, and Malek Zareyan. Gate-controlled supercurrent reversal in MoS_2-based Josephson junctions. *EPL (Europhysics Letters)*, 108(3):37002, 2014.

[39] S. Mironov, E. Goldobin, D. Koelle, R. Kleiner, Ph. Tamarat, B. Lounis, and A. Buzdin. Anomalous Josephson effect controlled by an Abrikosov vortex. *Phys. Rev. B*, 96:214515, Dec 2017.

[40] Falko Pientka, Anna Keselman, Erez Berg, Amir Yacoby, Ady Stern, and Bertrand I. Halperin. Topological superconductivity in a planar Josephson junction. *Phys. Rev. X*, 7:021032, May 2017.

[41] Taro Yamashita. Phase shift and control in superconducting hybrid structures. *IEICE Transactions on Electronics*, E101.C(5):378–384, 2018.

[42] A. V. Ustinov and V. K. Kaplunenko. Rapid single-flux quantum logic using π-shifters. *J. App. Phys.*, 94(8):5405–5407, 2003.

[43] T. Ortlepp, Ariando, O. Mielke, C. J. M. Verwijs, K. F. K. Foo, H. Rogalla, F. H. Uhlmann, and H. Hilgenkamp. Flip-flopping fractional flux quanta. *Science*, 312(5779):1495–1497, 2006.

[44] M I Khabipov, D V Balashov, F Maibaum, A B Zorin, V A Oboznov, V V Bolginov, A N Rossolenko, and V V Ryazanov. A single flux quantum circuit with a ferromagnet-based Josephson π-junction. *Superconductor Science and Technology*, 23(4):045032, 2010.

[45] Tomohiro Kamiya, Masamitsu Tanaka, Kyosuke Sano, and Akira Fujimaki. Energy/space-efficient rapid single-flux-quantum circuits by using π-shifted Josephson junctions. *IEICE Transactions on Electronics*, E101.C(5):385–390, 2018.

[46] L. B. Ioffe, V. B. Geshkenbein, M. V. Feigel'man, A. L. Fauchere, and G. Blatter. Environmentally decoupled sds-wave Josephson junctions for quantum computing. *Nature*, 398:679–681, 1999.

[47] G. Blatter, V. B. Geshkenbein, and L. B. Ioffe. Design aspects of superconducting-phase quantum bits. *Phys. Rev. B*, 63:174511, 2001.

[48] T. Yamashita, K. Tanikawa, S. Takahashi, and S. Maekawa. Superconducting π qubit with a ferromagnetic Josephson junction. *Phys. Rev. Lett.*, 95:097001, 2005.

[49] A. K. Feofanov, V. A. Oboznov, V. V. Bol'ginov, J. Lisenfeld, S. Poletto, V. V. Ryazanov, A. N. Rossolenko, M. Khabipov, D. Balashov, A. B. Zorin, P. N. Dmitriev, V. P. Koshelets, and A. V. Ustinov. Implementation of superconductor/ferromagnet/ superconductor π-shifters in superconducting digital and quantum circuits. *Nat. Phys.*, 6(8):593–597, Aug 2010.

[50] N. K. Katam, O. A. Mukhanov, and M. Pedram. Superconducting magnetic field programmable gate array. *IEEE Trans. Appl. Supercond.*, 28(2):1–12, March 2018.

[51] F. London and H London. The electromagnetic equations of the supraconductor. *Proceedings of the Royal Society of London. Series A - Mathematical and Physical Sciences*, 149(866):71–88, March 1935.

[52] Lev Davidovich Landau and V L Ginzburg. On the theory of superconductivity. *Zh. Eksp. Teor. Fiz.*, 20:1064, 1950.

[53] L. D. Landau and E. M. Lifshitz. *Statistical Physics*, chapter XIV. Pergamon Press Ltd., 2nd edition, 1958[1969].

[54] Michael Tinkham. *Introduction to Superconductivity*. Dover Publications, 2nd edition, 1996.

[55] J. Bardeen, L. N. Cooper, and J. R. Schrieffer. Microscopic theory of superconductivity. *Phys. Rev.*, 106:162–164, Apr 1957.

[56] J. Bardeen, L. N. Cooper, and J. R. Schrieffer. Theory of superconductivity. *Phys. Rev.*, 108:1175–1204, Dec 1957.

[57] L.P. Gor'kov. Microscopic derivation of the ginzbug-landau equations in the theory of superconductivity. *Soviet Phys. JETP*, 36:1364, 1959.

[58] M. G. Blamire. The Potential of the Josephson Energy. *Journal of Superconductivity and Novel Magnetism*, 34(6):1629–1632, June 2020.

[59] Antonio Barone and Gianfranco Paterno. *Josephson Junctions in Superconducting Loops*, chapter 6.2, pages 122–128. John Wiley & Sons, Ltd, 1982.

[60] J. Matisoo. Critical currents and current distributions in josephson junctions. *Journal of Applied Physics*, 40(4):1813–1820, 1969.

[61] M G Blamire, C B Smiet, N Banerjee, and J W A Robinson. Field modulation of the critical current in magnetic Josephson junctions. *Superconductor Science and Technology*, 26(5):055017, May 2013.

[62] E. A. Demler, G. B. Arnold, and M. R. Beasley. Superconducting proximity effects in magnetic metals. *Phys. Rev. B*, 55:15174–15182, Jun 1997.

[63] A. F. Volkov, F. S. Bergeret, and K. B. Efetov. Odd triplet superconductivity in superconductor-ferromagnet multilayered structures. *Phys. Rev. Lett.*, 90:117006, Mar 2003.

[64] A. I. Buzdin. Proximity effects in superconductor-ferromagnet heterostructures. *Rev. Mod. Phys.*, 77:935–976, Sep 2005.

[65] LN Bulaevskii, VV Kuzii, and AA Sobyanin. Superconducting system with weak coupling to the current in the ground state. *JETP lett*, 25(7):290–294, 1977.

[66] T. Kontos, M. Aprili, J. Lesueur, F. Genêt, B. Stephanidis, and R. Boursier. Josephson Junction through a Thin Ferromagnetic Layer: Negative Coupling. *Phys. Rev. Lett.*, 89:137007, Sep 2002.

[67] Antonio Barone and Gianfranco Paterno. *Josephson Junctions in Superconducting Loops*, chapter 12, pages 354–382. John Wiley & Sons, Ltd, 1982.

[68] Bethany Maria Niedzielski. *Phase sensitive measurements of ferromagnetic Josephson junctions for cryogenic memory applications*. PhD thesis, Michigan State University, 2017. OCLC: 1028049502.

[69] III Glick, Joseph Allen. *Ferromagnetic Josephson Junctions Carrying Spin-Triplet Supercurrent for Cryogenic Memory*. PhD thesis, Michigan State University, 2017.

[70] Alexander E Madden, Joshua C Willard, Reza Loloee, and Norman O Birge. Phase controllable Josephson junctions for cryogenic memory. *Superconductor Science and Technology*, 32(1):015001, January 2019.

[71] E. C. Gingrich, Bethany M. Niedzielski, Joseph A. Glick, Yixing Wang, D. L. Miller, Reza Loloee, W. P. Pratt Jr, and Norman O. Birge. Controllable 0-π Josephson junctions containing a ferromagnetic spin valve. *Nat. Phys.*, 12(6):564–567, Jun 2016.

[72] Boris Chesca, Reinhold Kleiner, and Dieter Koelle. SQUID Theory. In J. Clarke and A. I. Braginski, editors, *The SQUID Handbook*, chapter 2, pages 29–92. Wiley-Blackwell, 2005.

[73] Won-Tien Tsang and T. Van Duzer. Influence of the current-phase relation on the critical-current-applied-magnetic-flux dependence in parallel-connected josephson junctions. *Journal of Applied Physics*, 47(6):2656–2661, 1976.

[74] P. Quarterman, Nathan Satchell, B. J. Kirby, Reza Loloee, Gavin Burnell, Norman O. Birge, and J. A. Borchers. Distortions to the penetration depth and coherence length of superconductor/normal-metal superlattices. *Phys. Rev. Materials*, 4:074801, Jul 2020.

[75] Bethany M. Niedzielski, T. J. Bertus, Joseph A. Glick, R. Loloee, W. P. Pratt, and Norman O. Birge. Spin-valve josephson junctions for cryogenic memory. *Phys. Rev. B*, 97:024517, Jan 2018.

[76] B. Baek, M.L. Schneider, M.R. Pufall, and W.H. Rippard. Phase Offsets in the Critical-Current Oscillations of Josephson Junctions Based on Ni and Ni- (Ni 81 Fe 19) x Nb y Barriers. *Physical Review Applied*, 7(6):064013, June 2017.

[77] Joseph A. Glick, Mazin A. Khasawneh, Bethany M. Niedzielski, Reza Loloee, W. P. Pratt, Norman O. Birge, E. C. Gingrich, P. G. Kotula, and N. Missert. Critical current oscillations of elliptical Josephson junctions with single-domain ferromagnetic layers. *Journal of Applied Physics*, 122(13):133906, October 2017.

[78] M. Fauré, A. I. Buzdin, A. A. Golubov, and M. Yu. Kupriyanov. Properties of superconductor/ferromagnet structures with spin-dependent scattering. *Phys. Rev. B*, 73:064505, Feb 2006.

[79] D M Heim, N G Pugach, M Yu Kupriyanov, E Goldobin, D Koelle, R Kleiner, N Ruppelt, M Weides, and H Kohlstedt. The effect of normal and insulating layers on $0-\pi$ transitions in Josephson junctions with a ferromagnetic barrier. *New Journal of Physics*, 17(11):113022, November 2015.

[80] B. Crouzy, S. Tollis, and D. A. Ivanov. Josephson current in a superconductor-ferromagnet junction with two noncollinear magnetic domains. *Phys. Rev. B*, 75:054503, Feb 2007.

[81] Norman Birge, Alexander E. Madden, and Ofer Naaman. Ferromagnetic Josephson junctions for cryogenic memory. In Henri Jaffrès, Henri-Jean Drouhin, Jean-Eric Wegrowe, and Manijeh Razeghi, editors, *Spintronics XI*, page 57, San Diego, United States, September 2018. SPIE.

[82] Swapna Sindhu Mishra, Robert M. Klaes, Joshua Willard, Reza Loloee, and Norman O. Birge. Enhancement of supercurrent through ferromagnetic materials by interface engineering. *Phys. Rev. B*, 106:014519, Jul 2022.

[83] Melissa G. Loving, Thomas F. Ambrose, Henry Ermer, Don Miller, and Ofer Naaman. Interplay between interface structure and magnetism in NiFe/Cu/Ni-based pseudo-spin valves. *AIP Advances*, 8(5):056309, May 2018.

[84] Rakesh K. Singh, Nicholas D. Rizzo, Michelle Bertram, Kaiwen Zheng, and Nathan Newman. Improvement in the Magnetic Properties of Ni–Fe Thin Films on Thick Nb

Electrodes Using Oxidation and Low-Energy Ar Ion Milling. *IEEE Magnetics Letters*, 9:1–4, 2018.

[85] S. Piano, J. W. A. Robinson, G. Burnell, and M. G. Blamire. 0-π oscillations in nanostructured nb/fe/nb Josephson junctions. *The European Physical Journal B*, 58(2):123–126, Jul 2007.

[86] J. W. A. Robinson, S. Piano, G. Burnell, C. Bell, and M. G. Blamire. Zero to π transition in superconductor-ferromagnet-superconductor junctions. *Phys. Rev. B*, 76:094522, Sep 2007.

[87] Joseph Finley and Luqiao Liu. Spintronics with compensated ferrimagnets. *Applied Physics Letters*, 116(11):110501, 2020.

[88] Se Kwon Kim, Geoffrey S. D. Beach, Kyung-Jin Lee, Teruo Ono, Theo Rasing, and Hyunsoo Yang. Ferrimagnetic spintronics. *Nature Materials*, 21(1):24–34, January 2022.

[89] P. Chaudhari, J. J. Cuomo, and R. J. Gambino. Amorphous metallic films for bubble domain applications. *IBM Journal of Research and Development*, 17(1):66–68, 1973.

[90] Thomas A. Ostler, Richard F. L. Evans, Roy W. Chantrell, Unai Atxitia, Oksana Chubykalo-Fesenko, Ilie Radu, Radu Abrudan, Florin Radu, Arata Tsukamoto, A. Itoh, Andrei Kirilyuk, Theo Rasing, and Alexey Kimel. Crystallographically amorphous ferrimagnetic alloys: Comparing a localized atomistic spin model with experiments. *Physical Review B*, 84(2):024407, July 2011.

[91] K H J Buschow. Intermetallic compounds of rare-earth and 3d transition metals. *Reports on Progress in Physics*, 40(10):1179–1256, oct 1977.

[92] P. Hansen, C. Clausen, G. Much, M. Rosenkranz, and K. Witter. Magnetic and magneto-optical properties of rare-earth transition-metal alloys containing Gd, Tb, Fe, Co. *Journal of Applied Physics*, 66(2):756–767, July 1989.

[93] Lakhan Bainsla, Akash Kumar, Ahmad A. Awad, Chunlei Wang, Mohammad Zahedinejad, Nilamani Behera, Himanshu Fulara, Roman Khymyn, Afshin Houshang, Jonas Weissenrieder, and Johan Åkerman. Ultrathin Ferrimagnetic GdFeCo Films with Low Damping. *Advanced Functional Materials*, 32(23):2111693, June 2022.

[94] C. D. Stanciu, A. V. Kimel, F. Hansteen, A. Tsukamoto, A. Itoh, A. Kirilyuk, and Th. Rasing. Ultrafast spin dynamics across compensation points in ferrimagnetic GdFeCo: The role of angular momentum compensation. *Phys. Rev. B*, 73:220402, Jun 2006.

[95] T. Kato, K. Nakazawa, R. Komiya, N. Nishizawa, S. Tsunashima, and S. Iwata. Compositional dependence of g-factor and damping constant of gdfeco amorphous alloy films. *IEEE Transactions on Magnetics*, 44(11):3380–3383, 2008.

[96] A. D. Naylor, G. Burnell, and B. J. Hickey. Transport spin polarization of the rare-earth transition-metal alloy $co_{1-x}gd_x$. *Phys. Rev. B*, 85:064410, Feb 2012.

[97] Christian Kaiser, Alex F. Panchula, and Stuart S. P. Parkin. Finite Tunneling Spin Polarization at the Compensation Point of Rare-Earth-Metal–Transition-Metal Alloys. *Physical Review Letters*, 95(4):047202, July 2005.

[98] A. Brunsch and J. Schneider. H2and n2contaminated amorphous cogd and fegd films. *IEEE Transactions on Magnetics*, 14(5):731–733, 1978.

[99] Yu. M. Ivanchenko and L. A. Zil'Berman. The Josephson Effect in Small Tunnel Contacts. *Soviet Journal of Experimental and Theoretical Physics*, 28:1272, June 1969.

[100] Sachio Komori, James M. Devine-Stoneman, Kohei Ohnishi, Guang Yang, Zhanna Devizorova, Sergey Mironov, Xavier Montiel, Linde A. B. Olde Olthof, Lesley F. Cohen, Hidekazu Kurebayashi, Mark G. Blamire, Alexandre I. Buzdin, and Jason W. A. Robinson. Spin-orbit coupling suppression and singlet-state blocking of spin-triplet cooper pairs. *Science Advances*, 7(3):eabe0128, 2021.

[101] Kohei Ueda, Aik Jun Tan, and Geoffrey S. D. Beach. Effect of annealing on magnetic properties in ferrimagnetic gdco alloy films with bulk perpendicular magnetic anisotropy. *AIP Advances*, 8(12):125204, 2018.

[102] J B Pelka, W Paszkowicz, P Dłużewski, E Dynowska, A Wawro, L T Baczewski, M Kozlowski, A Wisniewski, O Seeck, S Messoloras, and H Gamari-Seale. Structural and magnetic study of co/gd multilayers deposited on si and si-n substrates. *Journal of Physics D: Applied Physics*, 34(10A):A208–A213, may 2001.